

Field Driven Design of Graded Cellular Structures

by

Mandar Hanamant Shinde

A Dissertation Presented in Partial Fulfillment  
of the Requirements for the Degree  
Doctor of Philosophy

Approved March 2023 by the  
Graduate Supervisory Committee:

Dhruv Bhate, Chair  
Yang Jiao  
Beomjin Kwon  
Yongming Liu  
Pedro Peralta

ARIZONA STATE UNIVERSITY

May 2023

## ABSTRACT

The design of energy absorbing structures is driven by application specific requirements like the amount of energy to be absorbed, maximum transmitted stress that is permissible, stroke length, and available enclosing space. Cellular structures like foams are commonly leveraged in nature for energy absorption and have also found use in engineering applications. With the possibility of manufacturing complex cellular shapes using additive manufacturing technologies, there is an opportunity to explore new topologies that improve energy absorption performance. This thesis aims to systematically understand the relationships between four key elements: (i) unit cell topology, (ii) material composition, (iii) relative density, and (iv) fields; and energy absorption behavior, and then leverage this understanding to develop, implement and validate a methodology to design the ideal cellular structure energy absorber. After a review of the literature in the domain of additively manufactured cellular materials for energy absorption, results from quasi-static compression of six cellular structures (hexagonal honeycomb, auxetic and Voronoi lattice, and diamond, Gyroid, and Schwarz-P) manufactured out of AlSi10Mg and Nylon-12. These cellular structures were compared to each other in the context of four design-relevant metrics to understand the influence of cell design on the deformation and failure behavior. Three new and revised metrics for energy absorption were proposed to enable more meaningful comparisons and subsequent design selection. Triply Periodic Minimal Surface (TPMS) structures were found to have the most promising overall performance and formed the basis for the numerical investigation of the effect of fields on the energy

absorption performance of TPMS structures. A continuum shell-based methodology was developed to analyze the large deformation behavior of field-driven variable thickness TPMS structures and validated against experimental data. A range of analytical and stochastic fields were then evaluated that modified the TPMS structure, some of which were found to be effective in enhancing energy absorption behavior in the structures while retaining the same relative density. Combining findings from studies on the role of cell geometry, composition, relative density and fields, this thesis concludes with the development of a design framework that can enable the formulation of cellular material energy absorbers with idealized behavior.

## DEDICATION

This thesis is dedicated to my parents and my wife, who motivated me throughout this journey.



## ACKNOWLEDGMENTS

Words cannot express my gratitude to my advisor and chair of my committee, Dhruv Bhate, for his invaluable patience and feedback. I also could not have undertaken this journey without my defense committee, who generously provided knowledge and expertise. Additionally, this endeavor would not have been possible without the generous support from BAE Systems, America Makes and the Fulton Schools of Engineering at ASU, who collectively financed my research. I would also like to extend my thanks to members of our 3DXResearch group, in particular to Cameron Noe for supporting all the 3D printing builds in this study, Paul Paradise for generating test data of IN718 for thickness dependent model, and Irving Edwin Ramirez-Chavez for teaching me DIC and helping conduct compression tests of the cellular structures in this work. Athul for helping with Nylon-12 material model development. Tyler, and Yash for valuable inputs during group meetings.

## TABLE OF CONTENTS

	Page
LIST OF TABLES .....	ix
LIST OF FIGURES.....	x
CHAPTER	
1. INTRODUCTION.....	1
1.1. Literature Review.....	2
1.1.1 Energy Absorption Parameters .....	4
1.1.2 Ideal Energy Absorption Behavior .....	8
1.1.3 Empirical Studies .....	9
1.1.4 Modeling For AM Cellular Structure Deformation .....	12
1.2. Research Gaps.....	14
1.3. Thesis Objectives .....	15
1.4. Thesis Approach And Scope.....	16
2. COMPRESSION BEHAVIOR OF CELLULAR MATERIALS.....	19
2.1. Design And Manufacturing.....	20
2.2. Manufacturing.....	23
2.3. Test Setup.....	26
2.4. Results.....	27
2.4.1 Hexagonal Honeycomb.....	27
2.4.2 Auxetic Lattice.....	29
2.4.3 Voronoi (Stochastic) Lattice .....	31

CHAPTER	Page
2.4.4 Schwarz-P TPMS .....	33
2.4.5 Diamond TPMS .....	35
2.4.6 Gyroid TPMS.....	37
2.5. Analysis.....	38
2.5.1 Specific Energy Absorption and Transmitted Stress .....	38
2.5.2 Densification Efficiency .....	40
2.5.3 Plateau Undulation.....	42
2.5.4 Tunability .....	43
2.5.5 Evaluating Overall Energy Absorption Performance .....	45
3. ENERGY ABSORPTION METRICS.....	47
3.1. The Role of Densification Strain in Energy Absorption.....	48
3.2. Approaches for Estimating the Onset Strain of Densification (OSD).....	51
3.2.1 Graphical Method .....	53
3.2.2 Fixed Strain Method .....	54
3.2.3 Plateau Stress Based Method.....	55
3.2.4 Maximum Efficiency Method.....	55
3.3. Objectives and Structure of this Paper.....	56
3.4. The Hybrid Efficiency Method for Estimating the OSD .....	57
3.5. Methods.....	59
3.5.1 Design .....	59
3.5.2 Manufacturing.....	60

CHAPTER	Page
3.6. Matlab Implementation .....	62
3.7. Results.....	63
3.7.1 Compression Response .....	63
3.8. Onset strain of Densification ( $\epsilon_d$ ).....	65
3.9. Discussion.....	68
3.9.1 Specific Energy Absorption (SEA).....	68
3.9.2 Maximum Transmitted Stress (MTS) .....	70
3.10. Conclusions.....	70
4. FINITE ELEMENT ANALYSIS OF SHELL STRUCTURES.....	72
4.1. Modeling CAD structures for FEA.....	75
4.2. Material Model.....	78
4.3. Mesh Convergence:.....	80
4.4. Finite Element Model.....	82
4.5. Results.....	84
4.6. Drawbacks of the conventional shell model: .....	87
4.7. Continuum Shell Elements.....	88
4.7.1 Patch Tests .....	90
4.8. Continuum shell model for Schwarz-Primitive .....	91
4.9. Results.....	92
4.10. Variable Thickness FEA Modeling .....	92
4.11. Conclusions.....	94

CHAPTER	Page
5. FIELD-DRIVEN DESIGN.....	96
5.1. Field-Driven Design of Cellular Materials .....	97
5.2. Simulation Driven design.....	99
5.2.1 Field Selection.....	102
5.2.2 Thickness Distribution .....	104
5.2.3 Manufacturing and Charactorization .....	107
5.2.4 Compression Testing .....	109
5.2.5 FEA Validation .....	112
5.3. Analytical Field Driven Design.....	114
5.3.1 Uniform Gradient Field.....	114
5.3.2 Shear Band Field.....	118
5.3.3 Radial Field .....	121
5.4. Stochastic Fields.....	124
5.4.1 Simplex Noise Field.....	124
5.4.2 Cellular Noise Field .....	126
5.5. Conculsions.....	129
6. SUMMARY AND FUTURE STUDY .....	130
6.1. Summary .....	130
6.2. Future Work.....	132
REFERENCES.....	134

APPENDIX	Page
A. MATLAB CODE INFORMATION.....	144
B. ONSET STRAIN OF DENSIFICATION.....	153
C. ABAQUS SCRIPT.....	173
D. ENERGY ABSORPTION VARIABILITY GRAPHS.....	176
E. DECLARATION.....	180

## LIST OF TABLES

Table	Page
1 Compilation of Quasi-Static Energy Absorption Studies in Lattice Structures Manufactured with Metal Additive Manufacturing.....	11
2. Unit Cell Shapes and Relative Densities Designed for the Study.....	21
3 Densification Strain Methods Used in the Literature Studying Energy Absorption Characteristics of Additively Manufactured Cellular Structures.....	51
4. Onset Strain of Densification Estimated with the Two Different Efficiency-Based Methods.....	66
5 TPMS Modeling Methods Comparison [2] .....	75
6. Element Quality Criterion For S4 Elements .....	77
7 Comparison of Energy Absorption Characteristics for 0.4 mm Schwarz-Primitive Structure.....	92
8. Thickness Range of the Schwarz-Primitive Specimens.....	106

## LIST OF FIGURES

Figure	Page
1 Helicopter Seat Drop Test Setup with Dummy; (B) Detail of Seat Energy Absorber, Installed under the Seat Pan above the Load Cell [2].....	1
2 Number of Publications in the Elsevier Database Related To Energy Absorption And Other Mechanical Properties (B) Percentage Distribution of Papers Studying Energy Absorption And Other Mechanical Properties [5] .....	3
3 Catagories of Lattice Structures Based on Cell Type And Configuration [5]. .....	4
4 (A) A Typical Compression Stress-Strain Response of A Metallic Lattice Material, Showing the First Peak, the Plateau Region, And the Onset of Densification And (B) Energy Efficiency Graphed Against Displacement, with the Peak Used To Identify the One .....	5
5. Ideal Stress-Strain Response For Maximum Energy Absorption[19] .....	8
6 Unit Cell Visual Representation of TPMS Structures (A) Gyroid Structure (B) Diamond Structure And (C) Schwarz- Primitive Structure [24]. .....	10
7 (A) Unit Cell Representation And Multilayer Model of Schwarz Primitive Lattice (B) Comparison of Stress Strain Curve Obtained with Experiment with the Unit Cell And Multilayer Simulation. [33] .....	13
8. Design of Cellular Structures Used in This Study: (A) the Six Unit Cell Shapes Used in This Study, (B) the Same Shapes Enclosed in A 0.5mm Thin Tube .....	20
9. Build Orientations of (A) Specimens with Endplates, And (B) Specimens Enclosed in Tubes.....	24



Figure	Page
10. Images of Fabricated Specimens For Each of the Six Cell Types, Showing Good Reproduction of Design Intent.....	24
11. Scanning Microscope Optical Images, And Height Maps of the Specimens Fabricated, Showing Print Quality And Resolution. ....	25
12. instron Universal Testing Machine, Camera Set Up For Compression Tests. ....	27
13 (A) Stress-Strain Curves For Honeycomb Compression with 0.4, 0.6- And 0.8-mm Thickness (*the 0.8mm Specimen Was Tested on A Different Mechanical Load Frame), (B) Honeycomb Deformation For Each of the Three Thicknesses At Increasing Strain.	28
14. Failure Analysis on Two Surfaces of the 0.8mm Wall Thickness Honeycomb (R.D. of 0.36), Showing Two Inclined Failure Bands And Lateral Fractures in the Wall Evident on Surface A; Wall Crimping Visible on Surface. ....	29
15. (A) Stress-Strain Curves For An Auxetic Lattice Shape under Compression with 0.5, 0.75 And 1mm Beam Diameters, (B) Auxetic Lattice Deformation Sequence For Each of the Three Beam Diameter Specimens At Increasing Strain.....	30
16. Failure Analysis on Two Surfaces of the Auxetic Lattice: (A) For the 0.5mm Beam Diameter Specimen (R.D. of 0.08), Surface A Shows Beams Collapsing And Closing the Re-Entrant Cell Space, Surface B Shows Shearing of Planes; (B) The 1mm Beams (R.D. of 0.27).....	31
17. (A) Stress-Strain Curves For Voronoi Lattice Shape under Compression with 0.5, 0.75, And 1mm Beam Diameters, (B) Voronoi Lattice Deformation Sequence For Each of the Three Beam Diameter Specimens At Increasing Strain.....	32

Figure	Page
18. Failure Analysis on Two Surfaces of the 0.75mm Beam Diameter Voronoi Lattice (R.D. of 0.07).....	33
19 (A) Stress-Strain Curves For Schwarz-P TPMS Structure under Compression with 0.4, 0.6, And 0.8mm Wall Thicknesses, (B) Schwarz-P TPMS Deformation Sequence For Each of the Three Wall Thickness Specimens At Increasing Strain. ....	34
20. Failure Analysis on Two Surfaces of the Schwarz-P TPMS Structure For Three Different Wall Thicknesses/Relative Densities: (A) 0.4mm/0.11 R.D.; (B) 0.6mm/0.17 R.D.; (C) 0.8mm/0.22 R.D.....	35
21 (A) Stress-Strain Curves For Diamond TPMS Structure under Compression with 0.4, 0.6 And 0.8mm Wall Thicknesses, (B) Diamond TPMS Deformation Sequence For Each of the Three Wall Thickness Specimens At Increasing Strain. ....	36
22 Failure Analysis on Two Surfaces of the Diamond TPMS Structure For 0.4mm Wall Thickness /0.13 R.D. Showing Cell Walls .....	36
23. (A) Stress-Strain Curves For Gyroid TPMS Structure under Compression with 0.4, 0.6, And 0.8mm Wall Thicknesses, (B) Gyroid TPMS Deformation Sequence For Each of the Three Wall Thickness Specimens At Increasing Strain.....	37
24. Failure Analysis on Two Surfaces of the Diamond TPMS Structure For 0.4mm Wall Thickness /0.13 R.D. Showing Cell Walls .....	38
25 (A) Comparison of SEA Vs Normalized Max Transmitted Stress (B) Zoomed in View of Lower Left Corner (C) Logarithmic Plot of Energy Absorbed Per Unit Mass Against	

Figure	Page
Maximum Transmitted Stress Till Structure Absorbs That Energy. (D) Zoomed in View of the Upper Right Corner of Plot C	39
26 Comparison of Densification Efficiencies For Each of the Six Shapes And Three Relative Densities .....	41
27. Deformation of Cellular Structures At the Densification Strain Is Mentioned Below the Picture of Individual Cellular Shapes. ....	42
28 Plateau Undulation Quantified As (A) Normalized First Dip, And (B) Normalized Plateau Range.....	43
29. (A) Normalized Effective Modulus, (B) Normalized Maximum Transmitted Stress, And (C) SEA, All Plotted As A Function of Relative Density. the Adjacent Tables Provide the Fit Parameters, with the R2 Value Indicative of the Quality of the Fit.....	44
30. (A) Stress-Strain Response Corresponding To An Auxetic Lattice Structure under Compression, (B) Progressive Collapse of the Auxetic Structure, Arrows Indicate the Collapsed Row And Correspond To the Observed Dip in.....	50
31. Onset Strain of Densification Estimated Using Various Approaches For the Schwarz Primitive Structure .....	53
32. (A) Comparison of Efficiency As Estimated Using the Instantaneous And Peak Stress Approaches; (B) Specimen At the Maximum Efficiency Estimated Using Both Approaches .....	58

Figure	Page
34. Manufactured Specimens (A) Alsi10mg Specimens Printed on Conceptlaser Mlab Machine with Laser Powder Bed Fusion (Reproduced From [42]) (B) Nylon-12 Specimens Printed on EOS Machine Using Selective Laser Sintering.....	61
35. Stress-Strain Curves of Cellular Structure under Uniaxial Compression For Nylon-12 And Alsi10Mg Structures, Normalized By the Yield Strength of the Material.....	64
36. Onset Strain of Densification Points Determined By Maximum Efficiency Method And Hybrid Efficiency Method For Studied Structures.....	67
37. Variability Graph Showing OSD Estimated with the Proposed Method For All the Cellular Structures In This Work.....	68
38. Comparison of Specific Energy Absorption Estimated By Different Methods (A) Comparison of MEM And HEM Approaches, And (B) Comparison of Fixed Strain (0.5) And HEM Approaches.....	69
39. Comparison of Maximum Transmitted Stress Estimated By Different Methods (A) Comparison of MEM And HEM Approaches, And (B) Comparison of Fixed Strain (0.5) And HEM Approaches.....	70
40 Process of Finite Element Analysis of Shell Problems [79] .....	73
41 Finite Element Models For TPMS IWP Structure (A) Solid (B)Shell (C) RVE (D) Super Element (E) Voxel [80].....	74
42 2D Mapping of A Solid into A Shell Geometry [79].....	75
43 Schwatz Primitive Unit Cell Meshed with S4 Elements. ....	76

Figure	Page
44 Front View of the Full Model of Schwarz Primitive Structure Meshed with S4 Elements. .....	77
45 Tensile Test Set Up To Evaluate Nylon-12 Stress-Strain Response. ....	79
46 Stress-Strain Curve For Nylon-12 At $10^{-3}$ Strain Rate (A) Test Data (B) Plastic Stress- Plastic Strain Conversion of the Test Data For Abaqus Material Model. ....	80
47 Mesh of S4 Elements For Schwarz Primitive Unit Cell with Element Size 0.5 mm, 0.4 mm, 0.3 mm, And 0.2 mm. ....	81
48 Mesh Convergence Graph Showing Reaction Force on the Unit Cell with Blue Curve And Time Required To Run the Complete Simulation in Seconds .....	82
49 Finite Element Analysis Model of Schwarz-Primitive Structure with Boundary Conditions.....	83
50 Energy Balance For the Schwarz-Primitive Uniaxial Compression Simulation Showing Low Artificial Energy And Low Mass Scaling Work As Compared To External Work .	85
51 Deformation Pattern And Von Mises Stress Contours in the Schwarz-Primitive Cellular Structure At (A) 0 mm, (B) 6 mm, (C) 12 mm, (D) 16.5mm, (E)21 mm, And (F) 27 mm Displacement.....	86
52 Force Displacement Response of 0.4 mm Schwarz-Primitive Cellular Structure under Uniaxial Compression Loading, Comparison with the Test Data .....	87
53 Difference in Conventional And Continuum Shell Element Modeling.....	89
54 Normals And Thickness Direction For Continuum Shell Elements Indicaing Top And Bottom Face of An Element.....	90

Figure	Page
55 Direction of Shell Normal For TPMS Schwarz Primitive Unit Cell Shown By Red Lines .....	90
56 one of the Patch Tests To Verify Equivalence of S4R And SC8R Elements.....	91
57 Continuum Shell Model of Schwarz-Primitive Structure 0.4 mm (B) Mesh For the Unit Cell.....	92
58 Force Displacement Response of 0.4 mm Schwarz-Primitive Cellular Structure under Uniaxial Compression Loading with Continuum Shell Model, Comparison with the Test Data.....	92
59 Comparison of Stress-Strain Curves Obtained From TPMS Schwarz-Primitive Model with Conventional And Continuum Shell Model. ....	92
60 Difference Between offset Functio For Uniform Thickness And Cvaribal Ethickness Continuum Shell Elements. ....	93
61. Flowchart For Abaqus Script To Generate Variable Thickness Continuum Shell Elements.....	94
61 Example of A Field-Driven Design To Drive Decisions on Cell Size And Member Thickness Locally Using An Imported Stress Field. ....	98
62 Types of Fields Used in the Study.....	99
63. Field Driven Design Methodology For Cellular Structures.....	102
64. Energy Dissipation in the Nylon-12 0.5 mm Scwarz-Primitive Structure .....	103
65 Deformed Specimen And Plastic Energy Density Field Mapping on the Undeformed Structure.....	103

Figure	Page
66 Histogram of No of Nodes And Corrospounding Plastic Energy Density. ....	104
67. Comparison of Relative Density For the Variable Thickness Structures with the Basline Uniform Thickness Structure. ....	106
68 Cut Section of Variable Thickness Schwarz-Primitive Structure, The Zoomed in Picture Shows Measurement of the Sides of A Single Cell. ....	106
69 Build Layout of the Variable Thickness Specimens. ....	107
70. Dimension Measurement of Manufactured Specimens .....	108
72 Comparison of 3D Height Map of Basline Specimen And Variable Thickness Specimen. ....	109
71 Stress-Strain Response of the Variable Thickness Schwarz-Primitive Structures And Comparison with Baseline Uniform Thickness Structure. ....	109
72 Comparison of Deformation Pattern in the Uniform Thickness Schwarz-P Structure And Variable Thickness Schwarz-Primitive Structure. ....	110
73 Densification Strain Comparison of the Variable Thickness Schwarz-Primitive Structure with the Basline Design.....	111
74 Comparison of SEA the Variable Thickness Schwarz-Primitive Structure with the Baseline Design.....	111
75 Comparison of Stress-Strain Curves Obtained By Schwarz-Primitive Testing And FE Simulation. ....	112
76 Deformation Pattern of Variable Thickness Schwarz-Primitive Structure At Strain=0.5 .....	113

Figure	Page
77 Workflow For the Analytical Field Driven Design .....	114
78 The Overlay of Uniform Gradient Field Values Varying From 0.44 mm To 0.56 mm And Schwarz-P Structure.....	115
79 Stress-Strain Curve For Uniform Gradient Variable Thickness Schwarz_P Structure And Comparison with the Uniform Thickness Structure with Same Relative Density..	116
80 Deformation Pattern of Uniform Gradient Variable Thickness Structure under Uniaxial Compression Load At Collapse of Cell Layers .....	117
81 Shear Band Formation in the AlSi10mg Gyroid, Diamond And Honeycomb Structures .....	118
82 The Overlay of Shear Band Field Values Varying From 0.43 mm To 0.56 mm And Schwarz-P Structure.....	119
83 Stress-Strain Curves And Cell Collapse Count For Shear Band Variable Thickness Schwarz-P Structure And Comparison with the Uniform Thickness Structure with Same Relative Density.....	120
84 Deformation Pattern of Shear Band Variable Thickness Structure under Uniaxial Compression Load At Collapse of Cell Layers .....	121
85 The Overlay of Radial Field Values Varying From 0.44 mm To 0.56 mm And Schwarz- P Structure.....	122
87 Deformation Pattern of Radial Field Variable Thickness Structure under Uniaxial Compression Load At Collapse of Cell Layers .....	123



Figure	Page
86. Stress Strain Curve Comparison of Spherical Field And Basline Uniform Thickness Structure.....	123
89 The Overlay of Radial Field Values Varying From 0.44 mm To 0.56 mm And Schwarz-P Structure.....	125
89. Deformation Pattern of Simplex Noise Field Variable Thickness Structure under Uniaxial Compression Load At Collapse of Cell Layers.....	126
90. Stress Strain Curve Comparison of Schwarz-P Simplex Noise Field And Basline Uniform Thickness Structure .....	126
91. The Overlay of Cellular Noise Field Values Varying From 0.43 mm To 0.56 mm And Schwarz-P Structure.....	127
90. Deformation Pattern of Cellular Noise Field Variable Thickness Structure under Uniaxial Compression Load At Collapse of Cell Layers.....	128
92. Stress Strain Curve Comparison of Schwarz-P Cellular Noise Field And Basline Uniform Thickness Structure .....	128

## CHAPTER 1: INTRODUCTION

Energy absorption refers to the ability of a material to withstand loads without catastrophic failure of the system that is being protected, while impact absorption refers to the same concept, but specifically at high strain rates [1]. In both cases, there is often a need to dissipate the energies of the applied load in ways that ensure that the stress does not exceed a threshold value determined for the system being protected. The area under the stress-strain curve represents the absorbed energy prior to the final catastrophic failure (or, in the case of compression, full densification). The energy and impact absorption of cellular materials is well known, with sandwich panels adopted for decades in aerospace, marine, and automotive industries due to their high stiffness-to-weight ratio and excellent energy absorption capability [1].

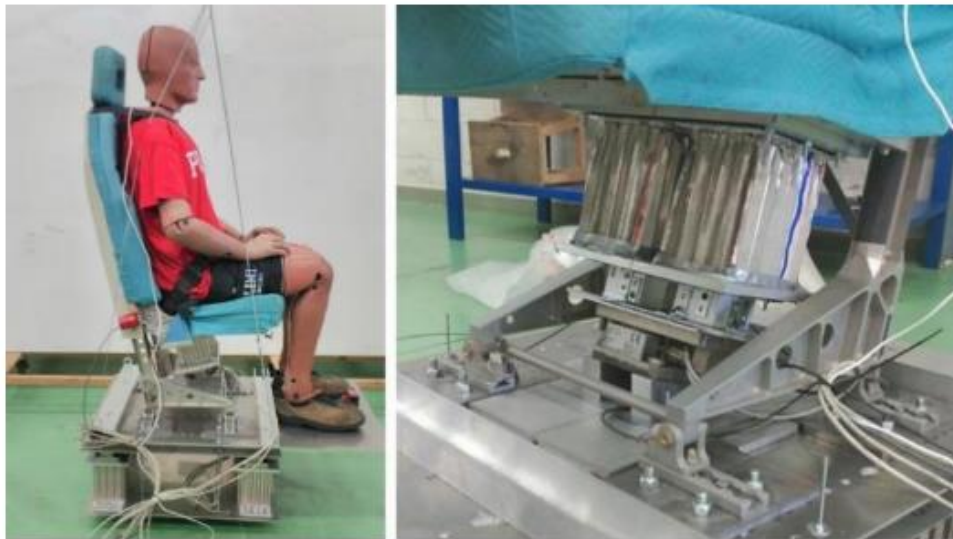


Figure 1. Helicopter seat drop test setup with dummy; (b) detail of seat energy absorber, installed under the seat pan above the load cell [2]

Polymer-based foams are suitable for impacts and cushioning for individuals in contact sports, effectively low-velocity impact. For higher velocity impact or blast protection, a metallic cellular material tends to be more suitable with energy absorbed irreversibly and accompanied by buckling, plastic deformation, and/or fracture [1]. Situations where a metal-based lattice would be more beneficial for impact protection, are in automobiles, airplanes, rotorcrafts, and spacecraft, due to the durability of metals compared to polymers, as well as the higher impact strength. Lightweight Aluminum honeycombs are mainly used in transportation and aerospace industries, often for impact protection, as shown for one example in Figure 1. For impact protection, the impact event typically imparts an impulse rather than transmitting energy, and it is typical to leverage heavy faceplates to absorb this impact with similar requirements [3]. Studies of energy-absorbing structures usually begin with quasi-static analysis and testing, the majority of which is done in compression, which is followed by studies at impact velocities more relevant to the application of interest [4].

### 1.1. Literature Review

In recent years, cellular structures have become a topic of research interest in the structural design domain, especially for their energy absorption characteristics. In the Elsevier database, there are more than 250,000 research papers by the end of 2021. 30% of those papers study the energy absorption behavior of the cellular structures [5], as shown in Figure 2.

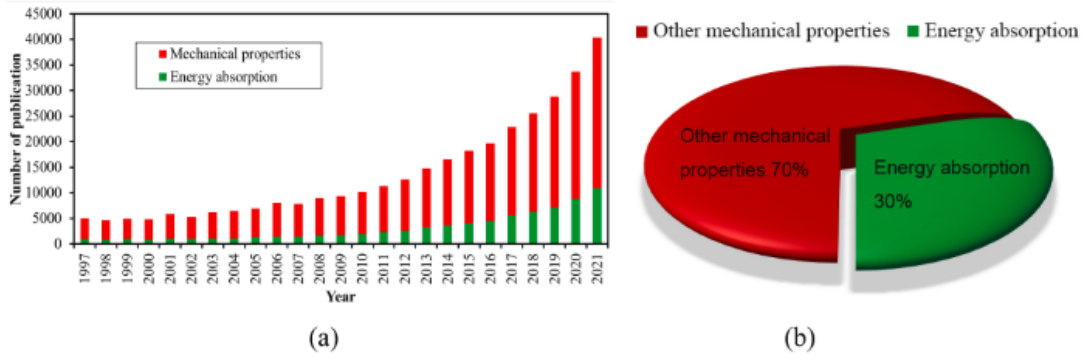


Figure 2. Number of publications in the Elsevier database related to Energy absorption and other mechanical properties (b) Percentage distribution of papers studying energy absorption and other mechanical properties [5]

Lattice structures can be further divided into 2D and 3D lattice structures as per the nature of the unit cell and the arrangement of cells in the space. Figure 3 gives insight into varieties of 2D and 3D lattice structures. 2D lattices are prismatic structures with the cellular arrangement in a plane normal to the prismatic direction. Regular honeycombs are the most widely used 2D lattice structure. In 3D lattice structures, cells are arranged in all three directions perpendicular to each other. It has identical mechanical properties in three (X, Y and Z) directions. Based on cell configuration, 3D lattice structures can be divided into truss-based, plate-based, and shell-based lattice structures, as shown in Figure 3. All the structures defined here are classified according to the topology of the unit cell, and combinations of these structures in hybrid combinations are also possible [6]. A complete evaluation of the structure concerning energy absorption parameters discussed in section 1.1.1 is required to determine the suitable structure for an energy absorption application.

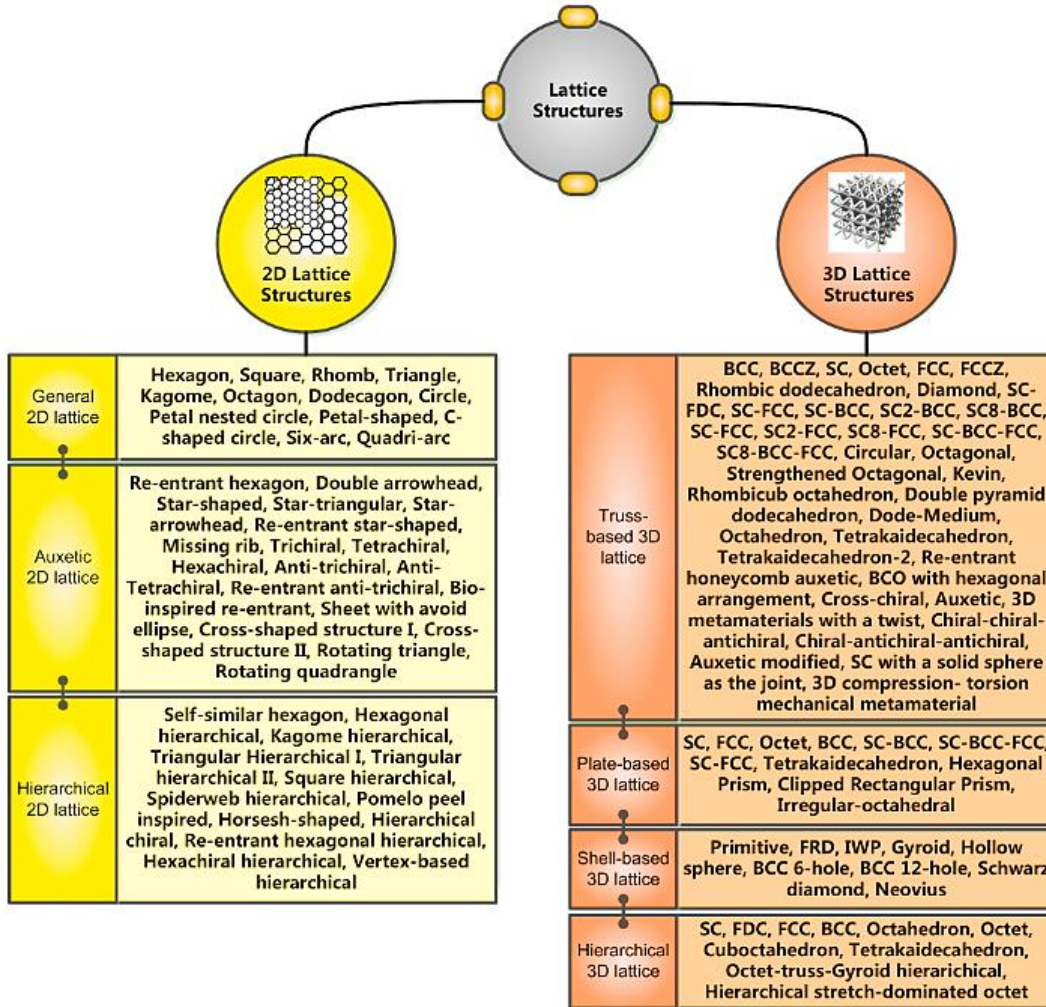


Figure 3. Categories of lattice structures based on cell type and configuration [5].

### 1.1.1 Energy absorption parameters

Several metrics can be extracted from the graph in Figure 4 (a); these are discussed in turn below, with the findings from the literature specific to a metric, woven into the discussion in the appropriate place.

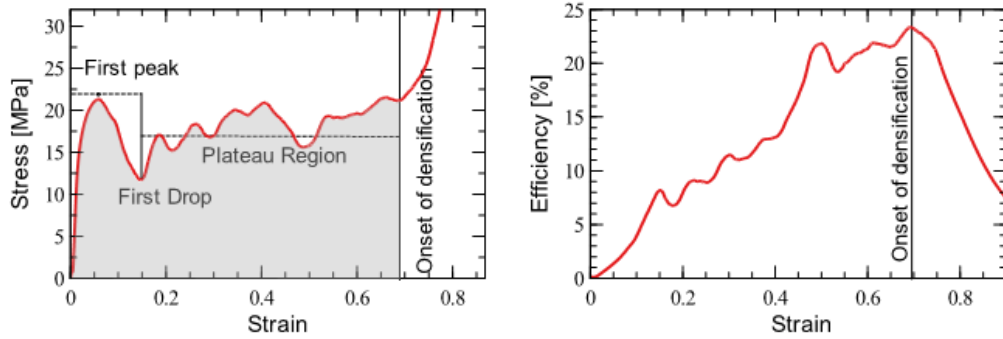


Figure 4. (a) A typical compression Stress-Strain response of a metallic lattice material, showing the first peak, the plateau region, and the onset of densification and (b) Energy efficiency graphed against displacement, with the peak used to identify the one.

- i. First Maximum/Peak Stress: The first maximum stress is the highest stress achieved before a drop in stress levels, as shown in Figure 4 (a). The specific value of this stress depends on the composition, cell geometry, and relative density [7].
- ii. Plateau Stress: The plateau is defined as the region between the first peak stress and the onset of densification. The average stress in the plateau region is defined here as plateau stress. The plateau stress value is lower than the peak stress.
- iii. Plateau slope: The slope of the stress plateau indicates whether the cellular structure hardens or softens under compressive loading. The higher the relative density, the harder the plateau compressive response will be, which can result in the plateau stress exceeding the first maximum stress, which is not ideal from a design standpoint where the goal is often to ensure the maximum transmitted stresses are maintained below a specific value. A cellular material with a flat plateau, across a range of relative densities, is a preferred material for energy absorption. The plateau slope of the P-type TPMS geometry has been shown to be less dependent on relative

density in comparison to other shapes [8], [9]. It has also been shown that two distinct plateaus may be arrived at [10].

- iv. Plateau undulation: Undulation, or waviness in the plateau, is another metric that is of interest and is indicative of the nature of localized failures during the compression event. A nondimensional indicator called Undulation of the Load-carrying Capacity (ULC) has been proposed as [11]:

$$ULC = \frac{\int_0^{S_{EF}} |F(s) - F_m| ds}{\int_0^{S_{EF}} F(s) ds} \quad (1)$$

where  $F$  and  $s$  represent force and displacement, while  $S_{EF}$  and  $F_m$  are the effective stroke and the maximum force experienced in the plateau, not including the first maximum stress. ULC tends to correlate inversely with energy efficiency, with an ideal energy absorber having a ULC value of 0. A drop in plateau load is typically indicative of a localized failure event, occasionally resulting in failure bands and barreling of the cellular structure. Load increases correspond to the transfer of load bearing to another set of members. Higher relative density structures generally have larger undulations on account of thicker beams or walls that tend to experience higher shear stresses. Material properties, including heat treatment induced changes in microstructure, also influence plateau undulation [12].

- v. Onset Strain of Densification: The onset strain of densification ( $\varepsilon_D$ ), which is often less correctly termed simply as the densification strain [13], is vital for the computation of energy absorption. At least four different approaches have been proposed and used to define  $\varepsilon_D$ : (a) The energy efficiency method, where the strain at the maximum energy efficiency point defines  $\varepsilon_D$ , as shown in Figure 4 (b) [14]–

[16]; (b) a predefined strain value at which all values are specified, typically 40% [9] or 50% [17] strain; (c) The use of the first maximum stress as a threshold –  $\varepsilon_D$  is defined when stress exceeds this threshold [18], [19]; and (d) The intersection of the slopes of the plateau and the densification region can be used to define  $\varepsilon_D$  [10], [20]. A detailed discussion on onset strain of densification is given in chapter 3.

- vi. Specific Energy Absorption (SEA): SEA is a normalized (by mass) measure of energy absorbed and is calculated from the stress-strain graph in Figure 4 (a) as:

$$SEA = \frac{\int_0^{\varepsilon_D} \sigma d\varepsilon}{\rho} \quad (2)$$

The numerator is the area under the stress-strain curve integrated up to the densification strain  $\varepsilon_D$ , and  $\rho$  represents the density of the lattice structure. This measure can also be obtained by dividing the area under the force-displacement curve by the measured mass of the lattice structure under compression. The volumetric counterpart of SEA is called energy absorption capacity ( $W_v$ ), with units of J/m<sup>3</sup>. Both these metrics depend on the definition of  $\varepsilon_D$ , and comparisons across the literature must be carefully drawn. Further, both values also typically increase with increasing relative density along with higher transmitted stress, a comparison across shapes is only relevant in the context of relative density and/or maximum transmitted stress.

- vii. Energy Absorption Efficiency: A related metric of interest is the energy absorption efficiency  $\eta$ , which enables a comparison of the energy absorption of cellular material of interest to an ideal energy absorber, for a given maximum transmitted stress  $\sigma_{peak}$ , and is estimated as:



$$\eta = \frac{\int_0^{\epsilon_D} \sigma d\epsilon}{\sigma_{peak} * 100\%} \quad (3)$$

This work attempts to dive deeper into correlating cellular material geometry to the above energy absorption metrics, understand why they have the relationships they do, and propose design strategies for approaching the ideal energy absorber. Instead of focusing on one class of cellular material, this work seeks to compare the behaviors of beam-based lattices and TPMS geometries against baseline honeycombs, all manufactured to similar scales and relative densities using the identical material composition (AlSi10Mg), processing equipment (LPBF), and post-process heat treatments.

### 1.1.2 Ideal energy absorption behavior

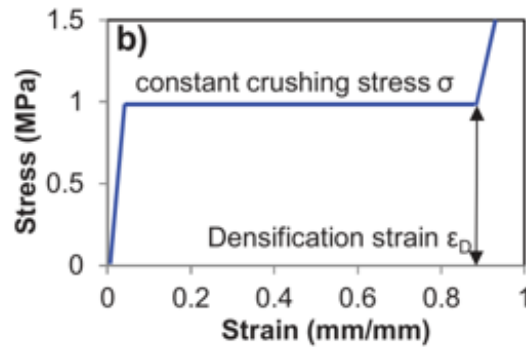


Figure 5. Ideal stress-strain response for maximum energy absorption[19]

As defined by Lu and Yu [4] the ideal energy absorption device should meet the following requirements:

- It should have irreversible energy conversion to avoid secondary impact due to energy release.
- It should have a long stroke to allow large plastic deformation.

- To give a predictable performance, stable and repeatable deformation modes are required.
- It should offer restricted and constant reactive force to ensure the safety of the package.
- It should be easy to manufacture and has high energy absorption.

An ideal energy absorber for the purposes of this discussion is therefore a cellular material that has certain characteristics: (a) a predictable peak stress-relative density relationship, (b) a flat plateau that keeps the stress below the peak stress that will damage the object being protected at a wide relative density range, and (c) the ability for the material to absorb all the energy needed before reaching densification. The stress strain behavior of an ideal energy absorber is shown in Figure 5.

### 1.1.3 Empirical studies

Cellular structures show extraordinary properties like high strength-to-weight ratio, good energy absorption capability [21]. Recently various studies have been undertaken to understand the energy absorption capability of cellular structures. The cellular structures can be further broadly classified as strut-based, surface-based, or ‘shellular’ structures. The strut-based cellular structures such as BCC or Octet-truss exhibit higher strength to weight ratio [22], but due to sharp corners and multiple connections at the node also show stress concentration at the joints which can cause premature failure during large deformation [23]. For the energy absorption application, the nature inspired surface based Triply periodic minimal surface (TPMS) cellular structures are preferred. A minimal surface is defined as

a surface with zero mean curvature at every point. The divergence of the unit normal vector is zero everywhere. When this minimal surface is periodic in three mutually perpendicular directions it is called a Triply periodic minimal surface. A German scientist Schwarz introduced the Schwarz Primitive and Diamond structures in 1865. TPMS structures are defined by rigorous mathematical equations, but for easy modeling and application, trigonometric approximations of those functions are used. The equation and unit cell shape of TPMS structures used in this study are given below.

Gyroid:

$$\sin x \cos y + \sin y \cos z + \sin z \cos x = c \quad (4)$$

Diamond

$$\cos x \cos y \cos z - \sin x \sin y \sin z = c \quad (5)$$

Schwarz Primitive:

$$\cos x + \cos y + \cos z = c \quad (6)$$

where  $x = \frac{2\pi X}{L_x}$ ,  $y = \frac{2\pi Y}{L_y}$ ,  $z = \frac{2\pi Z}{L_z}$ , and  $L_x$ ,  $L_y$ ,  $L_z$  are unit cell sizes in the X, Y, and Z direction respectively. Figure 6 shows graphical representation of the unit cell geometry of Gyroid, Schwarz-Diamond and Schwarz-Primitive structures. Though TPMS structures are defined in 18<sup>th</sup> century the methods to manufacture them with engineering materials were not common. With additive manufacturing TPMS structures are as simple to manufacture as any other structure because of the layer wise approach. Several studies carried out to examine the mechanical properties of the TPMS structures. Table 1 lists a compilation of energy absorption studies conducted on AM cellular materials at quasi-static strain rates in compression.



Figure 6. Unit cell visual representation of TPMS Structures (a) Gyroid structure (b) Diamond Structure and (c) Schwarz- Primitive structure [24].

Table 1. Compilation of quasi-static energy absorption studies in lattice structures manufactured with metal additive manufacturing.

Lattice Geometry	Process and Material	Strain or Displacement Rates	Relative Density Range (%)
BCC lattice [25]	LPBF Stainless Steel 316L	0.25 mm/min	3.5-13.8
Uniform and graded thickness BCC lattice [26]	LPBF AlSi10Mg	1.8 mm/min	22 (nominal)
BCC and BCC-Z lattice [27]	LPBF Stainless Steel 316L	0.5 mm/min	3.5-15.9 (nominal)
Cubic, diamond and re-entrant lattice [28]	EBM Ti6Al4V	0.2 mm/min	13.7 – 16.6
Lattice geometry mimicking C15 Laves phase [10]	LPBF Al-12Si	0.002 s <sup>-1</sup>	17-37 (nominal)
Hollow micro-lattice [18], [29]	Photopolymerization + Nickel coating	1 mm/min	~1.1-32 (nominal)
TPMS double gyroid [30]	LPBF AlSi10Mg	0.54 mm/min	22 (nominal)
TPMS diamond [31]	LPBF AlSi10Mg	0.4 mm/min	5-15 (nominal)
TPMS diamond [15]	LPBF Cu-Cr-Zr copper alloy	Quasi-static, rates not specified	10 – 20 (nominal)
TPMS P-type and G-type [9]	LPBF Stainless Steel 316L	0.001 s <sup>-1</sup>	22.5 – 36.7
TPMS P-type, diamond and gyroid [16]	LPBF Stainless Steel 316L	0.001 s <sup>-1</sup>	10.4 – 31.4

Stacked origami sheet-based materials [14]	LPBF Stainless Steel 316L	0.001 s <sup>-1</sup>	18.9 – 30.5
Bio-inspired cylindrical surface infilled with lattice struts [32]	LPBF AlSi10Mg	1 mm/min	NA

These studies represent a subset of the larger set of experimental studies that have involved compression of cellular materials but are called out here due to their emphasis on extracting energy absorption related information.

#### 1.1.4 Modeling for AM cellular structure deformation

Finite Element Analysis (FEA) simulations are helpful in studying the behavior of lattices and extracting insights not otherwise available from experimental studies. Unit cell simulations are widely used to reduce the numerical expense, but a key question is regarding their appropriateness for modeling energy absorption relevant phenomena. Jia et al. [33] investigated the compressive response of Schwarz primitive structures experimentally and numerically. For FEA simulations, a unit cell model with periodic boundary conditions and the complete model, referred to as the multilayer model, was used. The unit cell was modeled with solid elements, whereas the multilayer model was meshed with shell elements. The difference in the response can be seen in Figure 7. The unit cell model accurately predicts effective yield, but the multilayer approach is required for capturing entire stress strain curve, which is an essential prerequisite for estimating energy absorption metrics from simulation results.

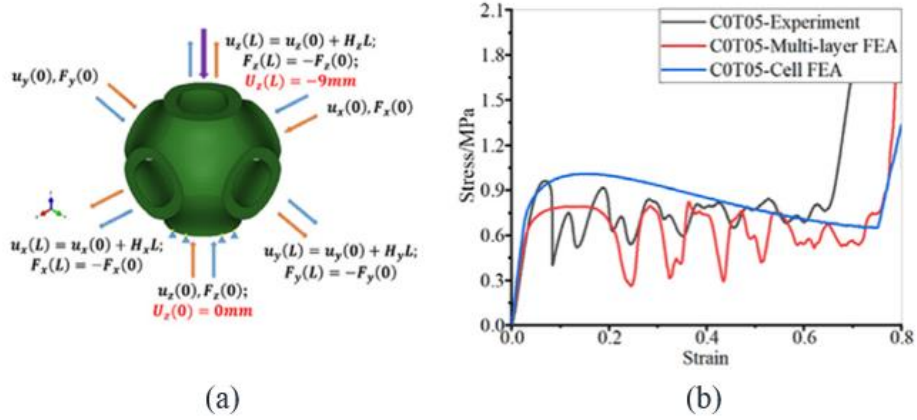


Figure 7. (a) Unit cell representation and multilayer model of schwarz Primitive lattice (b) comparison of stress strain curve obtained with experiment with the unit cell and multilayer simulation. [33]

Another key element of modeling energy absorption behavior is the representation of structure with the appropriate element types and material models. Dejean et. al. [34] investigated octet truss lattices for high energy absorption. The material stainless steel 316L is modeled using rate-independent J2-plasticity model with isotropic hardening. A piecewise linear hardening curve is calibrated using tensile specimens. The complete structure is modeled with linear solid elements. The numerically predicted plateau stress resembles that measured experimentally. Al-Ketan et. al. [35] compared mechanical properties TPMS lattices (Gyroid and Diamond) to those of octet truss lattices. An elastic plastic material model is used with solid elements to simulate unit cells of respective lattices. The sheet-based lattices found to be superior to octet truss lattices due to their stretching dominated deformation. Zhang et. al. [16] studied energy absorption characteristics of stainless steel TPMS structures. The numerical simulation with

Abaqus/Explicit are used to capture complete post yield behavior. The base material is modeled using plastic model with isotropic hardening. Failure model was not included based on the experimental evidence that failure does not occur in the structures. 3D solid elements were used in the study as they show better convergence stability as compared to shell elements. Implicit analysis is also used in linear elastic deformation region to validate. Yang et al [36] used DEFORM-3D software to do numerical analysis of TPMS solid lattices. Elastic-plastic material model with Johnson-Cook strengthening model is used to account for kinematic strengthening of Ti6Al4V. It is concluded that mechanical response of TPMS cellular structures can be described accurately, and stress strain distribution gives accurate explanation for fracture location.

## 1.2. Research Gaps

Through a literature survey of the experimental and numerical studies in the energy absorption of additively manufactured cellular materials the following research gaps were identified in three domains:

- Design Selection: The selection of a particular cellular topology for energy absorption applications remains an empirical study without a designer-oriented methodology for doing so. Further, there is significant disagreement in the identification of the Onset Strain of Densification (OSD), which influences the estimation of critical energy absorption parameters.
- Field-Driven Design: While several publications address quasi-static cellular material energy absorption, designs tend to be based on primitive unit cell shapes

selected *a priori* and arranged periodically in a structure. Limited work was found using design concepts such as gradations for cellular materials. While gradation concepts have been applied in polymeric cellular materials and show some promise, these have been limited to uniform functions that are prescribed and studied empirically – for example, the thickness of the walls varied as a function of  $z$ -position. Limited work was found in the context of energy absorption that uses field- or failure-driven gradation, which allows for a more physics-based approach by relating thickness to a metric such as inelastic dissipation or to the localization of failure bands.

- Modeling & Simulation: Finally, a key challenge in modeling large deformation in additively manufactured cellular materials has not received sufficient study, viz. the efficient, valid, and accurate modeling of variable thickness surface-based cellular structures.

These gaps have motivated the objectives of this thesis.

### 1.3. Thesis Objectives

The thesis aims to develop, implement, and validate a design methodology that enables the realization of cellular structures that approach ideal energy absorption behavior. To achieve that goal, it is essential to achieve the following objectives:

- Determine the key metrics relevant to energy absorption applications and investigate how and why does design influences energy absorption characteristics.



- Develop and validate modeling capability for significant deformation energy absorption behavior of shell-based energy absorbers.
- Develop, implement, and validate a design approach for field-driven graded structures that approach ideal energy absorption behavior.

#### 1.4. Thesis Approach and Scope

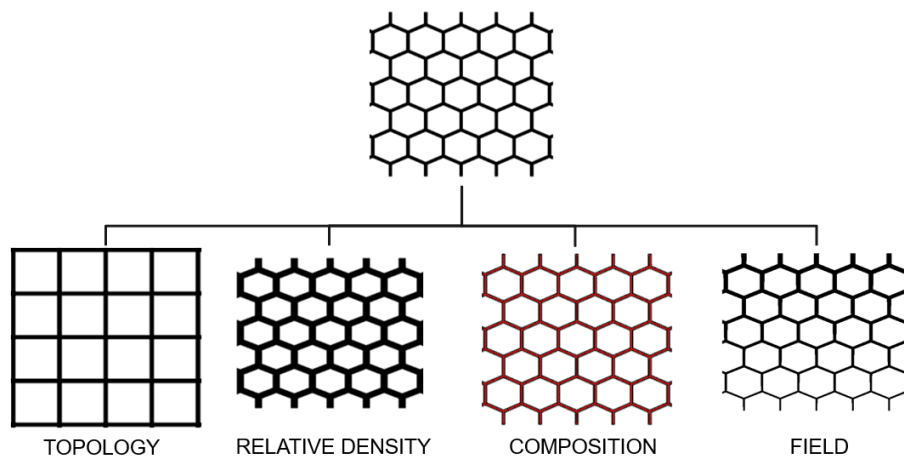


Figure 8. Factors affecting energy absorption for a cellular structure.

Figure 8 shows factors affecting the energy absorption in a cellular structure. An attempt is made to understand effect of each of these factors on energy absorption capacity of the structure. A three-tier system of tasks was established to carry out the required research based on the preliminary tests, analysis, and simulations to achieve these objectives. Each of the following four chapters addresses these topics in turn.

#### *Experimental studies with AlSi10Mg and Nylon-12 Cellular Materials*

To determine the factors governing the force-displacement response of a cellular structure six-unit cells were selected and manufactured in AlSi10Mg (using Laser Powder

Bed Fusion) and Nylon-12 (using Selective Laser Sintering). Three variations of relative density were achieved by changing the thickness of the shell or beam diameter. The obtained force-displacement response was analyzed with compression videos and failure analysis studies to correlate the change in force-displacement response with the failure mechanism in the structure. All the responses were then analyzed for the important parameters related to energy absorption. During this study, three metrics were proposed to aid design selection: (i) a new formulation of the Onset Strain of Densification (OSD), (ii) densification efficiency, and (iii) tunability. Chapter 2 and 3 discusses this work.

*Development of a valid and accurate model for variable thickness surface-based cellular materials*

An effort was made to develop a valid, accurate and efficient finite element model to predict the behavior of cellular structures under quasi-static compression loading. Three important things need to be addressed to develop a reliable and efficient model for predicting the deformation in cellular structure. A suitable material model is required for the prediction of plastic strain in the structure and failure band pattern. Also, an efficient method to represent the geometry accurately is needed for variable thickness modeling, which is a key requirement for enabling field-driven design. The developed models are validated against the test results, and the learnings are used for further research. Chapter 4 dives into the modeling methodology developed in this work.

*Design exploration towards an ideal energy absorber*

This final phase consisted of conceptualizing and analyzing cellular structures to approach an ideal force displacement curve with the help of FEA. The Schwarz-P structure

was selected as a candidate to explore field-driven design concepts on. Several different field-driven approaches were evaluated with the objective of understanding how field-driven design of the entire structure can influence energy absorption performance. Chapter 5 delves into this exploration.

## CHAPTER 2: COMPRESSION BEHAVIOR OF CELLULAR MATERIALS

### Abstract

A designer of metallic energy absorption structures using additively manufactured cellular materials must address the question of which of a multitude of cell shapes to select from, the majority of which are classified as either honeycomb, beam-lattice, or Triply Periodic Minimal Surface (TPMS) structures. Furthermore, there is more than one criterion that needs to be assessed to make this selection. In this work, six cellular structures (hexagonal honeycomb, auxetic and Voronoi lattice, and diamond, gyroid, and Schwarz-P TPMS) spanning all three types were studied under quasistatic compression and compared to each other in the context of the energy absorption metrics of most relevance to a designer. These shapes were also separately studied with tubes enclosing them. All of the structures were fabricated out of AlSi10Mg with the laser powder bed fusion (PBF-LB. or LPBF) process. Experimental results were assessed in the context of four criteria: the relationship between the specific energy absorption (SEA) and maximum transmitted stress, the undulation of the stress plateau, the densification efficiency, and the design tunability of the shapes tested—the latter two are proposed here for the first time. Failure mechanisms were studied in depth to relate them to the observed mechanical response. The results reveal that auxetic and Voronoi lattice structures have low SEA relative to maximum transmitted stresses, and low densification efficiencies, but are highly tunable. TPMS structures on the other hand, in particular the diamond and gyroid shapes, had the best overall performance, with the honeycomb structures between the two groups. Enclosing cellular structures in tubes increased peak stress while also increasing plateau stress undulations.

## 2.1. Design and Manufacturing

The primary aim of this work was to compare energy absorption in cellular materials spanning three categories: honeycombs, beam-based lattices, and TPMS structures.

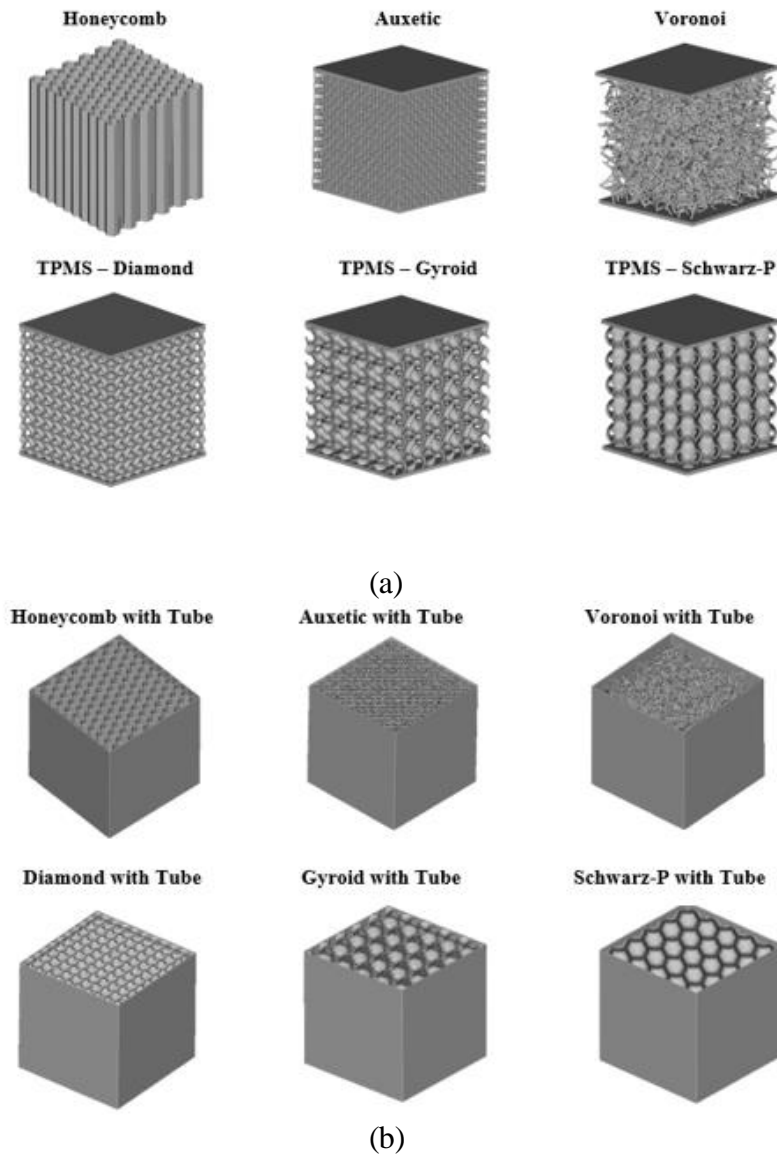


Figure 9. Design of cellular structures used in this study: (a) the six-unit cell shapes used in this study, (b) the same shapes enclosed in a 0.5mm thin tube.

A total of six different cell shapes were selected, as shown in Figure 9 (a): hexagonal honeycomb, auxetic and Voronoi lattices, and diamond, gyroid, and Schwarz-P TPMS geometries. All six of these shapes were fabricated at three different relative densities, by varying beam or wall thickness, as shown in Table 2, within a bounding box envelope of 40 x 40 x 40mm. To resolve the auxetic beam specimens sufficiently, the bounding box envelope for this specific cellular structure had to be increased to 44 x 44 x 44mm. This difference in dimensions was normalized by the computation of effective stresses and strains in the analysis step.

Table 2. Unit cell shapes and relative densities designed for the study.

<b>Unit Cell Shape</b>	<b>Thickness (mm)</b>	<b>Nominal Relative Density (r.d.)</b>	<b>Nominal Mass (g)</b>	<b>Measured Relative Density (r.d.)</b>	<b>Measured Mass (g)</b>	<b>% Difference</b>
Honeycomb	0.4	0.20	34.74	0.19	31.94	-8.05
	0.6	0.30	51.16	0.28	48.18	-5.82
	0.8	0.39	66.84	0.36	63.18	-5.48
Auxetic	0.5	0.08	40.54	0.08	44.85	10.62
	0.75	0.18	61.73	0.17	68.39	10.79
	1	0.29	88.47	0.27	102.83	16.23
Voronoi	0.5	0.03	23.26	0.03	23.09	-0.75
	0.75	0.06	29.94	0.07	31.59	5.53
	1	0.09	38.47	0.12	42.21	9.71
Diamond	0.4	0.16	45.38	0.16	42.43	-6.51
	0.6	0.25	59.56	0.25	53.85	-9.58
	0.8	0.33	73.48	0.32	67.74	-7.81
Schwarz P	0.4	0.13	36.81	0.13	32.85	-10.75
	0.6	0.19	46.59	0.19	42.43	-8.93
	0.8	0.26	56.42	0.25	49.89	-11.57
Gyroid	0.4	0.11	39.28	0.11	34.85	-11.29
	0.6	0.17	50.35	0.17	45.67	-9.30
	0.8	0.23	61.50	0.22	56.49	-8.15

The lowest relative density from each shape was replicated with an enclosing tube as shown in Figure 9 (b). Endplates of 2 mm thickness were created on the top and bottom of all the cellular material specimens, except the hexagonal honeycomb. No endplates were used on the specimens with tubes. A minimum of 10 unit cells in all three directions was used to mitigate against cell size effects [37], [38].

The inclusion of hexagonal honeycombs in this study was to provide a baseline cellular material of the same composition and fabrication process, and due to its well-known benefits as an energy absorber in out-of-plane compression. While BCC lattices have received the most interest in the literature due to their bending-dominated behavior, the auxetic lattice shape was selected due to its promise as an energy absorbing material [39] and limited prior work on energy absorption for metallic auxetics. Auxetic structures are well known for having a negative Poisson's ratio i.e., if a compressive load is applied from x-direction, these structures undergo a reduction in length in the y and z direction as well. The Voronoi lattice shape was also selected due to its stochastic nature similar to metallic foams, which has the potential for the reduced likelihood of failure band formation and smoother plateaus, as well as for reduced anisotropy. TPMS structures in the literature have shown a lot of promise for smoother stress-strain responses and relatively low sensitivity of the plateau slope to changes in relative density [8], and as a result, were selected here. Finally, the end application with cellular materials often involves enclosing them in tubes [20], and as a result one iteration of each design in tubes was also created. Table 2 shows all the shapes and their relative density variations used for the study. For all the surface-based structures, wall thicknesses of 0.4, 0.6, and 0.8 mm were used and for

beam-based structures beam diameters of 0.5, 0.75, and 1 mm were used to keep the relative density below 0.3. To study the effect of adding a tube enclosure, the lowest relative density for each cellular material was selected and enclosed with a 0.5 mm tube to see the change in the collapse pattern as well as change in energy absorption characteristics due to the addition of the tube. All these designs were created using the nTopology Platform software [40]. Table 2 also shows the difference between measured relative density, estimated after weighing the structures and subtracting the design mass associated with the endplates, which were estimated to be at worst within 0.03 from the nominal design.

## 2.2. Manufacturing

All specimens used in this study were manufactured at an established external manufacturing company on a Concept Laser MLab Cusing R machine (GE additive, Cincinnati, OH, USA) equipped with a single 100 W ytterbium fiber laser source. The wavelength and spot size of the laser beam were 1070 nm and 50  $\mu\text{m}$ , respectively, with a continuous scan strategy consisting of a single contour and internal raster. A layer thickness of 15  $\mu\text{m}$  was employed for all specimens. The internal raster had a laser power of 95 W, a scan speed of 550 mm/s and a hatch spacing of 0.105 mm, resulting in a volumetric energy density of 110 J/mm<sup>3</sup>. The contour had a laser power of 95 W and scan speed of 2000 mm/s. These parameters were developed by the supplier for AlSi10Mg on this particular machine and were shown to meet the ASTM F3318 standard [41]. All the parts were stress relieved following recommendations in ASTM F3318 (essentially following the AMS2771 standard [42], only with the temperature set at 285°C for 120 minutes, followed by air-cooling). All specimens with top and bottom endplates were



oriented as shown in Figure 10 (a), whereas specimens enclosed in tubes were oriented as shown in Figure 10 (b). This was done to ensure high part quality by placing flat walls in the vertical orientation. Honeycombs were similarly fabricated with vertical walls. Examples of specimen's post-fabrication and heat treatment are shown in Figure 11

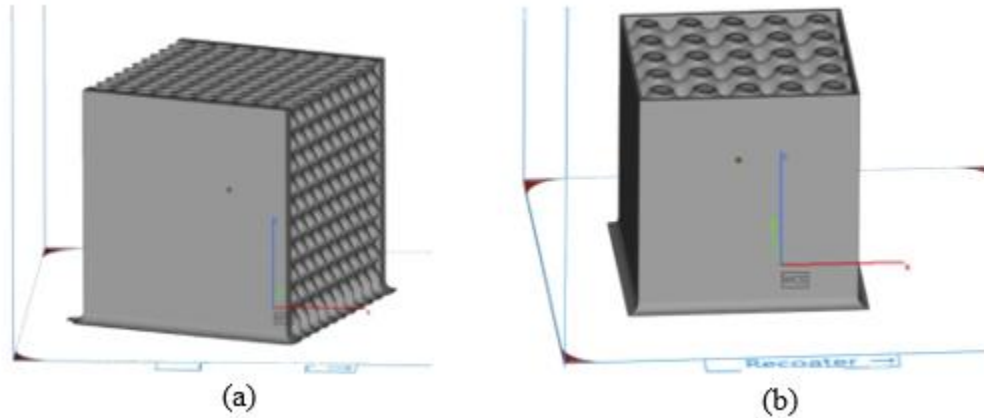


Figure 10. Build orientations of (a) specimens with endplates, and (b) specimens enclosed in tubes.

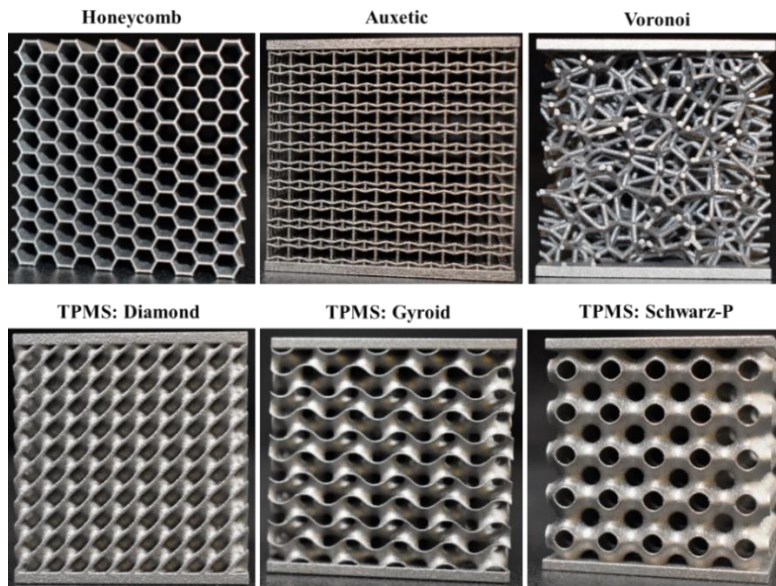


Figure 11. Images of fabricated specimens for each of the six cell types, showing good reproduction of design intent

Prior to mechanical compression, all specimens were weighed on an analytical balance with a 0.0001g resolution, and mass results are shown in Table 2. These mass measurements were compared to the estimated mass in the nTopology software by assuming a density of AlSi10Mg as 2.68 g/cm<sup>3</sup>, and differences estimated as an approximate measure of how closely the manufactured cellular structures conformed to designed geometries. Most mass errors were within 10%, except for the auxetic lattices which were 10-17% heavier than nominal design predictions. Measured relative density values reported in Table 2 were estimated with the assumption that all mass variations accrue to the cellular members alone, as opposed to the endplates, or in the case of specimens enclosed in tubes, to the tube walls.

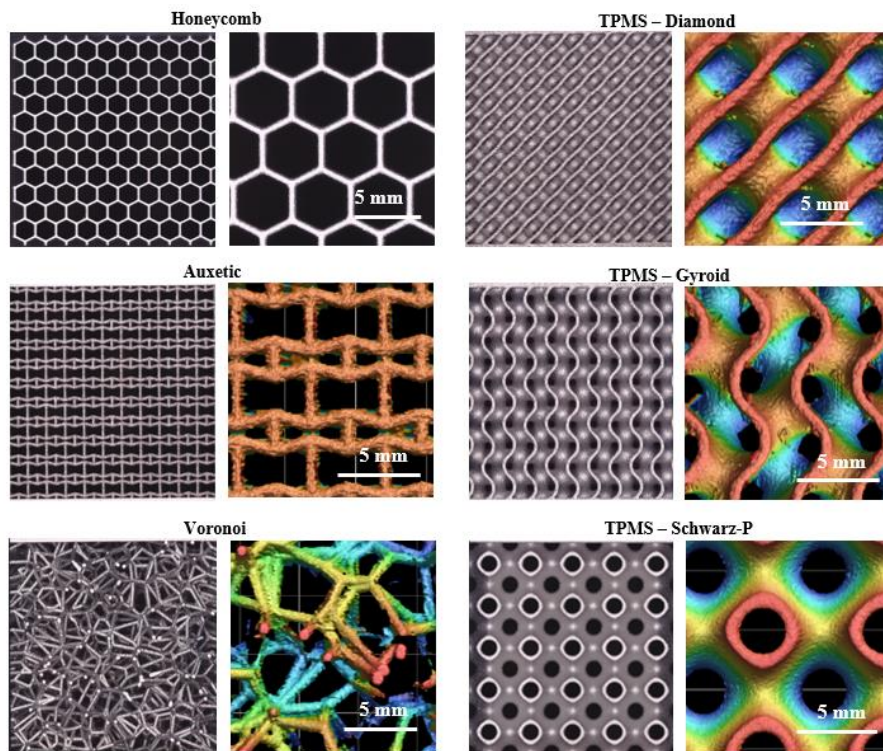


Figure 12. Scanning microscope optical images, and height maps of the specimens fabricated, showing print quality and resolution.

To ascertain the causes for deviation in mass calculations, specimens were examined under a Keyence V-3200 optical scanning microscope. Optical and height data from the microscope for each of the six shapes in this study are shown in Figure 11. Inspection of the auxetic specimens clearly shows significant roughness on the beams, the majority of which are low angle overhanging beams. The additional mass may be attributed to this surface morphology, which is also borne out by the Voronoi, which has a more variable distribution of beam orientation but does also show higher mass values than designed, particularly at higher relative densities. All subsequent discussions of relative density thus leverage experimental, instead of nominal values.

### 2.3. Test Setup

Quasi-static compression testing was carried out on all cellular materials using an Instron 5985 universal testing machine load frame with a load capacity of 250 kN at a constant displacement rate selected to effectively generate a strain rate of  $10^{-3} \text{ s}^{-1}$ . The loading direction was perpendicular to the endplates and along the direction of the walls of the tubes. Honeycombs were compressed out-of-plane. Stress and strain calculations were made based on area and specimen height estimates from the bounding box volumes, with the thicknesses of the endplates subtracted for height calculations. A 50 N preload was applied on each specimen prior to application of the specified displacement rate.



Figure 13. Instron Universal testing machine, Camera set up for compression tests.

The deformation patterns of the cellular structures were recorded via two digital SLR video cameras at an image capture frequency of 1Hz. The cameras were set at right angles to each other as shown in Figure 12. Rectangular stainless-steel platens were used on the compression machine with no lubrication between platens and specimen surface.

## 2.4. Results

### 2.4.1 Hexagonal Honeycomb

As shown in Figure 13 (a), out-of-plane compression of the hexagonal honeycombs with three different wall thicknesses (and associated relative densities) all show evident peak stress, followed by a plateau region. The 0.8 mm thickness specimen was tested on a 500 kN load frame since it was calculated to exceed the 250 kN load capacity for the machine used for testing all the other specimens. An examination of the stress-strain response reveals that the stress reaches a first maximum for all three shapes between an effective strain of 0.1-0.2. This is primarily the result of top and bottom surface crimping,

as visible in Figure 13 (b) for a strain of 0.2. The 0.6 mm wall thickness specimen shows a significant drop in the peak stress with a large first dip, which is associated with the formation of an inclined failure band in the structure, after which point the stress drops rapidly. In contrast to the other specimens studied in this work, the honeycomb is a prismatic structure and frequent stress rises and drops are not visible, with failure bands not materializing layer by layer, and instead forced to form along inclined planes.

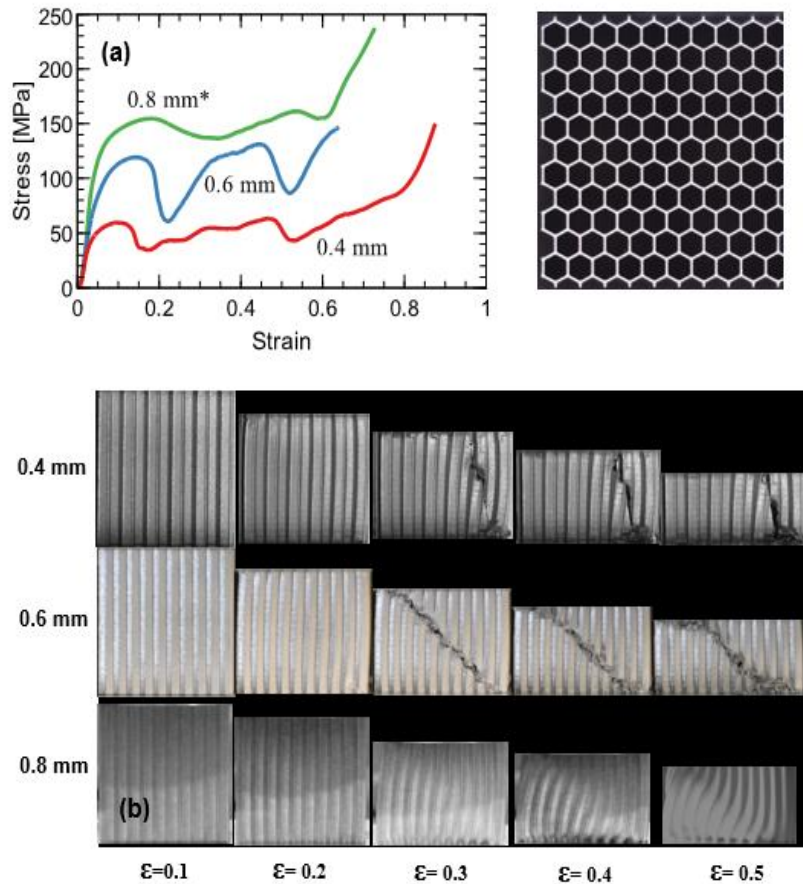


Figure 14. (a) Stress-strain curves for honeycomb compression with 0.4, 0.6- and 0.8-mm thickness (\*the 0.8mm specimen was tested on a different mechanical load frame), (b) honeycomb deformation for each of the three thicknesses at increasing strain.

As shown in Figure 14, for the 0.8 mm thick honeycomb, the failure bands result in fracture, and further, are not visible on every surface. Except for the 0.6 mm wall thickness



specimen, the honeycombs show reasonably good behavior, consistent with their well described properties as energy absorbers: they demonstrate a clear first peak and a plateau, and at low relative densities, seem to have delayed onset strain of densification. The honeycomb specimens also establish a baseline for comparison to the lattice- and TPMS-based geometries.

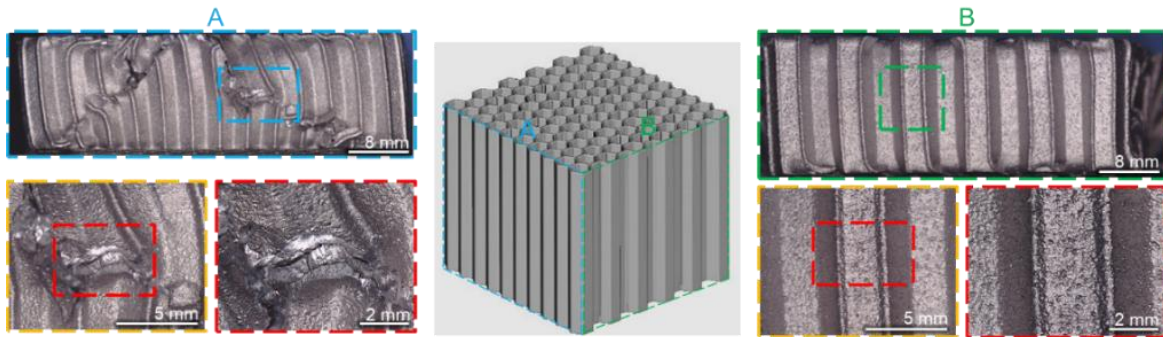


Figure 15. Failure analysis on two surfaces of the 0.8mm wall thickness honeycomb (r.d. of 0.36), showing two inclined failure bands and lateral fractures in the wall evident on surface A; wall crimping visible on surface.

#### 2.4.2 Auxetic Lattice

The auxetic lattice, of all the structures in this study, showed the highest undulations in the plateau region, with each load drop coinciding with a collapse of an entire row of beams, as shown in Figure 16 (a) and (b). A visual comparison of the auxetic lattice and the prior honeycomb stress-strain response immediately suggests that the auxetic shape is a poor candidate for an energy absorber. The auxetic shape has parallel beams in the direction of loading which resist the load till it exceeds the critical buckling load. The entire row, on collapse, effectively then shears sideways. As seen in Figure 16 for the densest auxetic lattice in this study, in addition to row-by-row densification, inclined failure bands

also form, which were not visible for the lower density specimens. Finally, the onset strain of densification for all three relative density specimens is at or under 0.4, suggesting poor overall energy efficiency for the auxetic lattices.

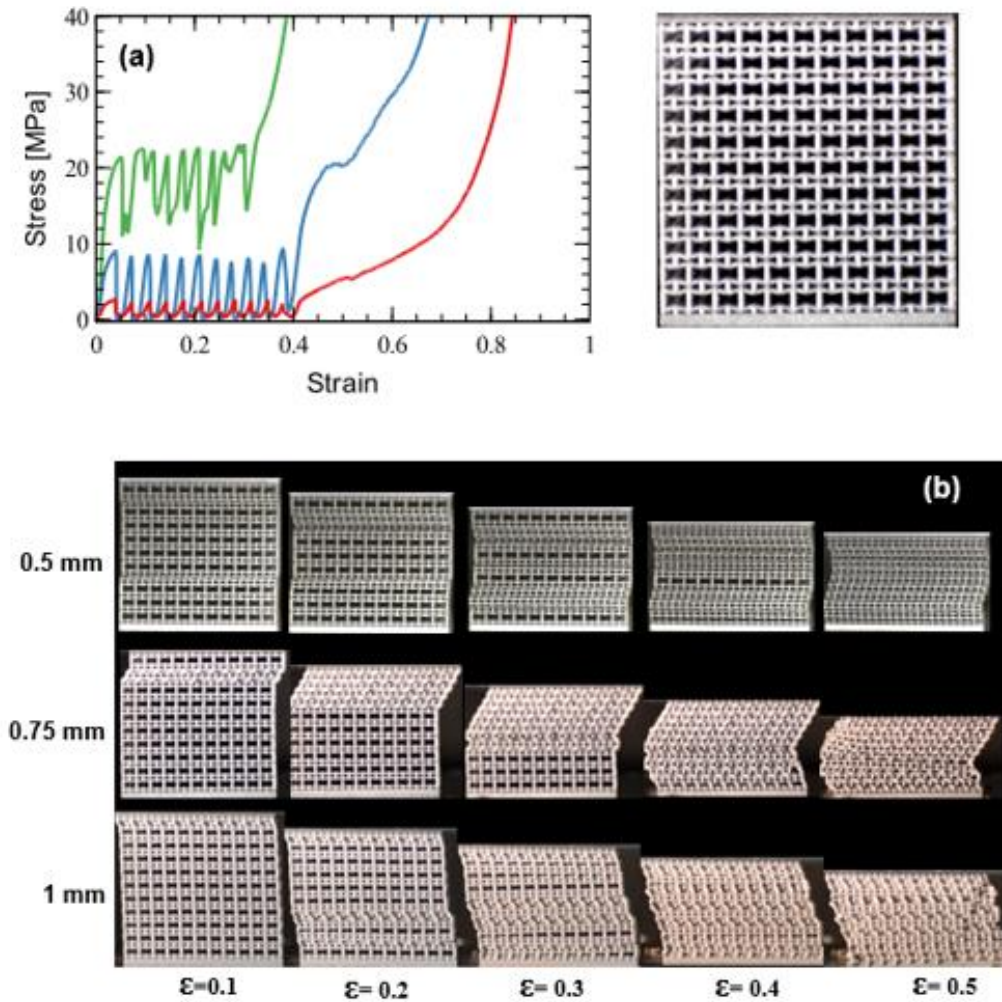


Figure 16. (a) Stress-strain curves for an auxetic lattice shape under compression with 0.5, 0.75 and 1mm beam diameters, (b) auxetic lattice deformation sequence for each of the three beam diameter specimens at increasing strain.

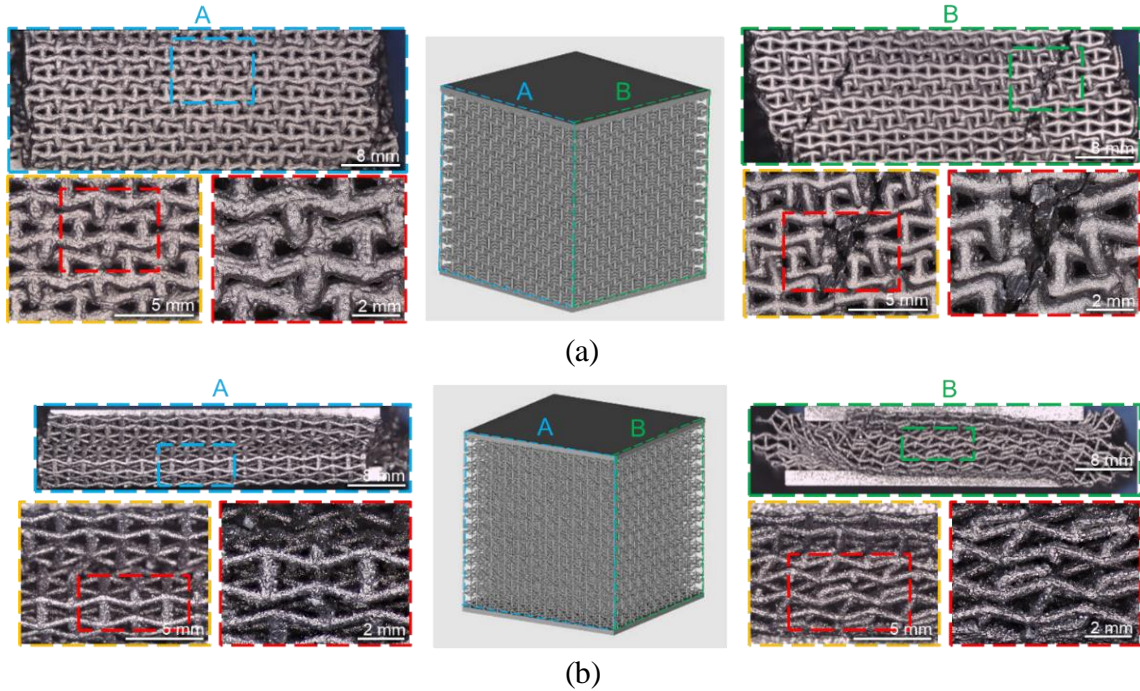


Figure 17. Failure analysis on two surfaces of the auxetic lattice: (a) for the 0.5mm beam diameter specimen (r.d. of 0.08), surface A shows beams collapsing and closing the re-entrant cell space, surface B shows shearing of planes; (b) the 1mm beams (r.d. of 0.27)

### 2.4.3 Voronoi (Stochastic) Lattice

In contrast to the auxetic lattice, the Voronoi or stochastic lattice shows a much smoother stress-strain response, as seen in Figure 18. The Voronoi structure has struts oriented in multiple directions with cell centroids randomly positioned so as to not emerge in the same plane (Figure 18), in contrast to the auxetic lattices. Compared to the auxetic lattices, the Voronoi lattices have a higher onset strain of densification. For example, Figure 18 shows a post-compression Voronoi lattice with a relative density of 0.07, which is slightly lower than that of the auxetic lattice shown in Figure 16 (a) (relative density of 0.08) yet has an onset strain of densification that is almost 50% higher than that of the auxetic structure.



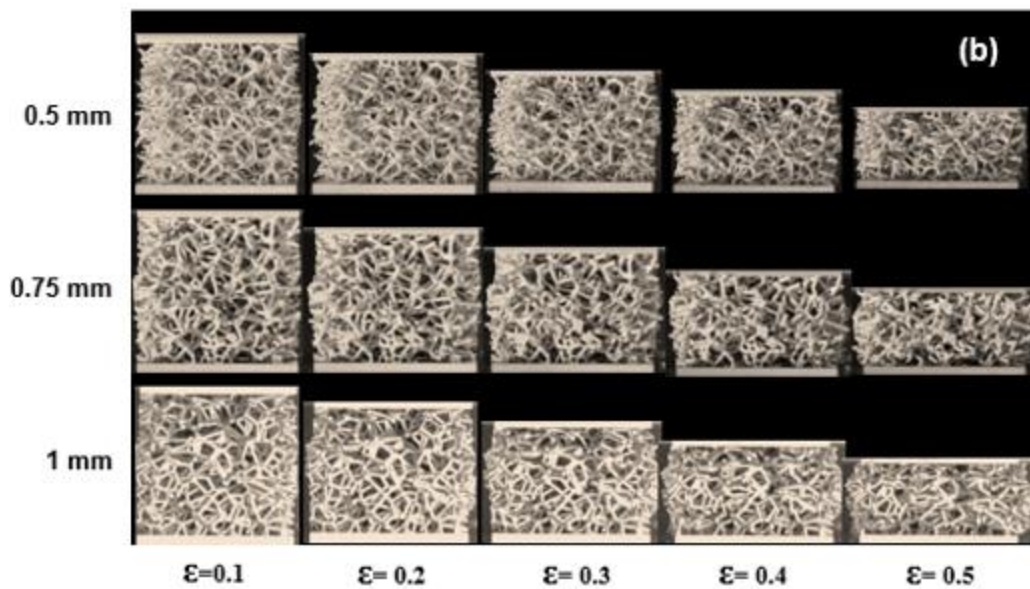
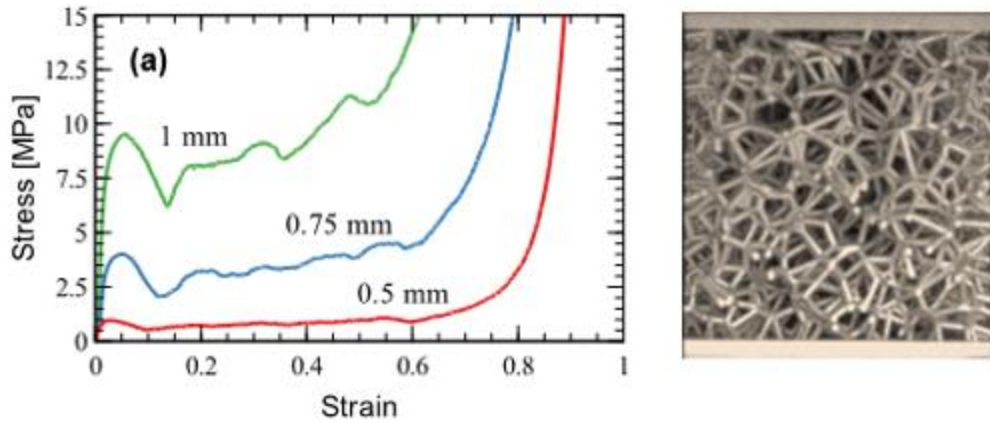


Figure 18. (a) Stress-strain curves for Voronoi lattice shape under compression with 0.5, 0.75, and 1mm beam diameters, (b) Voronoi lattice deformation sequence for each of the three beam diameter specimens at increasing strain.

The Voronoi lattice does however demonstrate a hardening tendency as relative density increases, and a significant first dip for all but the least dense of the specimens studied. The introduction of aperiodicity into lattice structures is thus helpful in preventing localization of failure bands and the resulting undulations in the stress plateau, but at the

same time does not assure a flat plateau that is required to ensure energy is absorbed at transmitted stress levels under the first maximum.

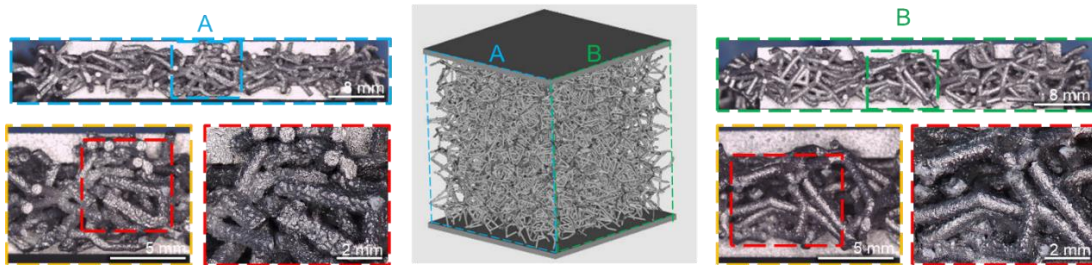


Figure 19. Failure analysis on two surfaces of the 0.75mm beam diameter Voronoi lattice (r.d. of 0.07)

#### 2.4.4 Schwarz-P TPMS

The Schwarz-P TPMS compressive response, shown in Figure 19 (a), resembles that of the honeycomb, with greater undulations at the highest relative density. This is attributable to the formation of localized failure bands as seen in Figure 19 (b), with each drop in stress coinciding with an inclined failure band localizing. All three specimens show slight hardening in the stress plateau before densification. An examination of the post-compression failure images in Figure 20 shows significant fracture at the extreme ends of the relative densities explored, with the 0.6mm wall thickness (relative density of 0.17) showing fewer fracture surfaces, corresponding to a smoother stress plateau.

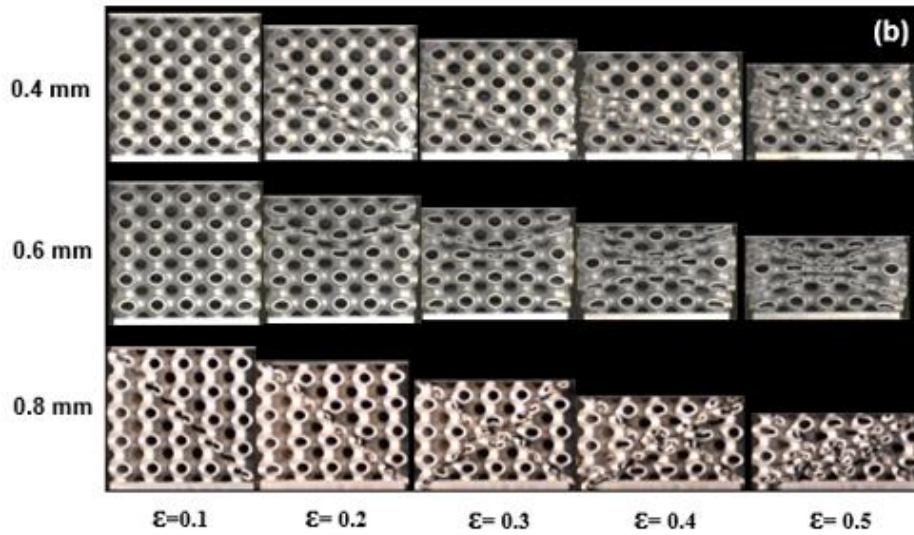
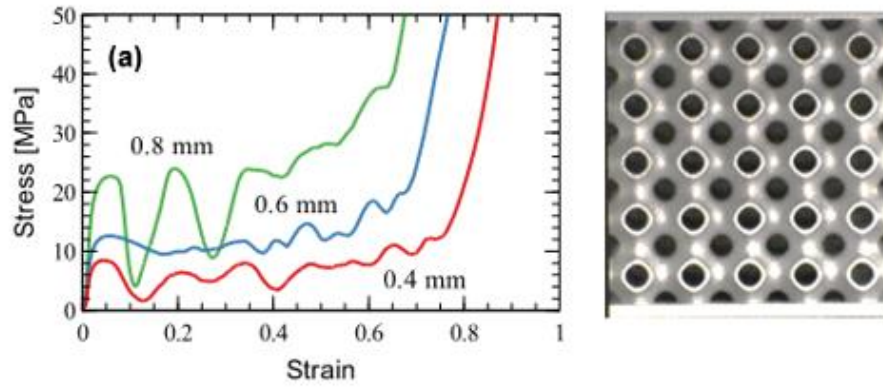
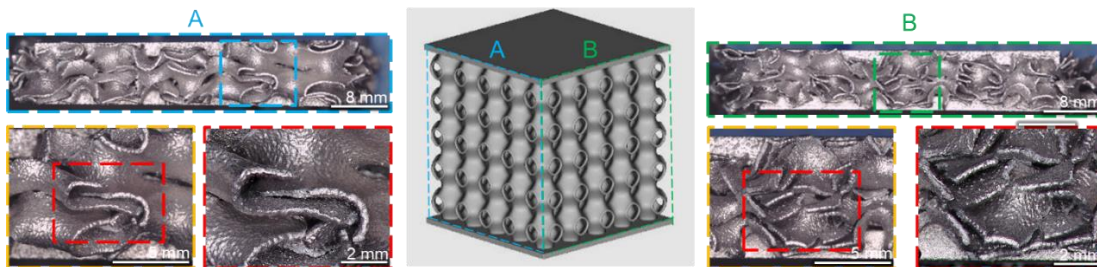


Figure 20. (a) Stress-strain curves for Schwarz-P TPMS structure under compression with 0.4, 0.6, and 0.8mm wall thicknesses, (b) Schwarz-P TPMS deformation sequence for each of the three wall thickness specimens at increasing strain.



(a)



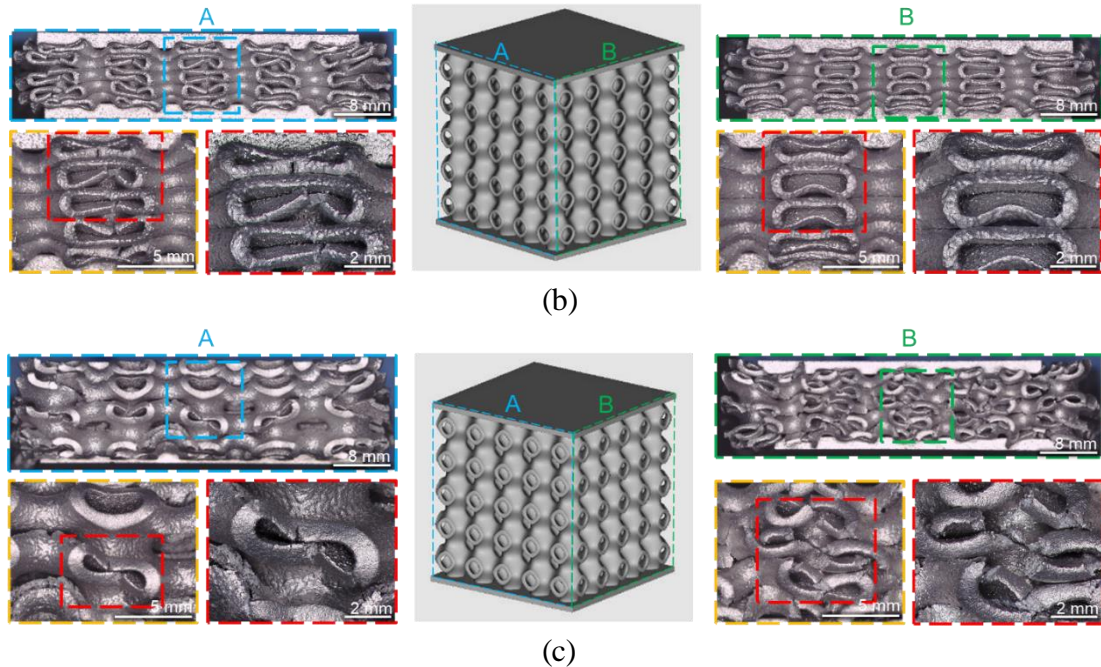


Figure 21. Failure analysis on two surfaces of the Schwarz-P TPMS structure for three different wall thicknesses/relative densities: (a) 0.4mm/0.11 r.d.; (b) 0.6mm/0.17 r.d.; (c) 0.8mm/0.22 r.d.

#### 2.4.5 Diamond TPMS

As shown in Figure 21 (a), the diamond TPMS compressive response is similar to that of the Schwarz-P, a key difference being that even at the highest relative density (0.25) the stress plateau is relatively smooth, in comparison to the Schwarz-P. While a failure band does form for the diamond TPMS, as seen in Figure 21 (b), the band involves sliding over cell walls along the shear plane, as opposed to complete cell-level collapse seen in the Schwarz-P specimens. This is also evident from a comparison between the failure images shown in Figures 20 (Schwarz-P) and 22 (diamond). The diamond TPMS compression curves have lower undulations and flatter plateaus in comparison to the Schwarz-P. The diamond TPMS geometries show barreling effects, particularly at higher relative densities,

which is not seen for Schwarz-P geometries, consistent with other findings in the literature [8].

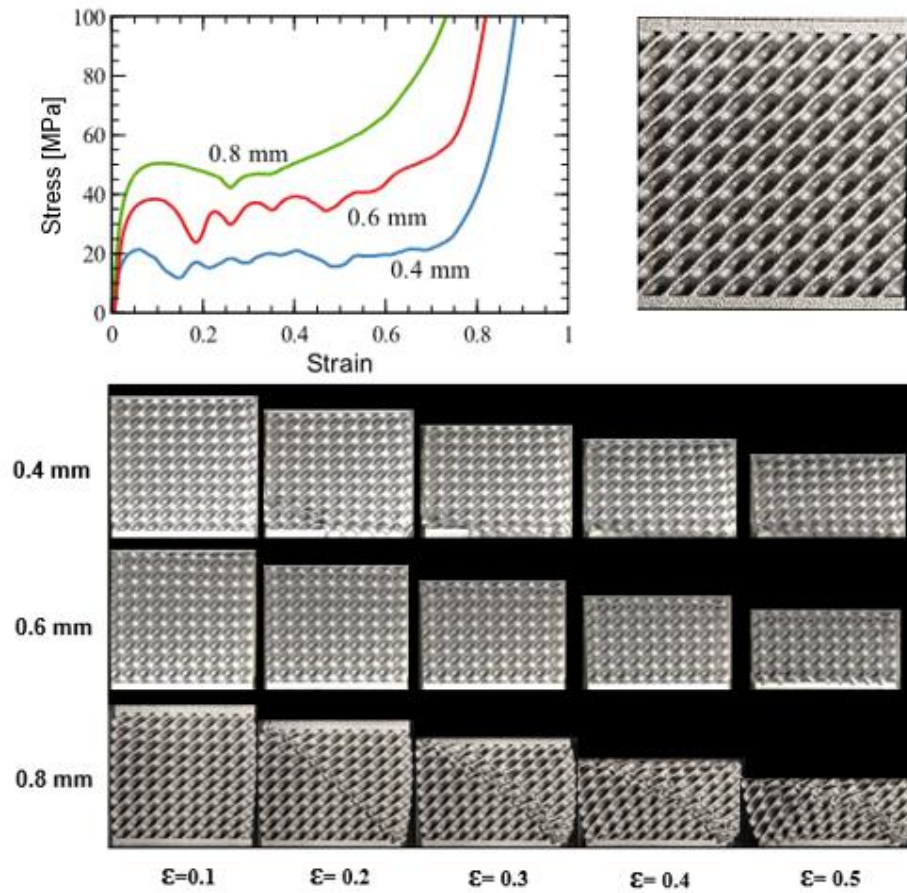


Figure 22. (a) Stress-strain curves for diamond TPMS structure under compression with 0.4, 0.6 and 0.8mm wall thicknesses, (b) diamond TPMS deformation sequence for each of the three wall thickness specimens at increasing strain.

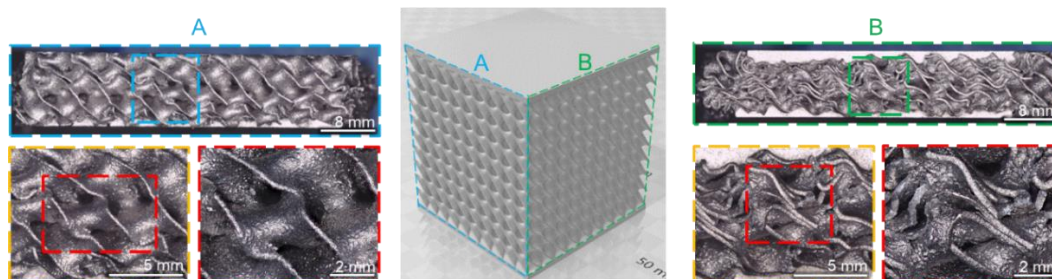


Figure 23. Failure analysis on two surfaces of the diamond TPMS structure for 0.4mm wall thickness /0.13 r.d. showing cell walls.

## 2.4.6 Gyroid TPMS

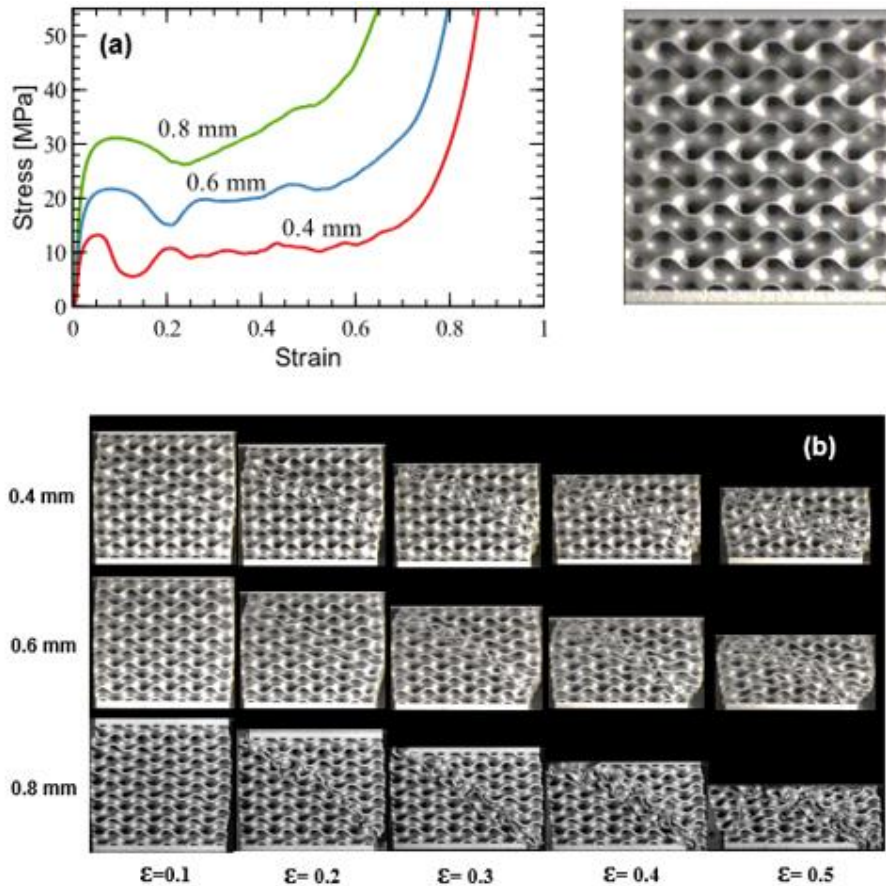


Figure 24. (a) Stress-strain curves for gyroid TPMS structure under compression with 0.4, 0.6, and 0.8mm wall thicknesses, (b) gyroid TPMS deformation sequence for each of the three wall thickness specimens at increasing strain.

The gyroid TPMS compression response, shown in Figure 23 (a), shows relatively flat plateaus with clear hardening only evident for the highest relative density studied (0.25). A clear drop in stress is evident after the first maximum, at strain values between 0.1 to 0.3. All specimens show barreling, shown in Figure 23 (b), similar to the diamond TPMS. Examining the two surfaces of the post-compression specimen in Figure 24 shows both plastic yielding and fracture are observed in the gyroid specimens.

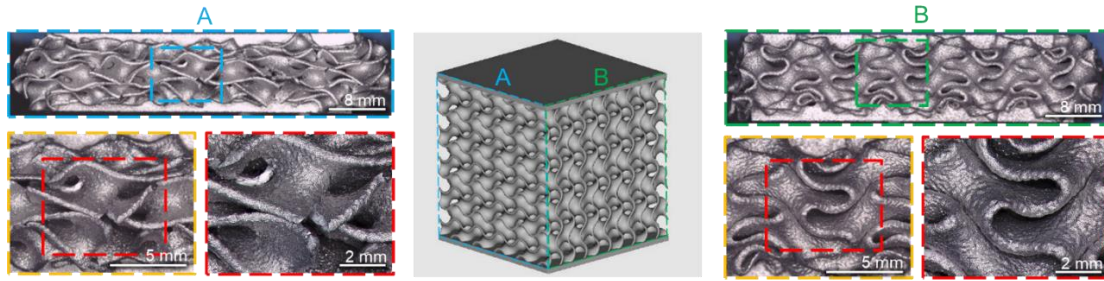


Figure 25. Failure analysis on two surfaces of the diamond TPMS structure for 0.4mm wall thickness /0.13 r.d. showing cell walls.

## 2.5. Analysis

### 2.5.1 Specific Energy Absorption and Transmitted Stress

The most commonly used criterion to assess the performance of an energy absorption material is its Specific Energy Absorption (SEA). SEA estimations are dependent on the assumption made on the upper bound of the strain value used to calculate them. In this work, the energy efficiency approach is used, where the maximum energy efficiency defines the onset strain of densification. (Chapter 3 will delve deeper into the calculation of onset strain of densification using an improved method which was developed on completion of the work discussed in this chapter.)

SEA, which increases with relative density, is best viewed in the context of the maximum transmitted stress, which from a designer's perspective, is not just the initial maximum stress, but the true maximum during the portion of the stress-strain response utilized in the SEA calculation [43]. Following this approach, SEA vs. the normalized maximum stress (divided by AlSi10Mg yield strength) is shown in Figure 25 (a). An ideal energy absorber in this context would lie in the upper left corner, with high SEA at low



maximum transmitted stresses. The trend line indicates that relative to the other cellular materials in the study, the TPMS geometries performed well, and the lattice geometries performed poorly. The honeycombs tested showed little change between SEA and relative density. Once the honeycombs are removed from the dataset, and the graph is replotted, as shown in Figure 25 (b), the prior observation differentiating TPMS from lattice structures is clearly borne out. Another method of viewing SEA data is by plotting it against the maximum transmitted stress up to a given point through the compression event, as shown in Figures 25c for all three TPMS geometries tested in this study.

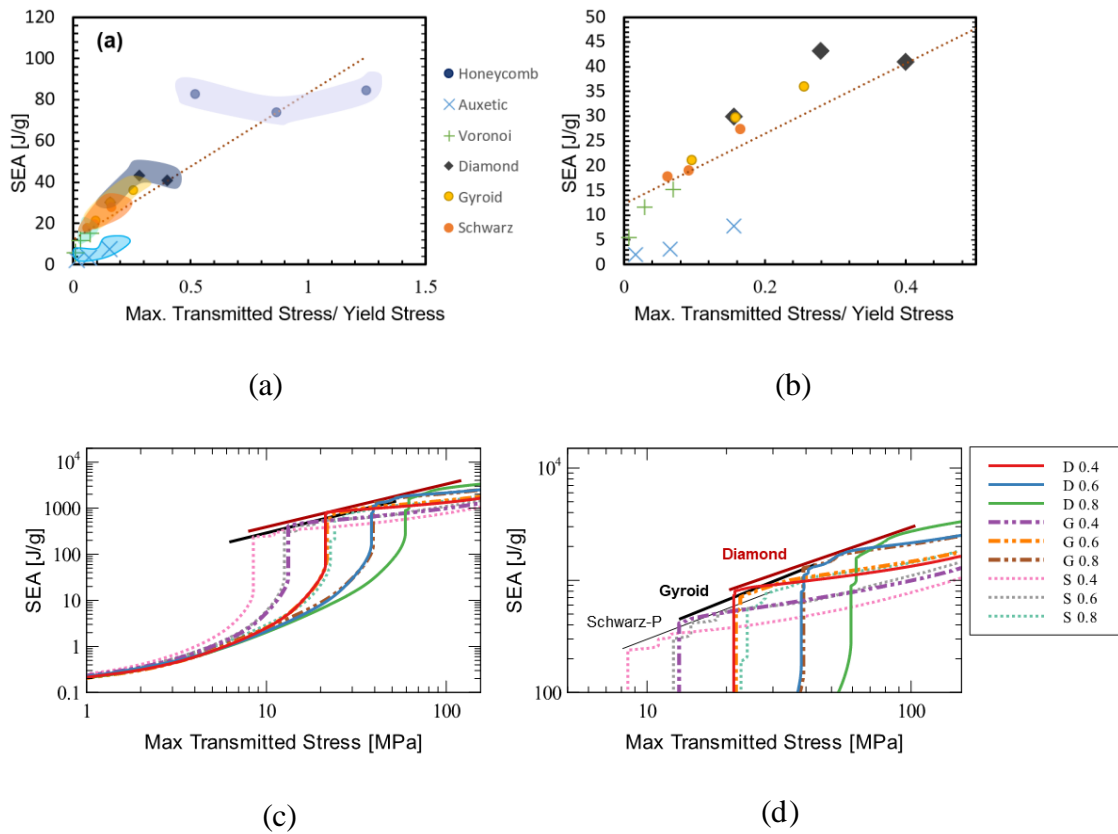


Figure 26. (a) comparison of SEA vs normalized max transmitted stress (b) Zoomed in view of lower left corner (c) Logarithmic plot of Energy absorbed per unit mass against maximum transmitted stress till structure absorbs that energy. (d) zoomed in view of the upper right corner of plot c



### 2.5.2 Densification Efficiency

As described before, the onset strain of densification is an important metric in energy absorption, not just since it influences the estimation of SEA, but also since it is indicative of the usable stroke length in a compression event. As with SEA, the onset strain of densification for a given cellular shape is a function of its relative density, making direct comparisons between shapes challenging. An ideal energy absorber, in principle, would delay the onset strain of densification till such time as all that remains in the compressed material is fully dense, and all “negative” or empty space [44] is eliminated – this is not strictly true since structures do demonstrate bulging and at very high strains push material outside the initial bounding box volume. Nevertheless, one may define a densification efficiency ( $\eta_D$ ) in terms of the onset strain of densification ( $\epsilon_D$ ) and the relative density ( $\rho^*/\rho_s$ ) as:

$$\eta_D = \frac{\epsilon_D}{1 - \frac{\rho^*}{\rho_s}} \quad (7)$$

Thus, an ideal energy absorber would have a densification efficiency of 1 or 100%. For the 18 specimens in this study, densification efficiencies are shown in Figure 27. Once again, it is evident that the beam-based cellular structures have low densification efficiency, but the honeycombs and TPMS structures exceed 70%, with the Diamond showing the highest mean value, and the Schwarz-P showing the least variability across relative density values.

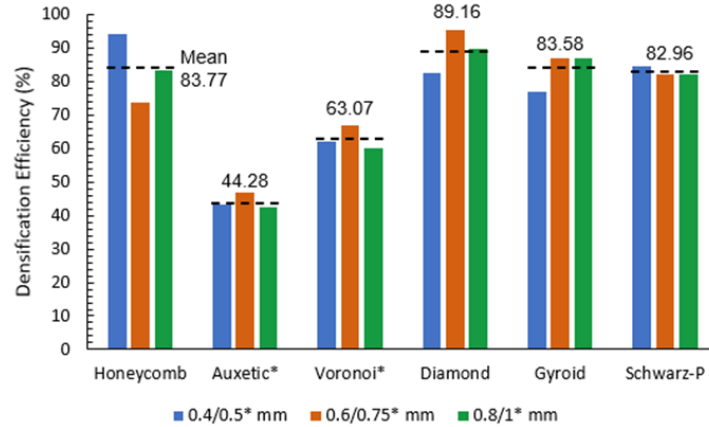


Figure 27. Comparison of densification efficiencies for each of the six shapes and three relative densities

To get a sense of the physical reasons underlying why a particular shape has a specific densification efficiency, it is useful to examine the compressed structure at the instant corresponding to the onset strain of densification, as shown in the compilation in Figure 27. An examination of the auxetic and Voronoi lattice structures shows significant negative space retained between struts at densification, explaining their low densification efficiencies. The 0.4mm honeycomb has the highest densification efficiency, but this is at least in part due to the lateral (horizontal) spreading of the collapsed structure, which also explains the higher  $\varepsilon_D$  value for the 0.8 mm thick gyroid. The diamond and Schwarz-P structures, while demonstrating some barreling, show limited lateral spread.




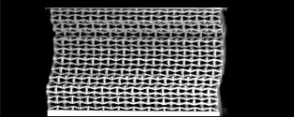
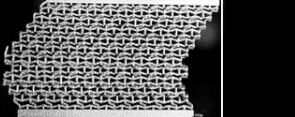
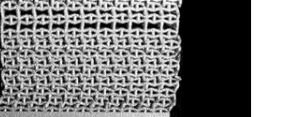
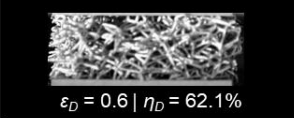
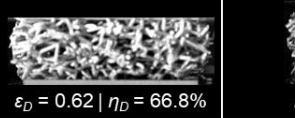
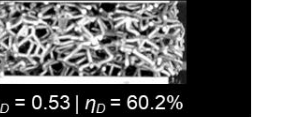
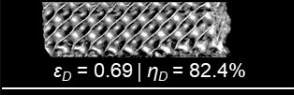
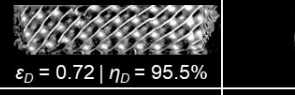
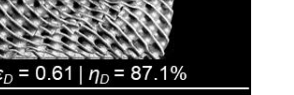
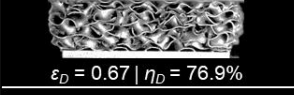
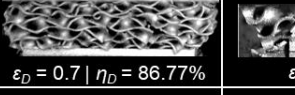
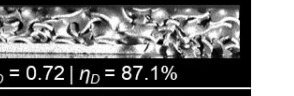
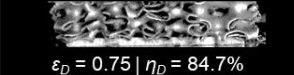
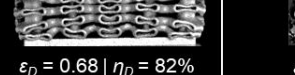
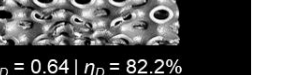
Thickness Shape	0.4/0.5*	0.6/0.75*	0.8/1*
Honeycomb	 $\epsilon_D = 0.76 \mid \eta_D = 94.1\%$	 $\epsilon_D = 0.53 \mid \eta_D = 73.7\%$	 $\epsilon_D = 0.61 \mid \eta_D = 92.2\%$
Auxetic*	 $\epsilon_D = 0.4 \mid \eta_D = 43.5\%$	 $\epsilon_D = 0.39 \mid \eta_D = 46.9\%$	 $\epsilon_D = 0.31 \mid \eta_D = 42.5\%$
Voronoi*	 $\epsilon_D = 0.6 \mid \eta_D = 62.1\%$	 $\epsilon_D = 0.62 \mid \eta_D = 66.8\%$	 $\epsilon_D = 0.53 \mid \eta_D = 60.2\%$
Diamond	 $\epsilon_D = 0.69 \mid \eta_D = 82.4\%$	 $\epsilon_D = 0.72 \mid \eta_D = 95.5\%$	 $\epsilon_D = 0.61 \mid \eta_D = 87.1\%$
Gyroid	 $\epsilon_D = 0.67 \mid \eta_D = 76.9\%$	 $\epsilon_D = 0.7 \mid \eta_D = 86.77\%$	 $\epsilon_D = 0.72 \mid \eta_D = 87.1\%$
Schwarz-P	 $\epsilon_D = 0.75 \mid \eta_D = 84.7\%$	 $\epsilon_D = 0.68 \mid \eta_D = 82\%$	 $\epsilon_D = 0.64 \mid \eta_D = 82.2\%$

Figure 28. Deformation of cellular structures at the densification strain is mentioned below the picture of individual cellular shapes.

### 2.5.3 Plateau Undulation

Undulations in the stress plateau have the undesirable effect of limiting SEA (relative to a perfectly flat plateau) and/or generating higher stresses than the initial first maximum stress. In addition, undulations could signal poor repeatability, resulting in more conservative designs to account for the higher uncertainty. In this sub-section, the first dip and plateau range terms introduced previously are evaluated, after normalizing them by plateau stress, and plotted in Figure 29 (a) and (b), respectively. The auxetic shape has the highest undulation as measured by both metrics, followed by the Schwarz-P. The

remaining shapes, including the Voronoi lattice, are fairly similar in their undulation behavior. The stochastic nature of the Voronoi lattice, with beams at multiple orientations relative to the loading direction, smoothens the plateau relative to the auxetic shape.

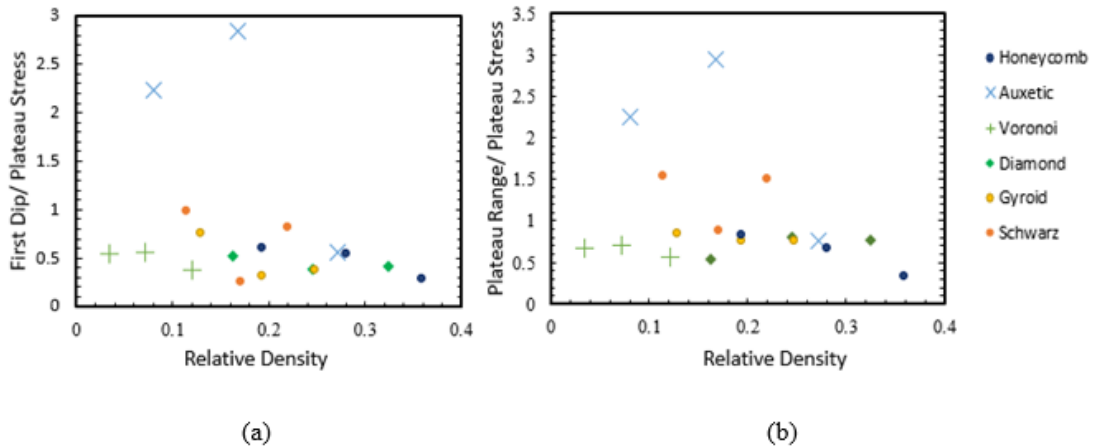


Figure 29. Plateau undulation quantified as (a) normalized first dip, and (b) normalized plateau range.

#### 2.5.4 Tunability

Tunability represents the designer's ability to use a particular shape and relative density to meet certain requirements with a high degree of confidence. In the context of a metallic energy absorber, it typically has to withstand static, in-use loads, as well as absorb energy when needed during the impact event. For the former, it is vital that the designer be able to predict the effective modulus, for the latter, it is vital to predict the maximum transmitted stress and the SEA. All three of these metrics (the first two normalized) are shown in Figure 30 (a), (b), and (c), respectively, as a function of relative density. Empirical power-law fits are demonstrated for all three metrics, and the accompanying table provides the fit parameters as well as the quality of the fit as measured by its  $R^2$  value, for each

shape studied. For the effective modulus and the maximum transmitted stress, the  $R^2$  value for all shapes is well over 0.75, indicating a strong correlation between the metric of interest

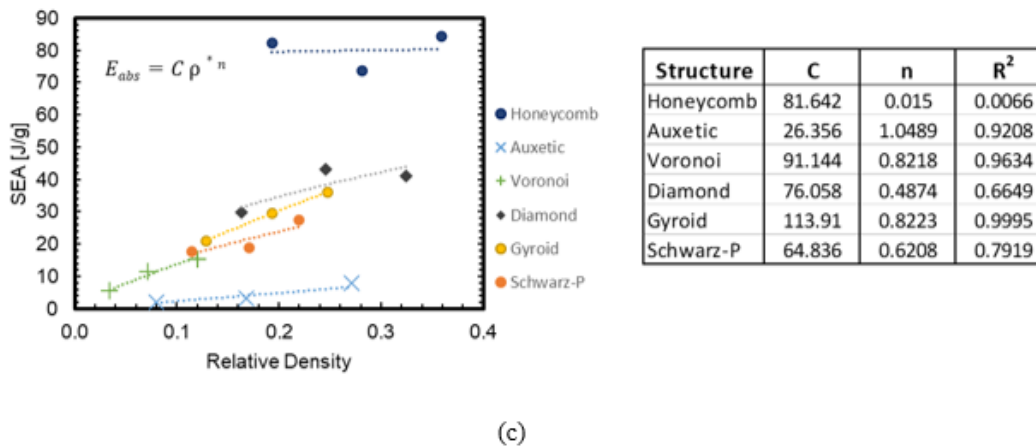
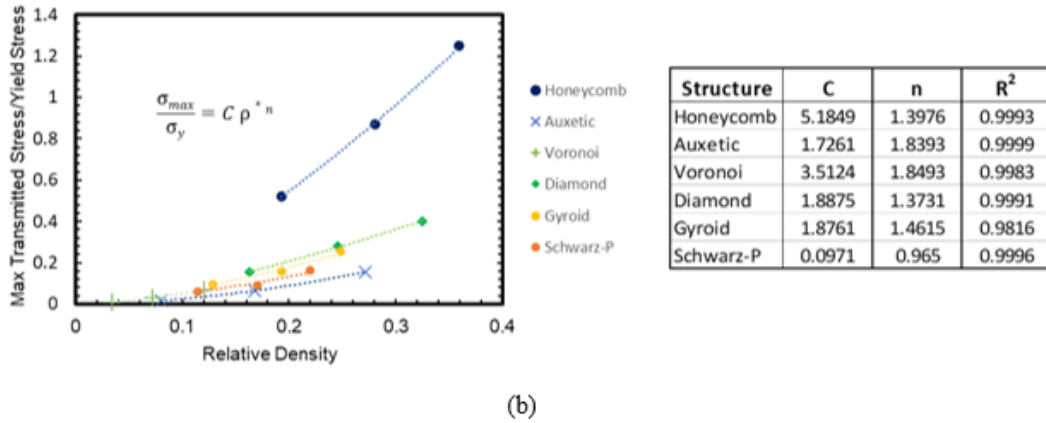
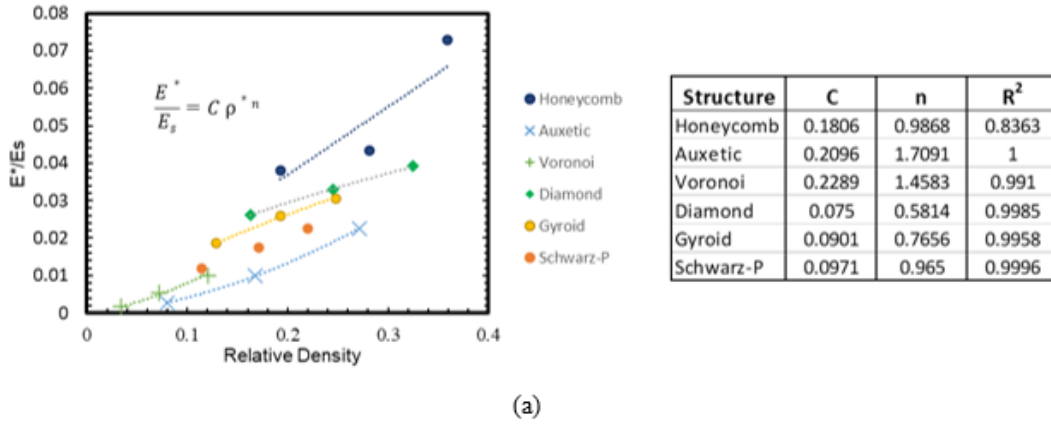


Figure 30. (a) Normalized effective modulus, (b) normalized maximum transmitted stress, and (c) SEA, all plotted as a function of relative density. The adjacent tables provide the fit parameters, with the R<sup>2</sup> value indicative of the quality of the fit.

and the relative density associated with a particular shape. For SEA, however, the honeycomb shows very poor fit quality, which is likely attributable to the lateral spread at the low relative density honeycomb which inflated its SEA value. The diamond and the Schwarz-P have a lower quality of fit compared to the lattices and the gyroid, the latter performing the best overall for tunability across all three metrics.

### 2.5.5 Evaluating Overall Energy Absorption Performance

The above discussion is indicative of the fact that there is more than one metric when it comes to assessing the performance of a particular shape for its potential use as an energy absorber. A formal comparison will depend on specific design requirements and weighting priorities associated with each. The method in Table 3, is one approach that may be taken to compare performance and identify leading candidates for further improvement along specific performance vectors.

Table 3. Comparison matrix for all shapes studied in this work.

Structure	SEA vs Max Transmitted Stress	Densification Efficiency	Plateau Undulation	Tunability	Overall
Honeycomb	2	1	1	2	2
Auxetic lattice	3	3	3	1	3
Voronoi lattice	3	2	1	1	3
Diamond TPMS	1	1	1	2	1
Gyroid TPMS	1	1	1	1	1
Schwarz-P TPMS	1	1	2	2	2

The table suggests that of all six shapes studied in this work, the gyroid and the diamond TPMS shapes stood out as the best performers, followed by Schwarz-P and the

honeycomb. The auxetic and Voronoi lattice shapes demonstrated the worst performance in at least one of the four criteria considered and are thus not recommended for further study for this application.

## REFERENCES

- [8] L. Zhang *et al.*, “Energy absorption characteristics of metallic triply periodic minimal surface sheet structures under compressive loading,” *Addit. Manuf.*, vol. 23, no. July, pp. 505–515, 2018.
- [20] M. F. Ashby, A. G. Evans, N. A. Fleck, L. J. Gibson, J. W. Hutchinson, and H. N. G. Wadley, *Metal Foams: A Design Guide*. Butterworth Heinemann, 2010.
- [37] E. W. Andrews, G. Gioux, P. Onck, and L. J. Gibson, “Size effects in ductile cellular solids. Part II: Experimental results,” *Int. J. Mech. Sci.*, vol. 43, no. 3, pp. 701–713, 2001.
- [38] C. Tekoğlu, L. J. Gibson, T. Pardoen, and P. R. Onck, “Size effects in foams: Experiments and modeling,” *Prog. Mater. Sci.*, vol. 56, no. 2, pp. 109–138, 2011.
- [40] NTopology, “Platform.” New York, 2020.
- [41] ASTM F3302, “Standard for Additive Manufacturing – Finished Part Properties – Standard Specification for Titanium Alloys via Powder Bed Fusion,” *ASTM Stand.*, vol. i, no. February, pp. 1–8, 2018.
- [42] “AMS2774E - IN718 Heat Treatment (SAE Standard).”
- [43] T. A. Schaedler *et al.*, “Designing metallic microlattices for energy absorber applications,” *Adv. Eng. Mater.*, 2014.
- [44] L. Casanova *et al.*, “On the Mechanical Behavior of Additively Manufactured Asymmetric Honeycombs,” in *Solid Freeform Fabrication*, 2018.

### CHAPTER 3: ENERGY ABSORPTION METRICS

A key application for cellular structures is for irreversible energy absorption due to the fact that they essentially are solid structures that embody void, or negative space, and thereby promote large deformation at low stresses by dissipating energy primarily through inelastic dissipation during the compression and removal of these negative spaces.

Unlike single parameter metrics like stiffness or failure strength, the energy absorption behavior of architected cellular materials needs to be characterized with two or more metrics, depending on functional requirements. For example, the designer of a helmet is concerned not merely with the energy absorbed during an impact but also with its density per unit mass and volume (so as to make for a lightweight, compact helmet) and, crucially, the peak force transmitted during the impact [45]. This makes it challenging to draw comparisons across the wide range of design possibilities reported in the literature, amplified as they have been with the advent of AM. However, there is another, less apparent reason why comparisons across AM cellular materials for energy absorption is challenging to do, and that has to do with a central notion in energy absorption: densification. A cellular material under compression would be said to have densified in a physical sense if there is no negative space left to eliminate. In principle, this would imply that it reaches densification when it has deformed so much that all that remains is a fully dense solid volume that equals the relative density of the undeformed cellular material. However, cellular materials start to experience a monotonic increase in transmitted stress well before they are entirely, physically dense. The point where this increase begins is



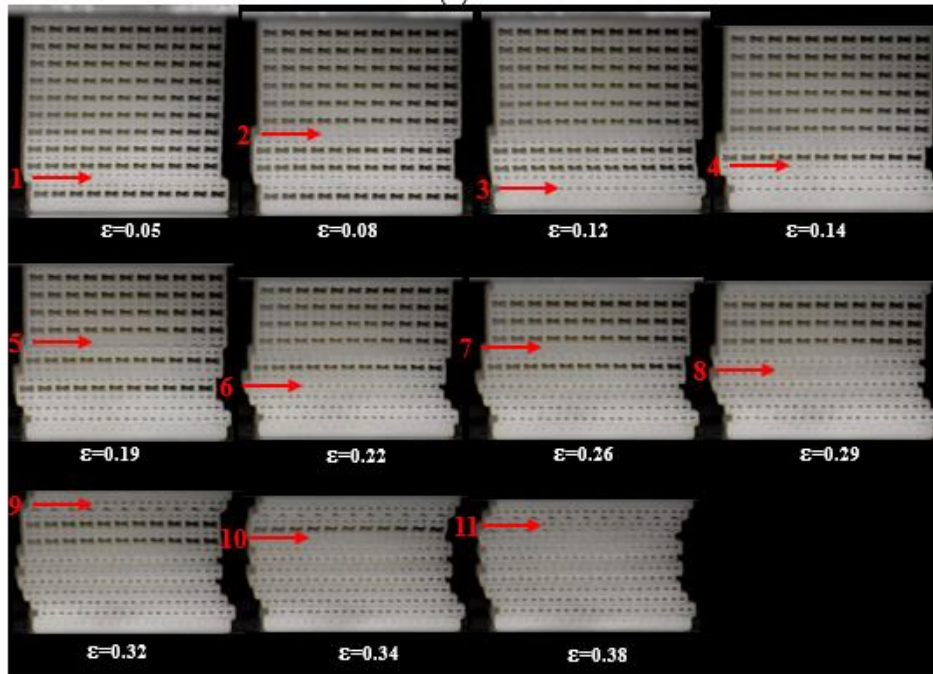
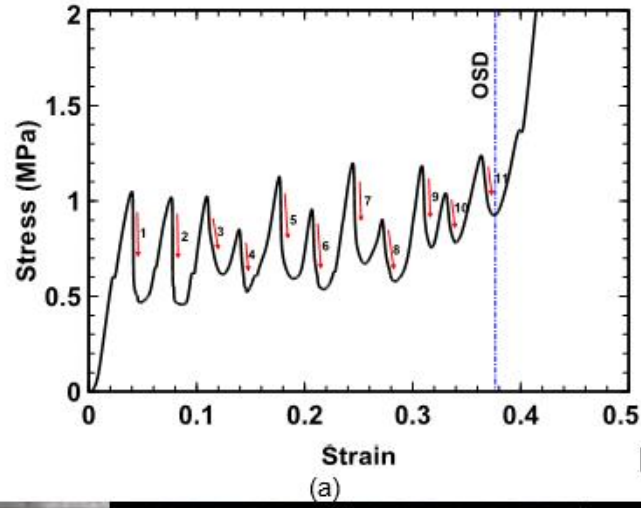
defined in terms of the applied strain at that point and is commonly referred to as densification strain, but is more correctly termed as the onset strain of densification [13]. Beyond this point, the cellular material continues to absorb energy, but does so at detriment to the objective of keeping transmitted stresses below acceptable values. As a result, densification strain is a critical threshold beyond which a cellular material ceases to function as a practical energy absorber. The challenge with densification strain is that there is no single, agreed upon approach to its definition and calculation.

### 3.1. The Role of Densification Strain in Energy Absorption

At the outset, it is useful to reiterate a distinction first made by Li et al. [13] between densification strain and the Onset Strain of Densification, hereafter referred to as OSD, which are two different points on the stress-strain curve of a cellular structure. They correspond to the different levels of interaction between the cell walls of the structure [13]. At densification strain, the cellular structure becomes compact; there are no gaps in the adjacent cell walls and the effective modulus is similar to that of the base material. In comparison, the OSD is a point that indicates the beginning of the densification regime. At this point, for most cellular materials, there are still voids present in between cell walls. The modulus of the structure is increasing, but not on the order of the base material. OSD this represents the point that indicates the end of the plateau region and initiation of interaction between cell walls.

Figure 31 (a) shows the stress-strain response for a Nylon-12 auxetic lattice under quasi-static compression, with each dip in the stress plateau numbered and the corresponding collapse observed physically indicated in Figure 30 (b). The plateau region

is characterized by consecutive cell row collapses, which bring cell walls together, but the load required to further compress these walls against each other is higher than the load required to collapse another row of cells.



(b)

Figure 31. (a) Stress-strain response corresponding to an auxetic lattice structure under compression, (b) Progressive collapse of the auxetic structure, arrows indicate the collapsed row and correspond to the observed dip in plateau stress

In energy absorbing structures, maximum energy is absorbed in the plateau region. As a result, determination of the extent of the plateau region is extremely important to determine

the amount of energy the structure can absorb – and this in turn depends on OSD since it is the parameter that defines the end of the plateau region. Further, due to its relevance in computing the usable energy absorption, OSD, and not densification strain, is a more appropriate metric for practical analysis.

### 3.2. Approaches for Estimating the Onset Strain of Densification (OSD)

A survey of the literature studying energy absorption in additively manufactured cellular materials shows that four approaches have been used for the estimation of OSD. A selection of these papers is summarized in Table 3, which shows that across a wide range of cellular structures, processes, and materials, the OSD is defined using different methods in some cases, the authors do not explicitly specify which method they use.

Table 3. Densification strain methods used in the literature studying energy absorption characteristics of additively manufactured cellular structures.

Sr. No	Authors	Structures	Material / Process	Onset Strain of Densification		
				Maximum Efficiency Method	Fixed Strain Method (strain value)	Plateau Stress Method (Stress multiplier)
1	Zhang, 2018 [16]	TPMS	SS 316L	•		
2	Habib, 2018 [46]	Lattice	PA-12	•		
3	Tao, 2019 [47]	Honeycomb	VW Plus	•		
4	Plocher, 2020 [48]	BCC Schwarz-P	Onyx	•		
5	Li, 2021 [49]	TPMS-Gyroid	SS 316L	•		
6	Zhao, 2022 [50]	Sheet based lattice	Ti6Al4V	•		
7	Ozdemir, 2016 [51]	Lattice	Ti6Al4V		• (0.3)	
8	Novak, 2021 [52]	TPMS	SS 316L		• (0.4)	
9	Liang, 2021 [53]	TPMS	SS 316L		• (0.4)	

10	Ali, 2020[54]	TPMS	PA1102	• (0.4)	
11	Maskery, 2017[55]	Gyroid	AlSi10Mg	• (0.5)	
12	Kumar, 2019[56]	Honeycomb	VW Plus	• (0.5)	
13	Al-Ketan, 2021[57]	TPMS	SS 316L	• (0.5)	
14	Ravichander, 2022 [58]	TPMS	SS 316L	• (0.5)	
15	Wang, 2021 [59]	TPMS	Ti6Al4V	• (0.5)	
16	Bai, 2020 [60]	FG lattice	PA 2200	• (0.55)	
17	Wang, 2020[61]	Cylindrical TPMS	SS 304	• (0.6)	
18	Abueidda, 2019 [62]	TPMS	PA 2200	• (0.6)	
19	Cao, 2020 [63]	novel P-lattice	Numerical Study	• (0.6)	
20	Zhong, 2021 [64]	Schwarz-Primitive	SS 316L	• (0.65)	
21	Xu, 2021[65]	TPMS-Gyroid	SS 316L		•
22	Ma, 2020 [15]	strut TPMS	Cu-Cr-Z		•
23	Zhang, 2022 [66]	TPMS	SS 316L		•
24	Fan, 2021 [67]	TPMS	Ti6Al4V		•
25	Liu, 2021[68]	BCC FCC	Al-12Si		•
26	Sun, 2022[69]	TPMS	Ti6Al4V		•
27	Li, 2019 [70]	Sheet & Strut gyroid	SLA		•
28	Maskerey, 2018 [31]	TPMS	PA 2200	-	
29	Cui, 201 [71]	Foams	Vero White Plus	-	
30	Jefferson, 2021[72]	Plate Lattices	SLA (PlastGRAY)	-	
31	Fu, 2022[73]	TPMS sheet	PA 2200	-	
32	Sankineni, 2021[74]	TPMS	PLA	-	

Four methods have been used in the literature, though one of them does not seem to have found application in the AM community. Prior to discussing each of these in turn, it is useful to underline the significance of this lack of standardization in the estimation of OSD. Each of the four methods can result in different OSD values, as shown in Figure 32 which is a stress-strain curve derived from a Schwarz primitive structure from this study, to be discussed more in a later section. While cellular materials with flatter plateaus are likely to have more agreement across the four methods, the behavior seen in Figure 32 is

not uncommon in several additively manufactured cellular materials reported in the literature and is hence used here as an example. The following sub-sections discuss each of these four methods in more detail.

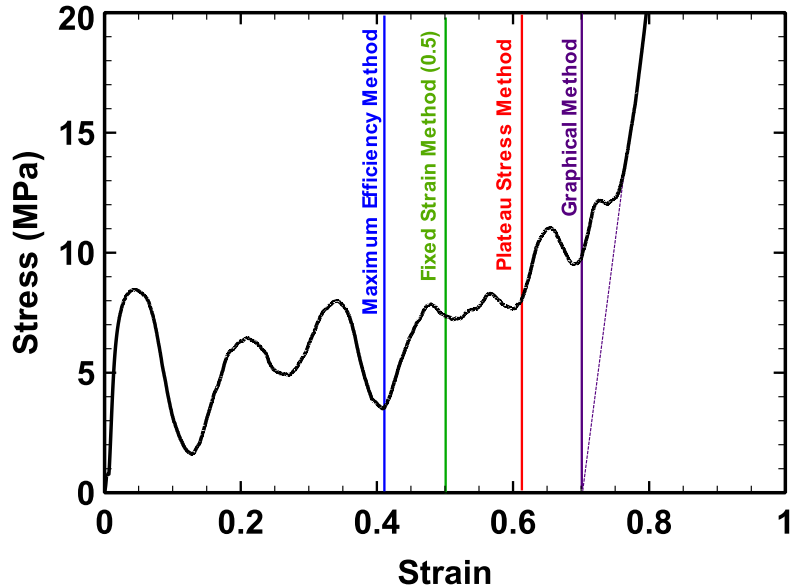


Figure 32. Onset strain of densification estimated using various approaches for the Schwarz Primitive structure.

### 3.2.1 Graphical Method

The graphical method is illustrated by the purple line in Figure 32. In this method, the slope of the densification region (also known as the densification modulus) [75] is used to determine the OSD. A line is drawn with the slope equal to the densification modulus shown by a dotted purple line in Figure 32. According to this method, the point at which the extended line intersects the x-axis is the densification strain [20]. A challenge with this approach is its sensitivity to the experimentally derived slope, which tends to gradually increase from the end of the plateau (Appendix Figure S1.6, S1.8). If the structure is not

tested till true densification modulus is obtained, that can result in lower OSD. Further, some structures show hardening behavior in the plateau where a transition from the plateau to the densification slope is less apparent (Appendix Figure S1.10, S1.11). Results obtained using this method are challenging to automate and rely on subjective verification by the user.

### 3.2.2 Fixed strain Method

As the name suggests, in this method, a fixed strain value, 0.4, 0.5 or 0.6 is fixed as the end of the plateau region. The green line in Figure 32 indicates the densification point at 50% strain according to the fixed strain method. This strain is fixed based on either design requirements or derived from visual inspection of the stress-strain curve. This is a practical approach, often motivated by the desire to avoid the uncertainties imposed by the other methods, and by the ease of implementation from a design perspective. However, this approach can be misleading if we try to compare various shapes based on the results of this method. Additionally, the plateau end strain fixed in this method is not the actual OSD, which as will be shown in section 3.2.3, can range from 30% to 80%. Having a higher onset strain of densification can be advantageous in specific applications and the fixed strain method runs the risk of overly conservative design in instances where the true densification is higher than that defined by the fixed strain method. This method also ignores stress information and the shape of the stress-strain curve, which can result in over-estimation of energy absorption for energy absorbing cellular materials with hardening behavior or with early OSD (Appendix Figure S1.3, S1.12).

### 3.2.3 Plateau Stress based Method.

This method is recommended by the ISO 13314:2011 standard [76] for compression tests for porous and cellular metals [76]. In this method, OSD is defined in the context of the end of the plateau region. The arithmetic means of stresses in the range of 20%-30% or 20%-40% strain, depending on the nature of the stress-strain curve, is considered as the plateau stress. A point in the stress-strain curve at which stress is 1.3 times that of the plateau stress is considered plateau end strain. The multiplier 1.3 can be changed if this point does not adequately represent the end of the plateau range. This standard gives a good guideline, but the plateau end strain must be determined by the user and a single multiplier is unlikely to be valid for all the shapes. For some shapes, as will be shown, densification happens as early as 30% of strain. This method is thus based on user expertise to identify the end of the plateau region and select an appropriate multiplier and as such is difficult to robustly codify and automate for a diversity of energy absorption behaviors.

### 3.2.4 Maximum Efficiency Method

Among the methods to determine the OSD, the maximum efficiency method [13] is a widely used approach and aims to mitigate some of the limitations described for the previous approaches. As the name suggests, it relies on the estimation of the efficiency of energy absorption.



If a cellular structure is compressed, the energy absorbed per unit volume is the area under the stress-strain curve, and can be estimated as:

$$W = \int_0^{\varepsilon_a} \sigma(\varepsilon) d\varepsilon \quad (8)$$

Where  $\varepsilon_a$  is the nominal strain up to which the energy absorption is estimated. The energy absorption efficiency parameter is defined as the energy absorbed per unit volume up to  $\varepsilon_a$ , divided by the corresponding stress value.

$$\eta(\varepsilon) = \frac{1}{\sigma(\varepsilon)} \int_0^{\varepsilon_a} \sigma(\varepsilon) d\varepsilon \quad (9)$$

Tan et al. [77] proposed for open cell foams that densification strain can be obtained at a strain where this efficiency has a global maximum:

$$\left. \frac{d\eta(\varepsilon)}{d\varepsilon} \right|_{\varepsilon_a} = 0 \quad (10)$$

Li et al. [13] proposed a method to determine the onset strain of densification based on the maximum efficiency so derived. This method first requires that the stress-strain curves be categorized based on the nature of the plateau stress. The onset strain of densification is either the global maximum of the efficiency strain curve or the last maximum if the plateau behavior is plastic. However, as will be shown in the next section, for some additively manufactured cellular structures, the OSD is neither the global maximum nor the last maximum on the efficiency curve, hence a new method is proposed to identify the point accurately.

### 3.3. Objectives and Structure of this Paper

This work has two objectives: (i) recommend a new approach for the computation of OSD, which modifies the maximum efficiency method; and (ii) compare the various

methods, including the one proposed here, against each other, using an identical dataset obtained from an experimental study conducted with two different materials and six different cellular topologies, and the effect of enclosing them in a tube.

Section 2 introduces the proposed approach for estimating the OSD, with an example. The experimental study, including design and manufacturing methods, is described in section 3.2.3. The results of uniaxial compression of the cellular structures are presented in section 3.4. The results are analyzed and compared with different methods in section 3.5, towards drawing conclusions and recommendations in the final section.

#### 3.4. The Hybrid Efficiency Method for Estimating the OSD

The first objective of this work is to propose a new, Hybrid Efficiency Method (HEM) for the estimation of the onset strain of densification. This method builds on the Maximum Efficiency Method (MEM) discussed previously. In equation , the efficiency parameter has the term  $\sigma(\varepsilon)$ , which is the effective stress corresponding to the strain at which the efficiency is calculated. The term in the numerator is a monotonically increasing function of strain, with absorbed energy incrementally added with increasing strain.

The use of the instantaneous stress in the computation of the efficiency parameter has a key drawback, which can be demonstrated by revisiting the stress-strain behavior of the auxetic specimen shown previously in Figure 31. Figure 33 (a) shows the efficiency estimated using instantaneous stress as shown in equation 9, overlaid on top of the stress-strain response. The use of the instantaneous stress results in significant variation in the efficiency parameter – greatly increasing the sensitivity of the definition of OSD to the

identification of a local peak, as shown in Figure 33 (a), since the MEM relies on the identification of OSD at the point of maximum efficiency.

If on the other hand, the instantaneous stress  $\sigma(\varepsilon)$  in the formula is replaced by the peak stress up to that instant,  $\sigma_p(\varepsilon)$  we can compute efficiency, as:

$$\eta_p(\varepsilon) = \frac{1}{\sigma_p(\varepsilon)} \int_0^{\varepsilon} \sigma(\varepsilon) d\varepsilon \quad (11)$$

Efficiency computed using the peak stress in this manner generates a far smoother curve as shown in Figure 33 (a), with a maximum value that is less sensitive to perturbations in the underlying stress-strain response. According to the MEM, the OSD lies at the global maximum of the efficiency curve, in this case, at an effective strain of 0.29. However, it is evident from the graph that the stress value remains in the same range till strain reaches around 0.4, and then it increases monotonically.

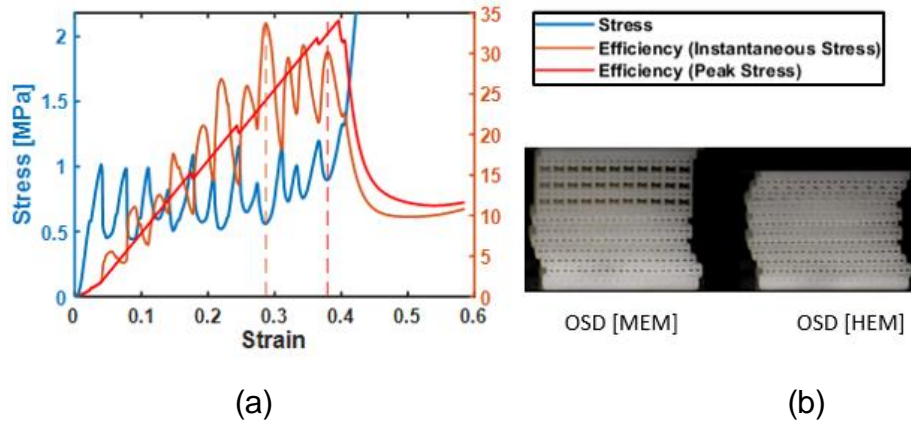


Figure 33. (a) Comparison of efficiency as estimated using the instantaneous and peak stress approaches; (b) specimen at the maximum efficiency estimated using both approaches.

According to the proposed HEM, the onset strain of densification is found to be 0.38. This point corresponds with the last maxima on the efficiency (instantaneous stress) curve prior to the global maxima on efficiency (peak stress). The maxima on the efficiency

(instantaneous stress) indicate local minima in the stress corresponding to collapse in the structure. The global maximum in the efficiency (peak stress) signifies strain value after which energy absorption is not efficient. Thus, HEM selects a point on the stress-strain curve which corresponds to the last collapse in the structure till the energy absorption is efficient. Figure 32 (b) shows the structure at the strain marked as OSD by maximum efficiency method and hybrid efficiency method respectively.

The efficiency derived using the HEM can be interpreted as the ratio of energy absorbed and maximum stress experienced by the structure till that point. The global maximum on this curve indicates the maximum energy that is absorbed for the highest transmitted stress through the structure, which is a key design requirement. After this point the structure can absorb more energy, but the transmitted stress will be higher, and the energy absorption is as a result, inefficient. Figure 33 (a) and (b) clearly indicate that the HEM results in a more accurate estimation of OSD than the MEM, but this is limited to the Nylon-12 auxetic lattice. The rest of this paper puts these two approaches to the test for a wider range of cellular topologies and materials.

### 3.5. Methods

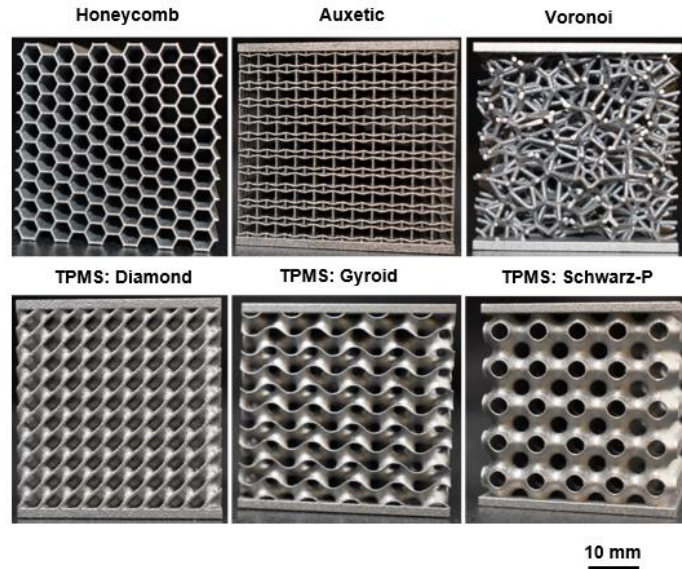
#### 3.5.1 Design

To enable a valid comparison of the different approaches to estimating OSD discussed here, cellular structures spanning six different designs were selected, following work reported in the previous chapter where all these designs were fabricated in AlSi10Mg

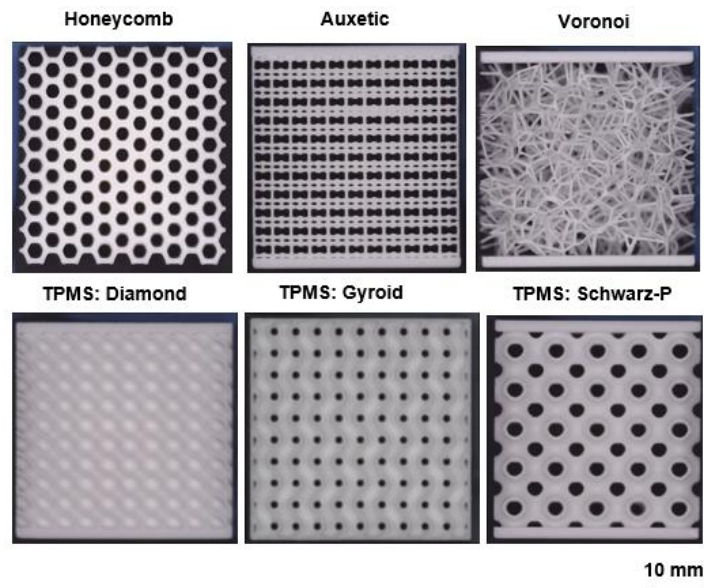
using Laser Powder Bed Fusion. On completion of that study, Nylon-12 specimens, with the identical design, were fabricated using Selective Laser Sintering.

### 3.5.2 Manufacturing

The AlSi10Mg specimens were manufactured on a Concept Laser MLab Cusing R machine (GE additive, Cincinnati, OH, USA) equipped with a single 100 W ytterbium fiber laser source. The Nylon-12 specimens used in this study were manufactured on an EOS FORMIGA P110 (EOS, Krailling, Germany) selective laser sintering machine with a 30W laser and optimized and proprietary laser parameters provided by the manufacturer. PA2200 powder (manufactured by EOS) with an average particle size of 56  $\mu\text{m}$  was used for manufacturing the specimens. All the parts were manufactured in a single build. The parts were oriented with end plates perpendicular to the printing direction, and for the honeycombs the cell walls were along the printing direction. The printed AlSi10Mg and Nylon-12 specimens are shown in Figure 34 (a) and (b), respectively. All specimens underwent quasistatic compression under an Instron 250 kN load-frame, details of which are also available in [78].



(a)



(b)

Figure 34. Manufactured specimens (a) AlSi10Mg specimens printed on ConceptLaser Mlab machine with Laser Powder bed Fusion (reproduced from [42]) (b) Nylon-12 Specimens printed on EOS machine using Selective Laser Sintering

### 3.6. MATLAB Implementation

A MATLAB code was developed to estimate the onset strain of densification and evaluate all the energy absorption characteristics and is provided in the Appendix A material. Force and data output from the compression test in the form of csv file is provided as input for the MATLAB code. All measured parameters for the given specimen, such as length, width, height, and mass are provided as a separate .csv file. Effective stress and effective strain for the cellular structure are calculated using given input data with equations,

$$\sigma^* = \frac{F}{A} \quad (12)$$

$$\varepsilon^* = \frac{\delta}{L} \quad (13)$$

where  $F$  is the compressive force on the structure,  $A$  is the cross-section area of the bounding box of the cellular structure,  $L$  is the height of the cellular structure, and  $\delta$  is the displacement of the compression platen. The area under the stress-strain curve (Energy absorbed per unit volume) is calculated using the trapezoidal method of numerical integration. Energy absorbed after each increment is stored and used in the calculation of the efficiency parameter using the two different stress assumptions in equations 9 and 11. The signal processing toolbox is used for filtering data and removing local undulations in the efficiency data.

### 3.7. Results

The results are presented in this section in two parts: the first subsection reports findings from the comparison of compression response plots of identical cellular structures with AlSi10Mg and Nylon-12, and the second subsection presents OSD as estimated from the two efficiency-based approaches.

#### 3.7.1 Compression Response

To enable comparisons of response between geometrically identical cellular structures and specimens of different material compositions, effective stress was normalized by yield strength of the respective material. The yield strength of Nylon-12 is obtained by uniaxial tensile test as per ASTM D638-14 standard [79], and yield strength of AlSi10Mg is provided by parts manufacturer. The normalized effective stress vs. effective strain response for all the structures studied is plotted in Figure 35, with colors indicating material



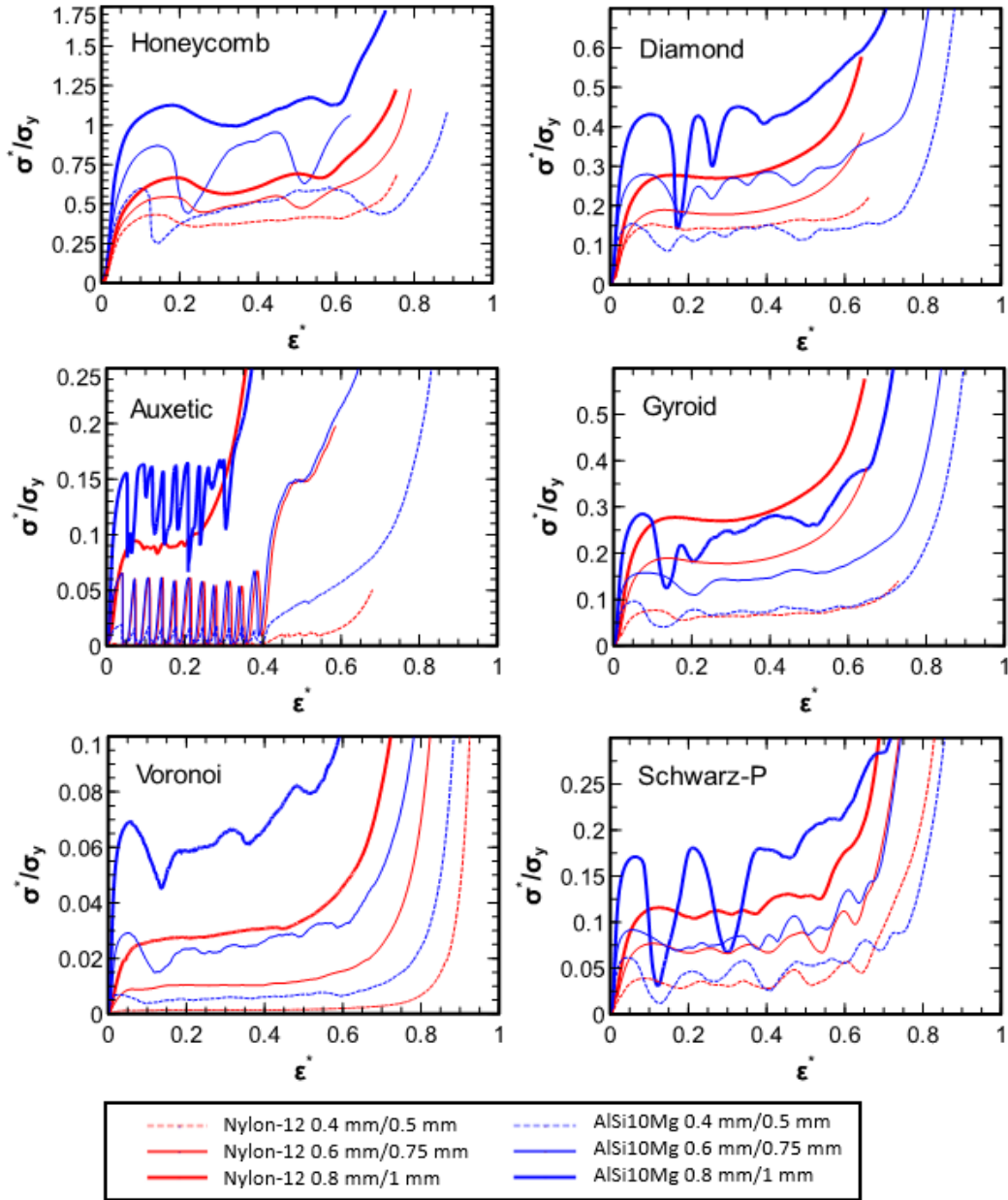


Figure 35. Stress-strain curves of cellular structure under uniaxial compression for Nylon-12 and AlSi10Mg structures, normalized by the yield strength of the material.

composition and the line thickness representing thickness of walls (0.4 - 0.8 mm) in shell-based structures, and of beams (0.5 - 1 mm) in lattice structures. The stress-strain curves of structures enclosed in tubes are provided in Appendix B. All curves show three

distinct regions as discussed previously, but the shape of the curve differs as a function of cell topology, relative density, and the base material. Among the beam-based lattice structures, the auxetic lattice had high variation in the stress level as discussed previously, whereas a smoother plateau was obtained for the Voronoi lattice. TPMS structures made up of Nylon-12 show behavior similar to ideal energy absorber. Identical structures made up of AlSi10Mg show big drop in the stress level due to formation of shear band. These structures have unique energy absorption characteristics and can be used in different applications. However, to compare these structures' energy absorption characteristics, estimating the correct onset strain of densification is very important. Based on OSD determined by hybrid efficiency method, the SEA, maximum transmitted stress, undulation coefficient, Plateau stress are computed for all the structures. The comparison of these characteristics based on material and relative density is out of scope of this paper hence the variability charts for all the energy absorption characteristics for the structures are given in Appendix D.

### 3.8. Onset Strain of Densification ( $\epsilon_d$ )

Table 4 gives values of the OSD calculated by the Maximum Efficiency Method (MEM) and the proposed Hybrid Efficiency Method (HEM).

Table 4. Onset strain of densification estimated with the two different efficiency-based methods.

Structure Name	Relative Density	AlSi10Mg		Nylon-12	
		Densification Strain HEM	Densification Strain MEM	Densification Strain DEM	Densification Strain MEM
Schwarz	0.11	0.61	0.41	0.64	0.52
Schwarz	0.17	0.56	0.56	0.54	0.54
Schwarz	0.23	0.43	0.27	0.54	0.54
Schwarz with tube	0.13	0.67	0.61	0.56	0.56
Diamond	0.16	0.69	0.69	0.59	0.59
Diamond	0.25	0.71	0.71	0.53	0.53
Diamond	0.33	0.66	0.66	0.55	0.55
Diamond with tube	0.18	0.67	0.66	0.58	0.58
Gyroid	0.13	0.62	0.60	0.62	0.62
Gyroid	0.19	0.59	0.59	0.62	0.62
Gyroid	0.26	0.57	0.57	0.52	0.52
Gyroid with tube	0.15	0.76	0.76	0.64	0.58
Auxetic	0.09	0.40	0.40	0.41	0.17
Auxetic	0.18	0.39	0.18	0.38	0.29
Auxetic	0.30	0.31	0.31	0.25	0.25
Auxetic with tube	0.10	0.75	0.47	0.56	0.48
Voronoi	0.03	0.63	0.60	0.56	0.55
Voronoi	0.07	0.62	0.62	0.53	0.53
Voronoi	0.12	0.54	0.53	0.53	0.53
Voronoi with tube	0.05	0.81	0.76	0.71	0.63
Honeycomb	0.20	0.57	0.50	0.62	0.62
Honeycomb	0.30	0.52	0.52	0.52	0.52
Honeycomb	0.39	0.46	0.46	0.58	0.58
Honeycomb with tube	0.22	0.75	0.71	0.60	0.60

The values are also plotted against each other in Figure 36. The solid black line indicates equal values for both methods. The farther away the point from the line horizontally, the more significant the difference between  $\epsilon_d$  estimated by these two methods – approximately half of the structures tested have OSD values that do not lie on the line. The maximum difference in OSD estimated by the two methods are 58.53%, whereas the average difference is 18%.

The spread of OSD is from 0.2 to as high as 0.8. For the fixed strain method, which assumes an OSD typically of 0.4 or 0.5, the computed energy is in most cases either higher or lower than the actual capacity of the structure.

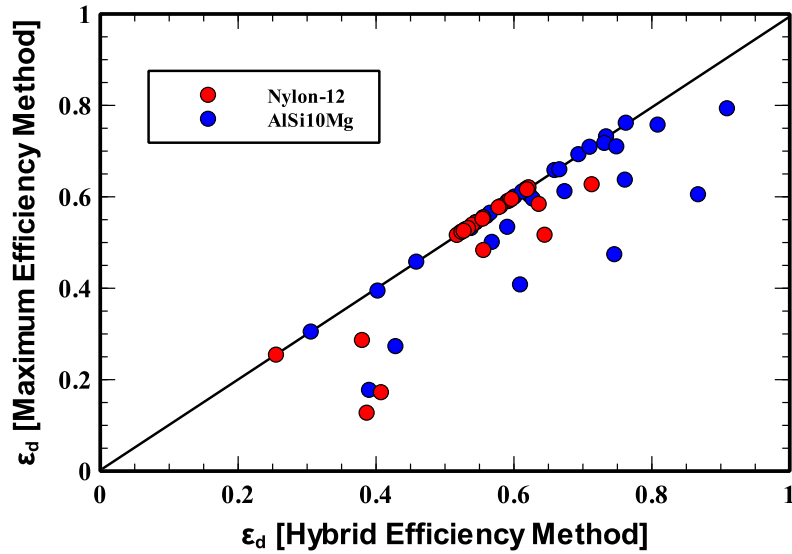


Figure 36. Onset strain of densification points determined by maximum efficiency method and Hybrid efficiency method for studied structures.

Figure 37 shows a variability chart for OSD as determined by HEM for studied shapes. All the shapes grouped according to material and wall thickness/ beam diameter on the X-axis. For the structures except Nylon-12 honeycomb and AlSi10Mg Diamond the OSD decreases with increasing relative density. The average OSD for AlSi10Mg Voronoi and Diamond shapes are higher than Nylon-12.

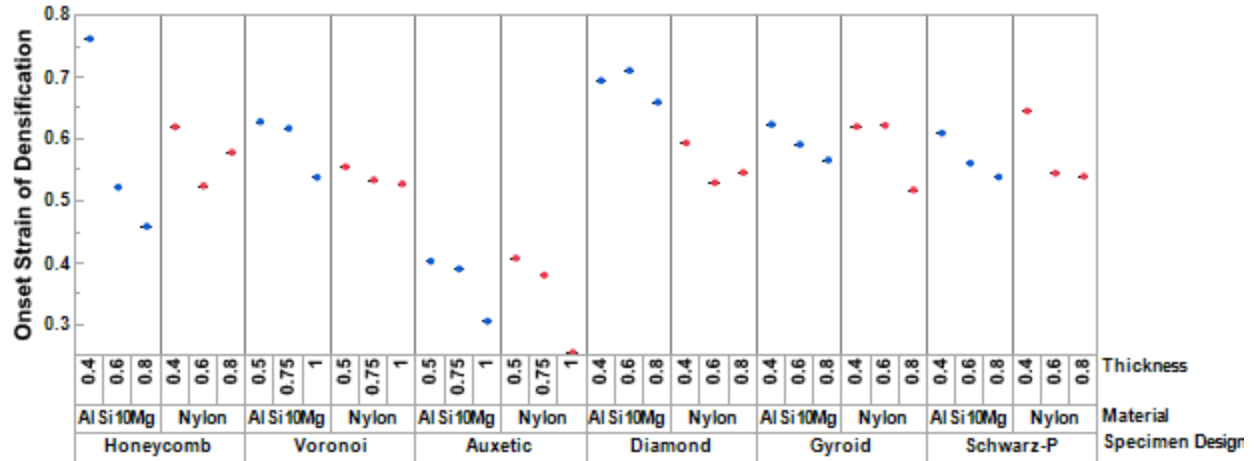


Figure 37. Variability graph showing OSD estimated with the proposed method for all the cellular structures in this work.

### 3.9. Discussion

Among the metrics used to characterize an energy-absorbing structure, two essential and widely used metrics are Specific Energy Absorption (SEA) and Maximum Transmitted Stress (MTS) through the structure [19]. The selection of a particular cellular structure for an energy absorption application is driven by the objective of maximizing SEA against the MTS allowed for the application in question.

#### 3.9.1 Specific Energy Absorption (SEA)

The definition of OSD affects both SEA and MTS to a significant degree, as shown in Figure 38 and Figure 39, respectively, where three methods discussed previously (HEM, MEM and fixed strain) are compared pairwise. Figure 38 (a) compares SEA calculated with the HEM and MEM, where deviations are clearly observed for the AlSi10Mg specimens, with the MEM always underestimating SEA. Figure 38 (b) compares HEM to the fixed strain method, the latter assuming an OSD value of 0.5, and shows that the fixed

strain method can both over- and under-estimate the SEA, though this depends on the value of the threshold OSD. In general, for AlSi10Mg specimens, the deviations between the OSD determined by MEM and HEM are greater, which is a result of greater undulations observed in the AlSi10Mg specimens (Appendix B), in turn caused by the higher propensity for fracture in these specimens [78], which makes it more sensitive to local maxima in the efficiency curve. In the Nylon-12 specimens however the Efficiency (instantaneous stress) and Efficiency (Peak stress) curves are same due to monotonous increase in the stress level (Appendix B Figure S1.29-S1.32, S1.34-1.35). The sudden drop in the stress level caused by material failure is not present. For the Schwarz structures undulations are observed in the Nylon-12 material but the drop in stress level is not as high as observed in AlSi10Mg structures.

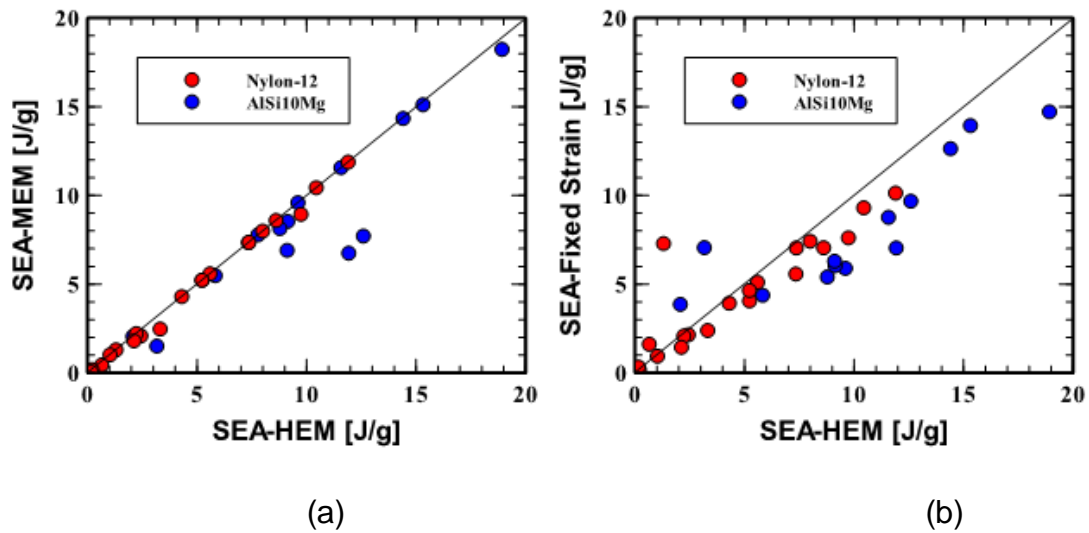


Figure 38. Comparison of Specific Energy Absorption estimated by different methods (a) Comparison of MEM and HEM approaches, and (b) comparison of fixed strain (0.5) and HEM approaches.

### 3.9.2 Maximum Transmitted Stress (MTS)

A similar comparison of estimated MTS values is shown in Figure 39 (a) and (b). MTS is not as sensitive to OSD definition as SEA is. The reason for this is apparent from Figure Figure 33 - MTS is often the first peak stress and is as a result not as sensitive to OSD which occurs at higher strain values than that corresponding to the first peak stress. Figures Figure 38 (a) and Figure 39 (a) are indicative again of how the MEM can lead to conservative designs by not maximizing the available SEA for a given MTS.

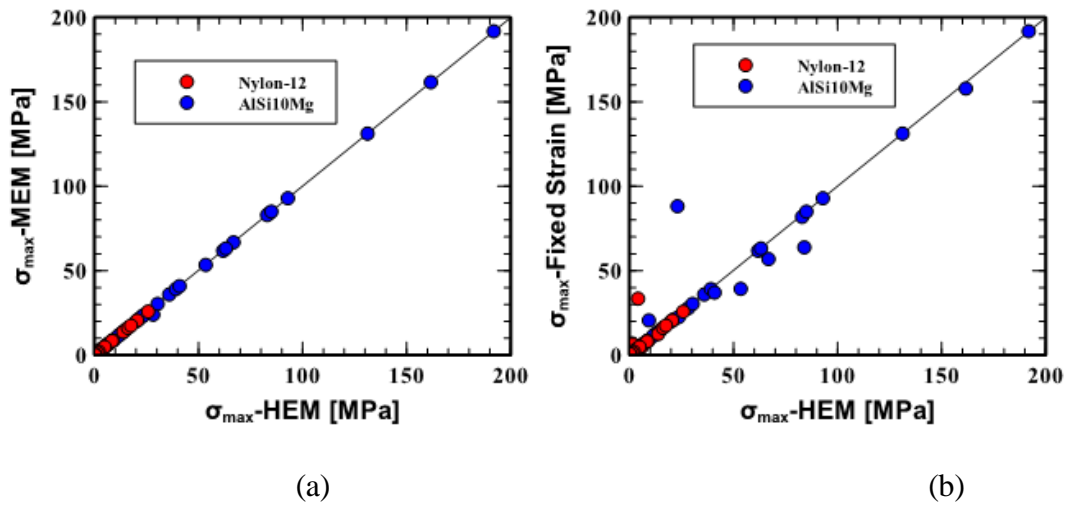


Figure 39. Comparison of maximum transmitted stress estimated by different methods (a) Comparison of MEM and HEM approaches, and (b) comparison of fixed strain (0.5) and HEM approaches.

### 3.10. Conclusions

The following conclusions may be drawn from the work reported in this chapter:

- A review of the literature of quasistatic energy absorption of additively manufactured cellular materials shows that wide range of unit cells and materials

are explored and characterized for energy absorption. It is observed that there is inconsistency in methods to determine onset strain of densification.

- At least four different approaches can be used for the calculation of OSD: Graphical method, Maximum efficiency method, Fixed Strain method and Plateau Stress method. These methods have subjectivity associated with them and can lead to erroneous estimation of OSD depending on the stress strain curve of a cellular structure.
- The Maximum Efficiency Method (MEM), while effective with the foams and structures with low ULC shown to give early densification for the structures due to local drop in the stress values.
- A new approach, called the Hybrid Efficiency Method (HEM) was proposed which is similar to MEM with the exception of (i) using peak stress instead of instantaneous stress to identify the efficiency maxima, and (ii) identifying the local maxima on the instantaneous efficiency just prior to this point to establish OSD.
- A comparison of approaches showed that Hybrid efficiency method is shown to improve accuracy in the prediction of OSD for the additively manufactured cellular structures.



## CHAPTER 4: FINITE ELEMENT ANALYSIS OF SHELL STRUCTURES

Chapters 2 and 3 demonstrated the vital role of unit cell topology, relative density, and material composition in influencing energy absorption behavior of cellular structures under quasistatic compression. TPMS structures showed promising behavior with regard to high energy absorption against maximum transmitted stresses, and tunability across a wide relative density range. As a result, subsequent discussion in this thesis focuses on surface/shell based TPMS structures. In this chapter, the Finite element analysis of shell structures is summarized, and the development of the Finite element model for the TPMS structures is shown. This forms the basis for the field-driven design exploration in the following chapter.

A shell structure is any three-dimensional structure which has a low thickness dimension in one direction and has a proportionally wide span in the remaining two directions. Shell structures are found in various natural designs, such as seashells, coconut shells, and the human skull. Due to this spatial design, they can span large areas, are lightweight, and resist applied load effectively. Shell structures also possess superior strength when they leverage curvature [80]. Various analytical models have been developed to analyze shell structures, but Finite Element Analysis (FEA) provides a significant advantage in analyzing complex shell structures of the kind used in the TPMS geometries central to this work. A crucial aspect of applying the method is capturing the shell structure's curvature accurately. It is important to note that the mathematical model, which includes shell geometry, a constitutive model of material, and boundary conditions,

comprehensively describes the physical structure. Figure 40 shows the process flow of the solution of the structural analysis of a shell structure using finite element analysis.

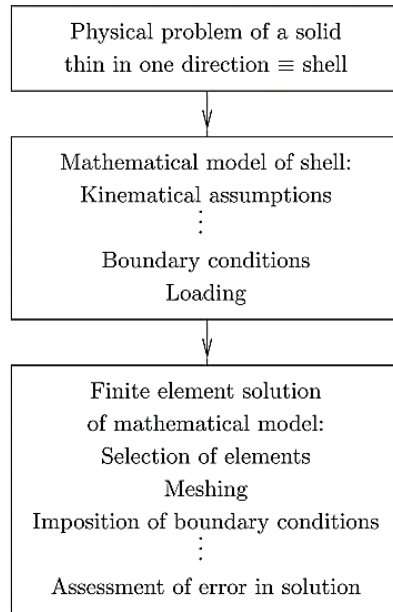


Figure 40 Process of finite element analysis of shell problems [80]

There are multiple methods to model shell-based TPMS structures in FEA - Simsek et al. [81] have provided comprehensive guidelines to model TPMS structures. Figure 41 shows all the possible modeling techniques for the TPMS structures. Table 5 gives an overview of each modeling method. Shell modeling is easy, computationally efficient, and easy for data management, but its applicability is limited as it can only be applied to very thin structures. Solid modeling applies to all shapes, but modeling with hexahedral elements is challenging and computationally inefficient when simulating thin structures. The element size must be kept low and simulation time is higher for solid elements. The data generated during simulation is proportional to the model size: a massive amount of data is generated for the solid model. Homogenization is an efficient technique to simulate

cellular structures, but it is useful till elastic limit only: for energy absorption applications, the large deformation of the topology of the structure plays an essential role and cannot be extracted from low strain behavior alone.

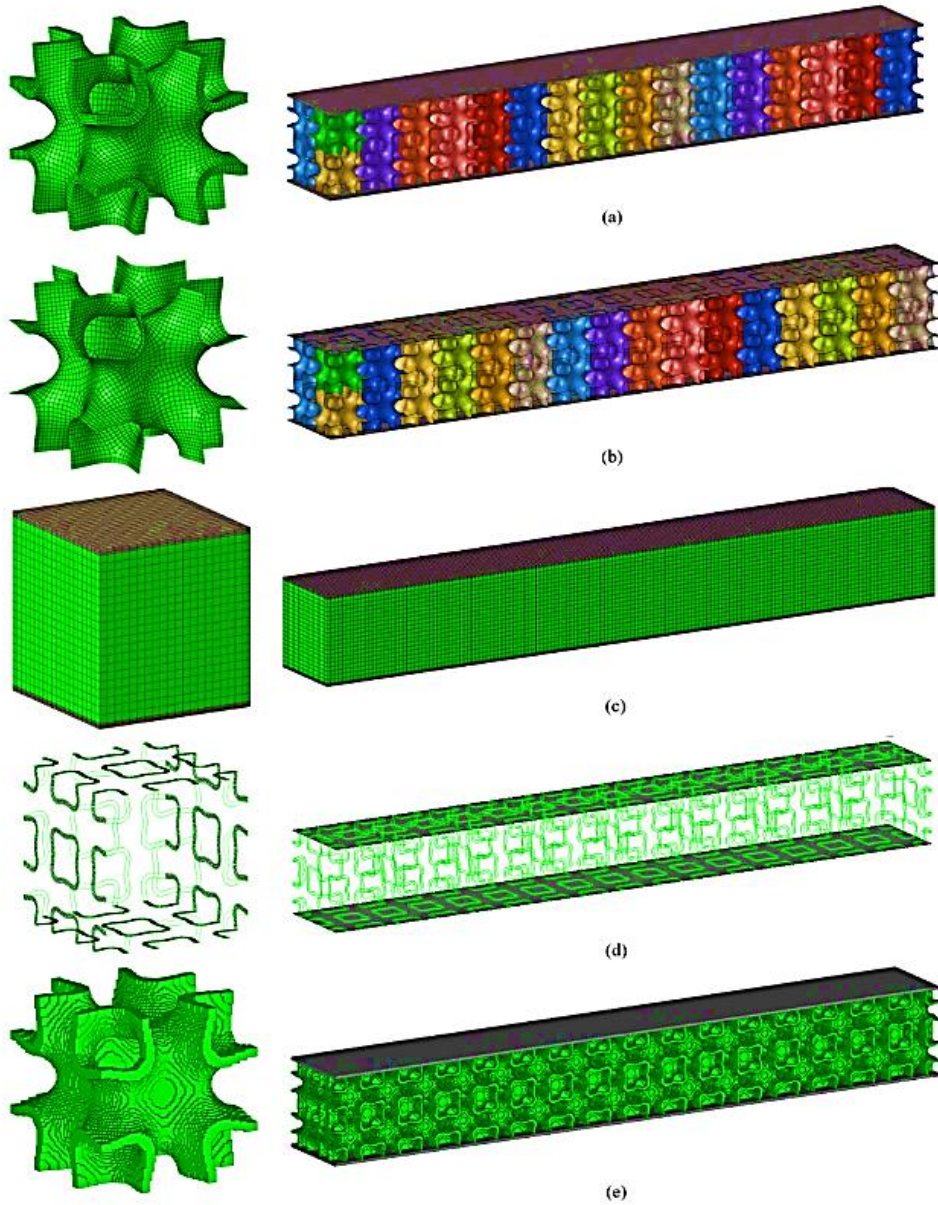


Figure 41 Finite element modeling approaches for a TPMS structure (a) solid, (b) shell, (c) homogenization, (d) super element, and (e) voxel [81]

Table 5 TPMS modeling methods comparison [81]

Modeling strategy	Modeling ease	Computational efficiency	Data management	Applicability
Shell	••••	•••••	•••••	••
Solid	•	•	•	•••••
Homogenization (PBC)	••	••••	••••	••••
Super element	•••	•••	•••	•••••
Voxel	•••••	••	••	•••••

#### 4.1. Modeling CAD structures for FEA

Simsek [81] concluded that shell elements are an efficient way to model TPMS structures. Conventionally, shell structures are modeled using the mid-surface of the structure. A single chart is used to represent 3D structure in the 2D domain, as shown in Figure 41.

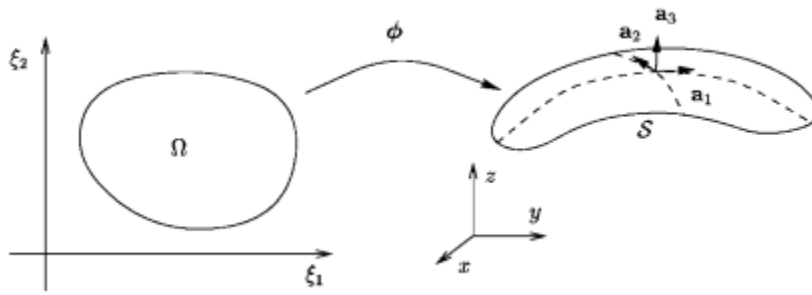


Figure 42. Mapping of a solid to a shell geometry [80]

Building on this approach, for this work, the symmetry of the structure was exploited to generate a finite element mesh of the TPMS structure. The Schwarz-P structure is selected for this study as it is found to have undulations in the stress strain response unlike Diamond and Gyroid structures. The mid surface of the quarter TPMS Schwarz

Primitive structure was extracted and meshed in Hypermesh<sup>®</sup> Software (V13.0). The quarter surface was meshed with four-node shell elements (S4). The nodes on the edges were checked for accuracy. A small node position error can lead to a significant deviation from the actual design due to arraying. The elements in the quarter section were copied and mirrored across the X, Y, and Z axis, respectively. As shown in Figure 42, the complete unit cell was obtained by the abovementioned process, with 3696 nodes and 3661 elements in the unit cell model. For the Schwarz Primitive design shown here, the mirror operation works to populate a cellular structure as the geometry is symmetric across three axes. However, in the case of Gyroid and Diamond, the elements must be rotated after mirroring.

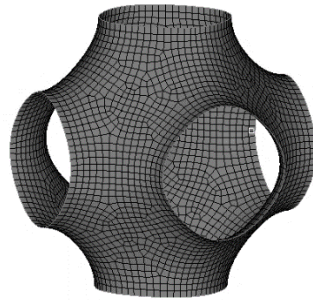


Figure 43 Schwarz Primitive unit cell meshed with S4 elements.

Once the unit cell was modeled, the quality of elements is checked. Table 6 gives the element quality criterion used for this study, consistent with those provided in Abaqus documentation [82] for reliable output with shell elements. The first column shows parameters, the second column shows the worst value in the generated mesh, and the third column indicates the minimum or maximum value. The generated mesh follows all the

criteria for excellent quality mesh. Importantly, node equivalence is essential after arraying all the elements to ensure continuity.

Table 6. Element quality criterion for S4 elements as obtained for a Schwarz-P unit cell.

Parameter	Worst	Criterion
Warpage	3.36	20
Skewness	0	30
Jacobian	0.58	0.5
Min Angle	58.41	45
Max Angle	125.57	135
Aspect Ratio	1.96	10
Min Length	0.135	0.1

The elements were then copied and arrayed to generate a final design, shown in Figure 44, having 125 unit cells. The full mesh consisted of 4,61,980 nodes and 4,57,680 elements.

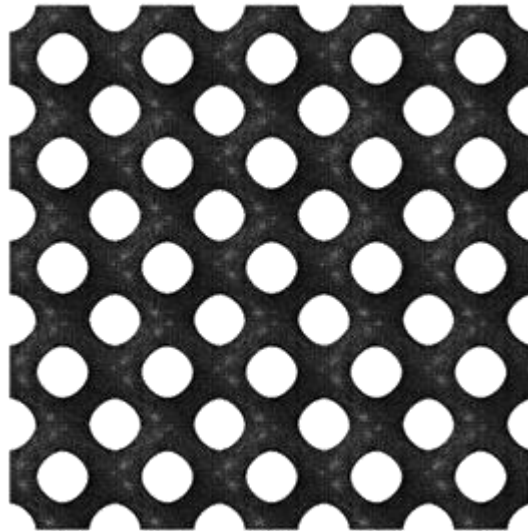


Figure 44 Front view of the full model of Schwarz Primitive structure meshed with S4 elements.

## 4.2. Material Model

The accuracy of FEA relies on the quality of inputs provided for the model. The Schwarz-P structures of interest in this work were manufactured by Selective Laser Sintering as discussed in the previous chapter. To accurately capture the material's behavior, tensile test specimens were manufactured on the same machine. The tensile test specimens were designed according to ASTM D638-14 standard [79]. The test specimens were manufactured with the longitudinal symmetry axis aligned with the vertical build orientation. Majewski et al. [83] showed no apparent effect of orientation on the tensile strength, Young's Modulus. Only the specimens manufactured in ZY showed lower strain at failure. As the Nylon-12 specimens tested in this study did not undergo failure, mechanical properties to consider are orientation-independent; hence specimens are manufactured only in the Z direction. Figure 45 shows the test setup used for the study; the black dots on the specimen are marker points used to track strain in the gauge length using a video extensometer. The video extensometer was calibrated before the start of each test.

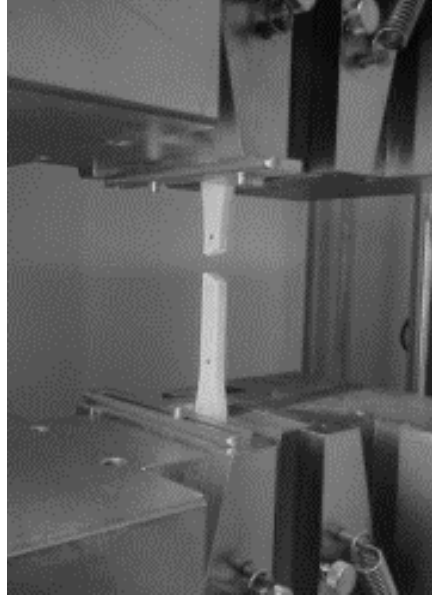


Figure 45 Tensile test set up to evaluate Nylon-12 stress-strain response.

Uniaxial tensile tests were carried out at a multiple strain rate ranging from  $10^{-5}$  to  $10^{-1}$ . The stress-strain data from the  $10^{-5}$  strain rate test was used to model the material for FEA. The data was recorded at the rate of 100 readings per second. Figure 46 (a) shows the true stress true strain data calculated from the gripper force data recorded on an Instron 5985 machine.

To model Nylon-12 for this study, an isotropic elastic multilinear plastic material model was selected, which depends on two components. The elastic material definition requires two independent elastic constants Young's modulus and Poisson's ratio. Young's modulus is calculated with a MATLAB script. Poisson's ratio is 0.4 based on the experiment carried out by Stoia et al [84]. The plastic stress plastic strain curve as shown in Figure 46 (b) is given as input in the form of a table. Mises yield surface is used to define isotropic yielding.



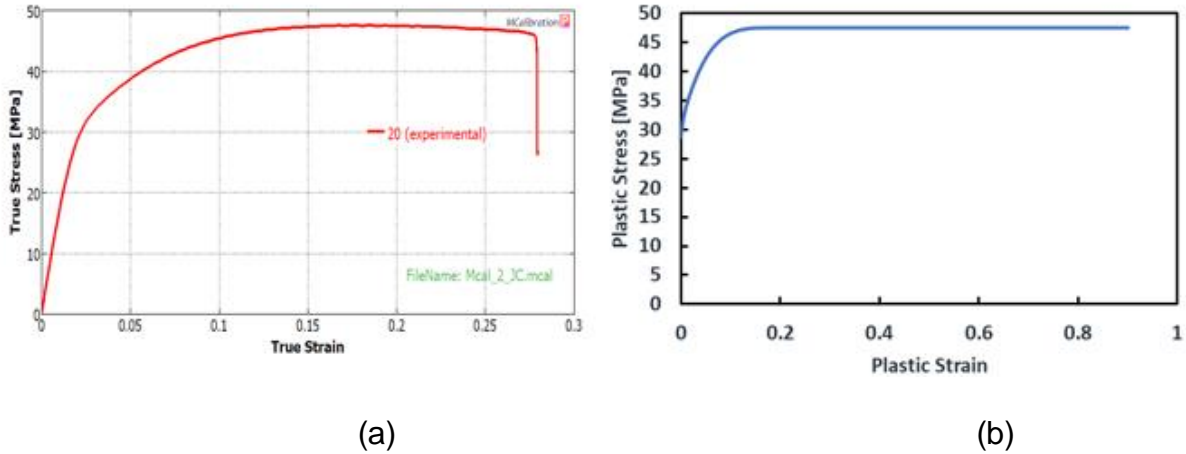


Figure 46 Stress-Strain curve for Nylon-12 at  $10^{-3}$  strain rate (a) Test data (b) Plastic stress- plastic strain conversion of the test data for use in FEA.

#### 4.3. Mesh Convergence:

Explicit Finite Element (FE) codes such as LS-Dyna [86] and Abaqus\Explicit [87] are used to analyze highly nonlinear deformation events such as car crashes and drop tests. The codes can predict the behavior of structures in such events, given that the underlying finite element model is constructed correctly. Once an appropriate material model has been developed, the choice of element type and element size is the most fundamental among all the considerations required to construct an accurate FE model.

A mesh convergence study determines the appropriate element size for the mesh. The study was carried out for the unit cell of the Schwarz-Primitive unit cell with uniaxial compressive loading conditions. The mesh size was reduced from 0.5 mm in steps to 0.1 mm, as shown in Figure 47. The material model explained in the previous section was used

for the simulation. An infinitesimal displacement in the  $-Z$  direction was applied at the top face of the unit cell using a rigid plate.

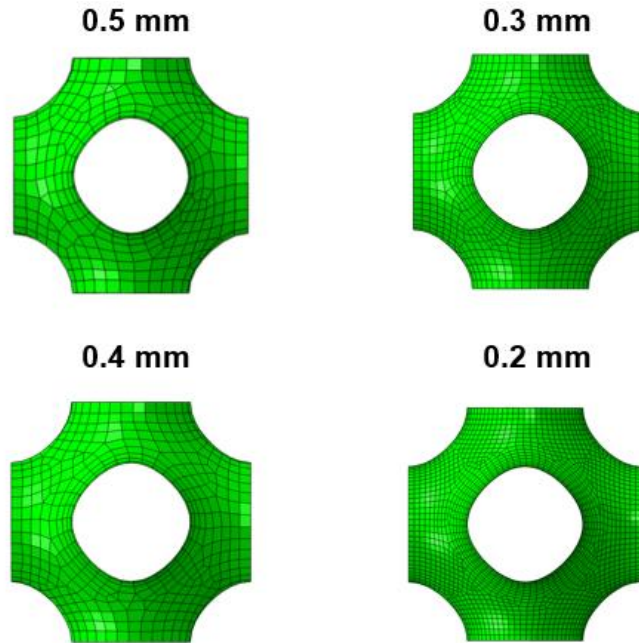


Figure 47. Mesh of S4 elements for Schwarz Primitive unit cell with element size 0.5 mm, 0.4 mm, 0.3 mm, and 0.2 mm.

The bottom face of the cell was in contact with another rigid plate at the bottom. The rigid bottom plate is constrained in all three directions. The reaction force on the rigid top plate is recorded via reference point. The job is executed in the explicit solver of Abaqus, and the CPU time required to complete the job is recorded. The CPU time is directly proportional to the number of nodes in the model.

Figure 48 shows the result of the mesh convergence study, where the reaction force of the unit cell is plotted with a blue line, and the time required to complete the simulation is plotted with the orange curve.

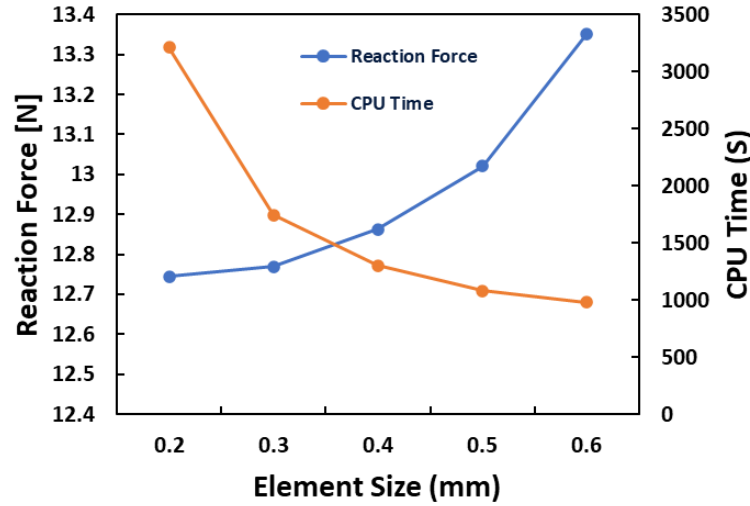


Figure 48 Mesh convergence graph showing reaction force on the unit cell with blue curve and time required to run the complete simulation in seconds.

As the mesh becomes finer, the result obtained is accurate, but the number of elements is higher, resulting in higher simulation time which is evident from the graph in Figure 48. The reduction of mesh size from 0.4 to 0.3 mm results in a 0.72% decrease in the resultant force and a 34% increase in the simulation time. On the further refinement of mesh size to 0.2 mm, the resultant force is reduced by 0.19%, and runtime is increased by 90%. This means the results obtained are only 0.19% different, but the required runtime is almost doubled. Hence the 0.3 mm element size was used in this study.

#### 4.4. Finite Element Model

The Force-Displacement curve for the cellular structure is obtained by simulating the uniaxial compression test of the cellular structure. The Finite element model for energy absorption characterization of the cellular structure is shown in Figure 49. The cellular structure is meshed as described in section 4.1. The cellular block is positioned between

two rigid plates. The rigid bottom plate is constrained to move in all directions, and the rigid top plate is allowed to move in only the Y direction and constrained in other directions. The rigid top plate is given a displacement of 30 mm in 750 seconds, giving a strain rate of 0.001 per second for a 40 mm high cellular structure. This loading condition is like the actual testing condition of the cellular structure. Semi-automatic mass scaling is used to keep the simulation time in check. A target time increment of 0.005 seconds is given; if the stable time increment falls below 0.005, the element's density will be increased to make the stable time increment below 0.005.

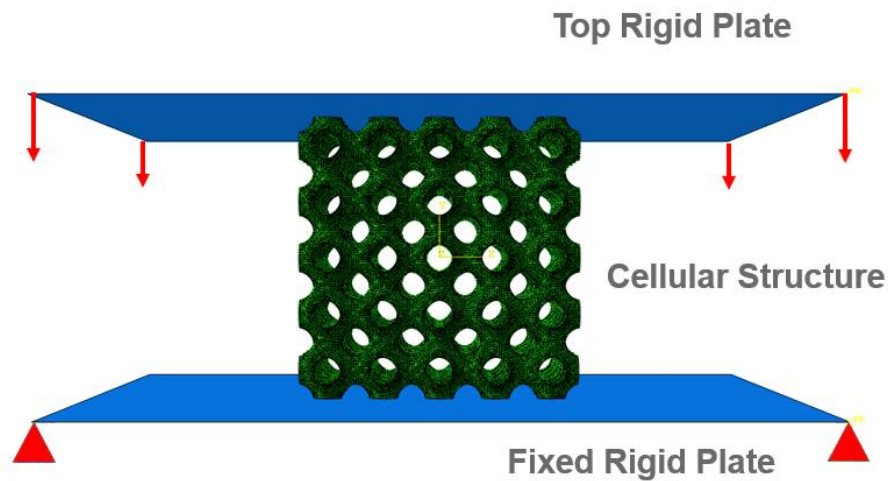


Figure 49. Finite Element Analysis model of Schwarz-Primitive structure with boundary conditions

After the first collapse of the cells, the walls of the cellular structure come in contact, an explicit general contact is defined to account for the contact between the rigid plate and cellular block as well as self-contact of the cellular structure. A homogeneous shell section is assigned to the cellular structure with five integration points across the thickness of the shell. Simpson's 5-point integration rule is used across the thickness. The

material model developed in section 4.2 is associated with the shell section. The results of the simulation are discussed next.

#### 4.5. Results

The explicit method of finite element analysis is conditionally stable. The time step of each increment must be less than the critical time step defined using the minimum element size ( $L^e$ ) and the speed of stress wave in the material ( $C_d$ )

$$\Delta t_{stable} = \frac{L^e}{C_d} \quad (14)$$

For a linear elastic material,

$$C_d = \sqrt{\frac{\lambda+2\mu}{\rho}} \quad (15)$$

Where  $\lambda$  and  $\mu$  are Lamé's constants and  $\rho$  is the density of the material. The critical time is a function of the smallest element size and material density. If few elements are causing smaller timesteps, the density of those elements is increased to maintain a defined timestep. This method to control timestep is called mass scaling.

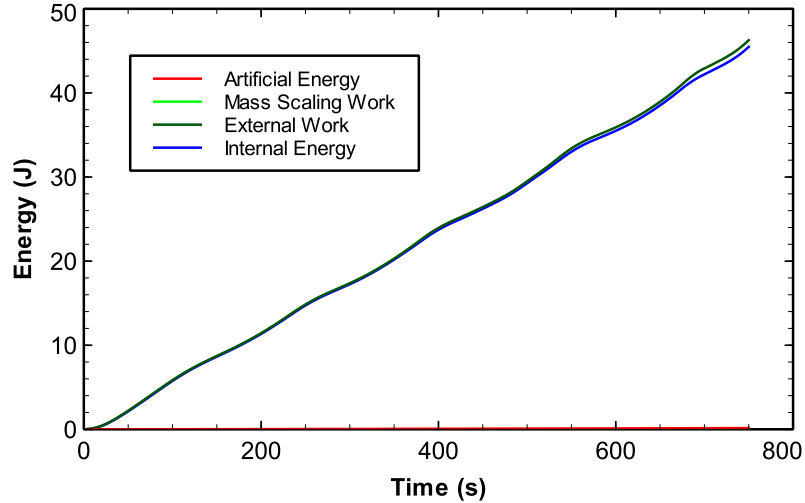


Figure 50. Energy balance for the Schwarz-P uniaxial compression simulation showing low artificial energy and low mass scaling work as compared to external work.

It is essential to verify the energy balance for the explicit solution. As semi-automatic mass scaling is used for the simulation, it is critical to check the mass scaling work in the complete simulation. External work, internal energy, artificial energy, and mass scaling work are plotted against simulation time in Figure 50. The ratio of external work done to internal energy at the end of the simulation is 0.98. The ratio indicates that 98% of external work is converted into internal energy, and 2% of the energy is required for mass scaling work and added as artificial energy to compensate for overclosures in the contact. The artificial energy in the simulation should be less than 5% [85]. In this work, the artificial energy added due to mass scaling is less than 2% - hence, the mass scaling assumptions are valid.

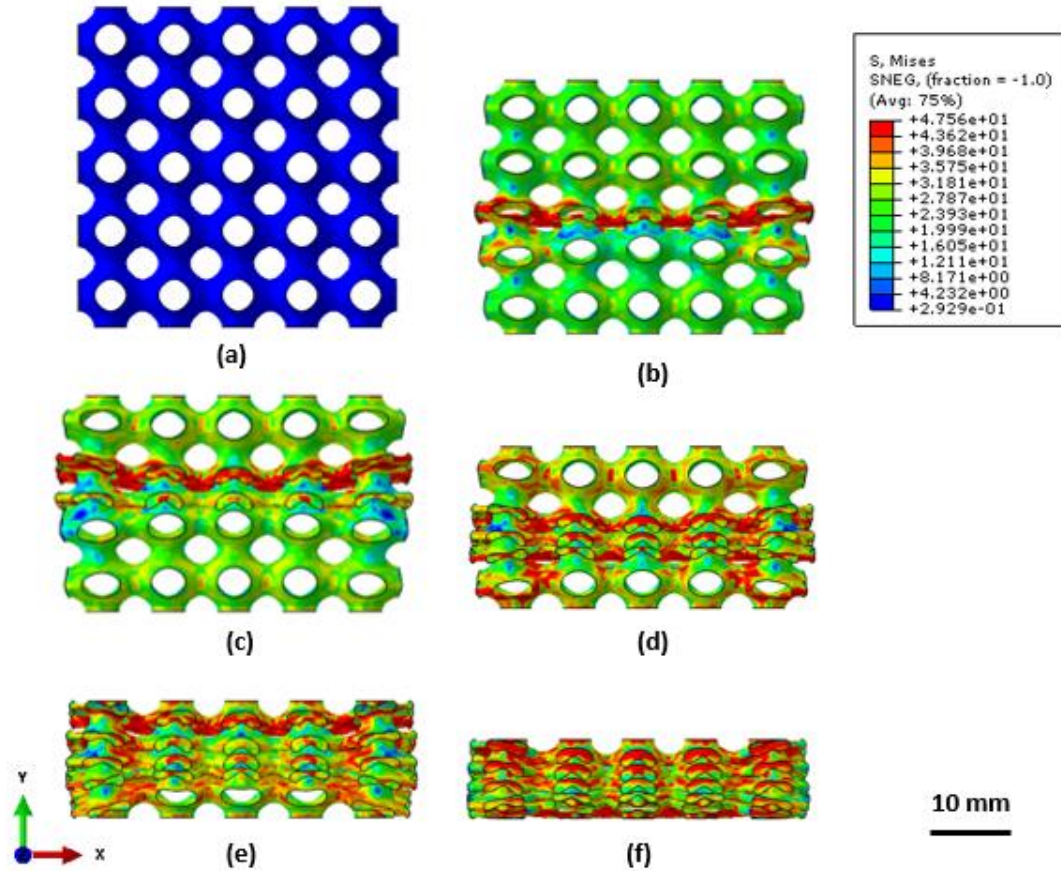


Figure 51 Deformation pattern and von mises stress contours in the Schwarz-Primitive cellular structure at (a) 0 mm, (b) 6 mm, (c) 12 mm, (d) 16.5mm, (e)21 mm, and (f) 27 mm displacement

Figure 51 shows a front view of the deformation pattern in the Schwarz-Primitive structure of 0.4 mm wall thickness. The top platen compresses the structure at a strain rate of  $10^{-3}$  per second. As the loading force on the structure increases, the central cell experiences high stresses on the shell walls. The stress at the top and bottom layers of the shell exceeds yield strength. Plastic hinges are formed, and the central cell collapses first, increasing the adjacent cells' stress level. This results in the collapse of the entire central row of the structure, giving rise to the first undulation in the force-displacement curve, shown in Figure 51. Further loading triggers the collapse of cell layers above and below

the central layer alternately. The decrease in the reaction force indicates each collapse as the structure's stiffness decreases once plastic hinges are formed; the cell can collapse without significant load. The structure regains stiffness when the collapsing cell's top walls come in contact. Figure 52 compares the force-displacement response obtained by simulation results with the test data. The onset strain of densification predicted by simulation has a 7.5% error. It is evident that the initial response of the simulation is close to the test data, but as deformation increases, the distance between peaks and valleys increases. The delay in contact can be attributed to the reduced thickness of shell elements during the simulation due to artificial adjustment during large deformation.

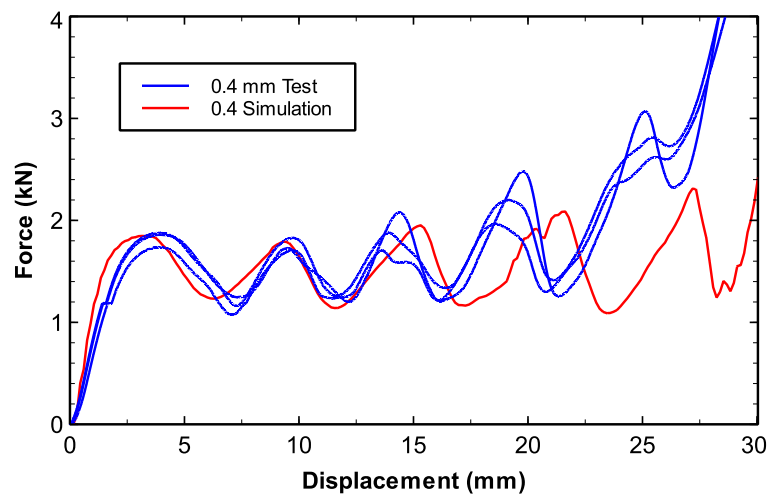


Figure 52 Force Displacement response of 0.4 mm Schwarz-Primitive cellular structure under uniaxial compression loading, comparison with the test data

#### 4.6. Drawbacks of the conventional shell model

Conventional shell elements have shown great promise in modeling sheet metal parts with uniform thickness and low aspect ratio in the automotive and aerospace industries. Additively manufactured lattice structures have a high aspect ratio (thickness



ratio to the unit cell length), and hence, the FE model's accuracy decreases as the sheet-based lattice's relative density increases. The thickness of the conventional shell elements is assigned through the user-defined section. The solver changes the thickness to avoid erroneous contact engagements related to thickness engagements. This thickness change is limited to only contact detection and not for stiffness calculation, but for the current study, this affects the energy absorption characteristics of the structure, especially at large strains as shown in Figure 51. To enhance the applicability of the shell elements of the TPMS structures, continuum shell elements are explored as they have advantages over conventional shell elements. The continuum shell elements are explained in Section 4.7.

#### 4.7. Continuum Shell Elements

Continuum shell elements or solid shell elements discretize the three-dimensional body as opposed to conventional shell elements, which only discretize the reference surface. Figure 53 illustrates the difference between conventional and continuum shell elements. For continuum shell elements, the thickness is determined from the nodal position. Continuum shell elements have only a translational degree of freedom and in appearance is similar to 3D continuum solids. The main advantage of continuum shells over conventional shell elements is that they can be stacked; hence, they are applicable to structures with a high aspect ratio. The thickness direction, element normal, and stacking direction in continuum shell elements are determined by nodal connectivity, as shown in Figure 54. For the triangular shell element (SC6R), the face 1-2-3 is the bottom face, and 4-5-6 is the top face. The normal direction is always the stacking direction for the

continuum shell elements. Multiple layers of the continuum shell elements can be added in the normal direction, increasing the model's accuracy. Figure 55 shows normals to the element surface for the Schwarz-P structure. Hence elements can be stacked in the thickness directions. To the best of our knowledge this is first attempt to model TPMS structures with continuum shell elements with the possibility of stacking them to improve accuracy in the solution as well as in contact detection.

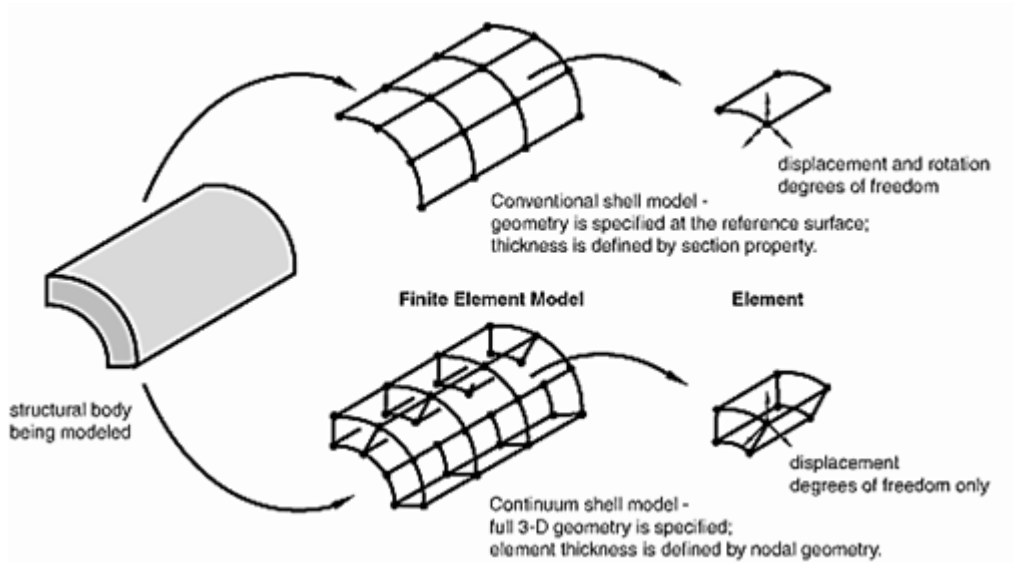


Figure 53 Difference in conventional and continuum shell element modeling [87]

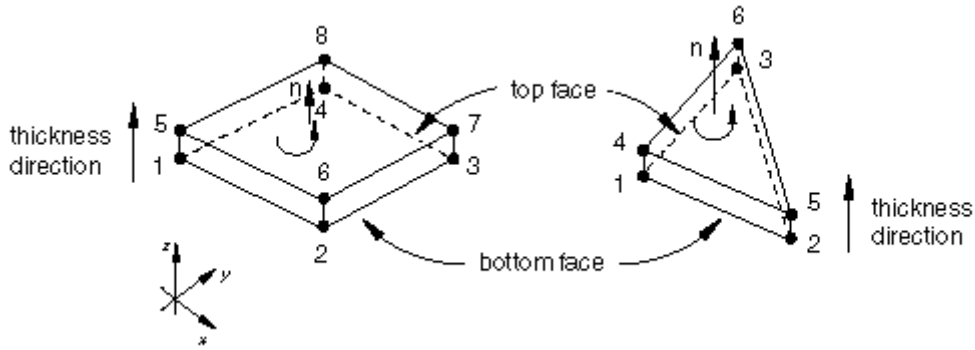


Figure 54. Normal and thickness direction for continuum shell elements indicate an element's top and bottom face [87]

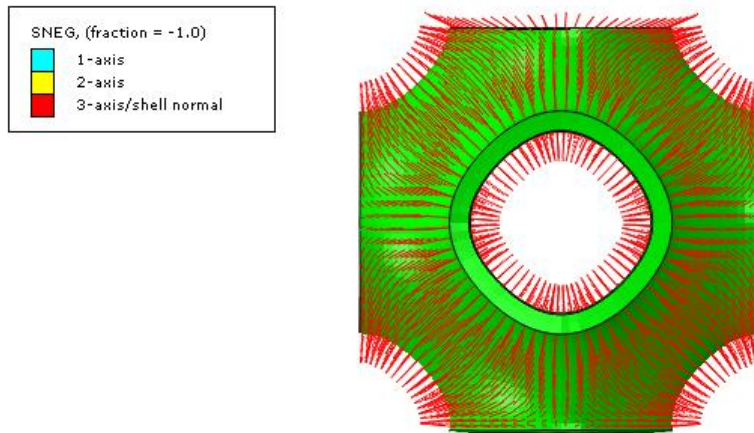


Figure 55 Direction of shell normal for TPMS Schwarz Primitive unit cell shown by red lines

#### 4.7.1 Patch Test

A patch test is carried out for verification of element equivalence of conventional shell elements (S4) and continuum shell (SC8) elements. In this patch test, basic deformation modes of the continuum shell elements are verified with conventional shell elements and analytical solutions [87]. An SC8 element is loaded with displacement

boundary conditions into its basic deformation modes, and the results are compared with the equivalent modes obtained with the S4 element. Figure 56 shows the deformation modes of S4 and SC8 single elements loaded in equal and opposite directions (the S4 element is at the center of the SC8 element). It is evident that these deform equally. Which shows that the S4 and SC8 elements are equivalent.

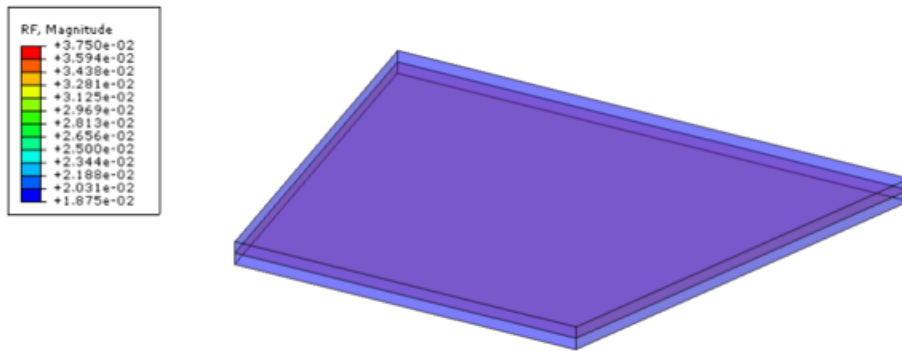


Figure 56 One of the patch tests to verify the equivalence of S4R and SC8R elements

#### 4.8. Continuum shell model for Schwarz-P

The model developed earlier with conventional shell elements was used to generate a solid element model. The offset (create solid layers) function in the Abaqus mesh toolset is used to generate solid elements on both sides of the reference surface. The newly generated elements are stacked in the normal direction, as shown in Figure 55. Generating solid elements for a uniform thickness structure is comparatively straightforward as each node must be offset by an equal distance. The complete Schwarz-Primitive structure modeled with continuum shell elements is shown in Figure 57. This model consists of

13,85,940 nodes and 9,15,360 elements of type SC8R. The material model, section assignment, and boundary conditions remain the same as in Section 4.4.

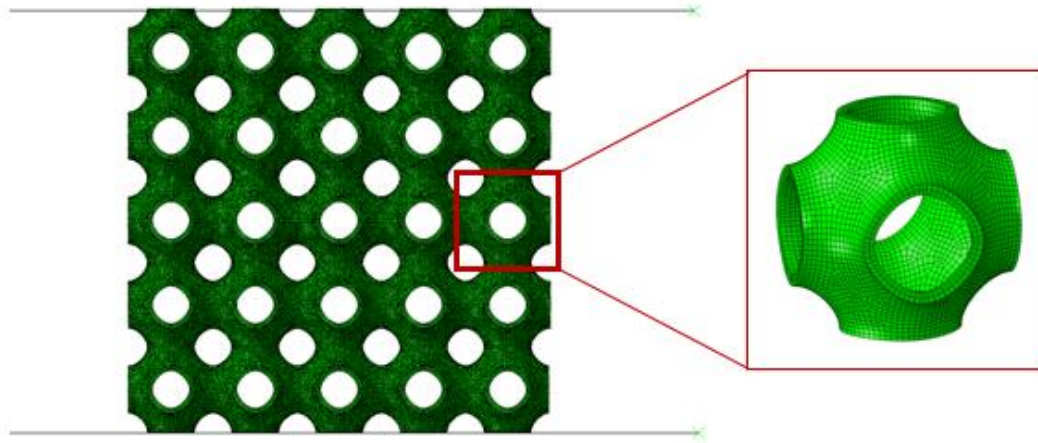


Figure 57 Continuum shell model of Schwarz-Primitive structure 0.4 mm (b) Mesh for the unit cell

#### 4.9. Variable Thickness Continuum Shell Modeling

While not essential to designing graded cellular materials using a field-driven design approach, the ability to model variable-thickness cellular structures efficiently in the context of large deformation analysis is vital for the rapid validation of design performance without resorting to expensive manufacturing and test cycles. As a result, it is essential to develop a methodology to generate variable thickness continuum shell models. The structures studied till now were uniform thickness structures and can be easily modeled with the offset command from mesh modeling software such as Hypermesh. For field-driven design however, this becomes a limitation.

Figure 58 shows the difference between uniform thickness and variable thickness continuum shell elements. The green plane represents a section of the mid-surface. To

generate uniform thickness continuum shell elements, the mid-surface is offset by half the thickness ( $t/2$ ) in both directions, but it is not straightforward for the variable thickness shell elements. Each node must be offset by a different value, as shown in Figure 58.

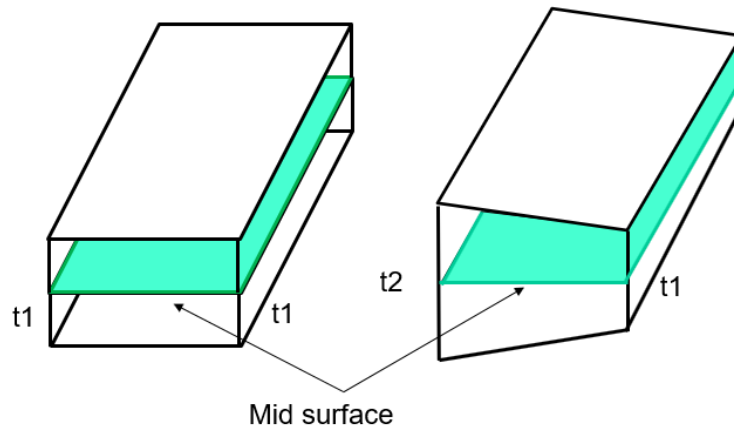


Figure 58 Difference between offset function for uniform thickness and variable thickness continuum shell elements.

Four elements share a node, and the node connectivity must be retained. It is impractical to do this procedure manually for the entire structure with 1.3 million elements; hence an Abaqus script was developed to generate a mesh with variable thickness continuum shell elements. The flowchart of the script is given in Figure 59, and the script is provided in Appendix C. The input required for the script is the element number and thickness associated with each element. The given script groups the elements according to the associated thickness. After the grouping, the elements in each group are offset by the thickness associated with the group. This approach is more efficient than offsetting each element due to the number of elements involved in the operation. Each node shared by four

elements generates four new nodes. These four nodes are then equivalenced at the midpoint to generate the connected mesh.

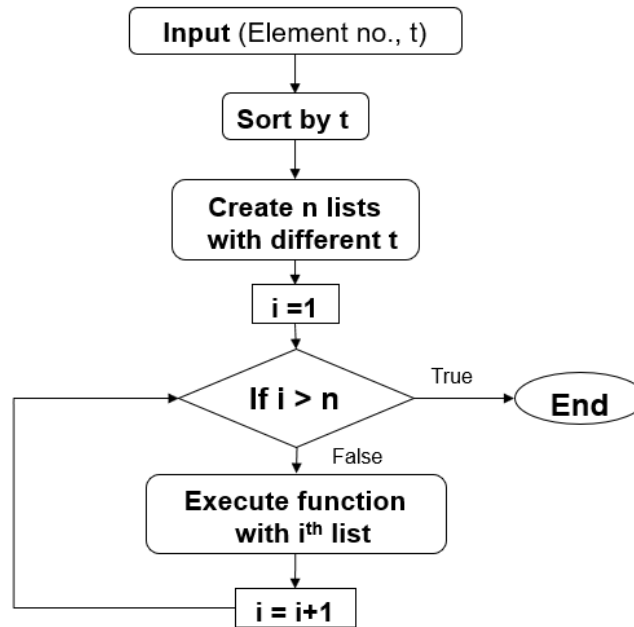


Figure 59. Flowchart for Abaqus script to generate variable thickness continuum shell elements.

This methodology successfully develops variable thickness continuum shell element models of the Schwarz-Primitive structures. To the best of our knowledge this is first study modeling Schwarz-P structures with continuum shell elements. A validation study for the variable thickness structures is presented in chapter 5.

#### 4.10. Conclusions

This chapter summarizes the development of the shell model for the TPMS Schwarz-Primitive structure. The isotropic multilinear plastic material model is suitable for Nylon-12 for quasi-static simulation. A mesh refinement study determines suitable

element sizes for the Schwarz-Primitive cellular structure. The aspect ratio for the thickness to the unit cell is such that conventional shell elements can not capture the self-contact of cell walls during deformation. The continuum shell elements are more suitable to model TPMS structures with relative density in the range of 0.14-0.25. Another advantage of continuum shell elements is stacking, which is effective in modeling accurate deformation of the Schwarz-Primitive structure. A methodology is developed to model variable thickness TPMS structures with continuum shell elements efficiently. Armed thus with the capability to model variable thickness TPMS structures, the thesis now moves to leveraging this modeling capability for the design of field-driven cellular structures.



## CHAPTER 5: FIELD DRIVEN DESIGN

The primary aim of this thesis is to develop a methodology for the design of a new class of cellular materials optimized for energy absorption using simulation data. Topology optimization is also used to enhance energy absorption of the structures. Yang and Li [86] developed advanced cuttlebone like (CLL) material with high energy absorption with topology optimization. A unit cell is optimized for internal energy as objective function and complete structures is designed by repeating this unit cell. Wu et al. [87] proposed a topology optimization method with local volume constrains and achieved organized complexity to give optimized stiffness design. The method is useful in generating bone like porous structures in the interior of given shape. The data driven approach is also a promising method for design. Wang et al. [88] used data driven topology optimization approach using Latent Variable Gaussian Process. A library is created with different classes of microstructures and their stiffness and using the data topology optimization is carried out which results in structure with multiple classes of microstructure. The approach is used with objective function of stiffness. It is promising approach to be used in future for energy absorption problems. It is important to understand how a unit cell performs as a function of position in a big structure in the context of energy absorption. Machine learning based design approach is used by Gu et al [89] instead of FEA to optimize specific property for a given structure. The patterns are discovered in high performing cells for the property in consideration. The approach is computationally effective and can be used to design energy absorbing structures. This approach also requires large number of unit cells characterized

for the specific property. In this study Field driven design approach is used which can be considered as primary stage for doing topology optimization. This thesis aims to begin with a high-performing cell shape (in this case, TPMS Schwarz-P) and further improve it using simulation information. The generic approach used in this study is called field-driven design, where a field, either prescribed mathematically or obtained from FEA is superimposed over geometry to modulate thickness locally. Enabling this creates three new research tasks, each of which is discussed in the following sections.

### 5.1. Field-Driven Design of Cellular Materials

Implicit modeling software such as nTopology Platform [88] has enabled the field-driven design of cellular materials. In this approach, fields are imported from FE solutions or can be generated from different functions and superimposed on cellular designs to drive thickness and/or size gradients. One example of such an approach is shown in Figure 60 where the stress field is obtained from a static structural analysis on a homogeneous excel structure and leveraged to refine density locally. In field-driven design, the selection of the field is critical to achieving the objective of the design, yet there is little prior work in the literature examining the different types of fields for cellular materials, with some exceptions such as uniform and stochastic fields, which have received some attention [6].

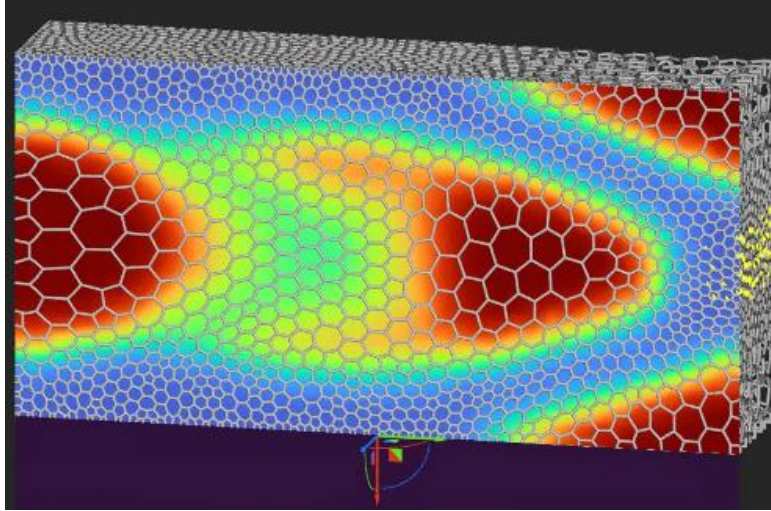


Figure 60 Example of a field-driven design to drive decisions on cell size and member thickness locally using an imported stress field [88].

In this work, fields are first categorized as rational and stochastic, as shown in Figure 61. The rational design method is typically used in metamaterial design [90] to obtain desired properties by changing either material distribution or changing architecture locally. Rational design is based on the mathematical formulation or derived from simulation. Rational fields are further divided into analytical and simulation-driven fields. Analytical functions define the analytical fields, whereas simulation-driven fields are obtained from the numerical simulation of the baseline design. Any scalar parameter from the output database of the simulation based on the objective can be used to influence design. On the other hand, stochastic fields are generated randomly, and for this study, they are categorized as simplex noise fields and cellular noise fields, in which cell generation is stochastic. Each of the four main categories of fields were evaluated in this work and are discussed in turn in this chapter.

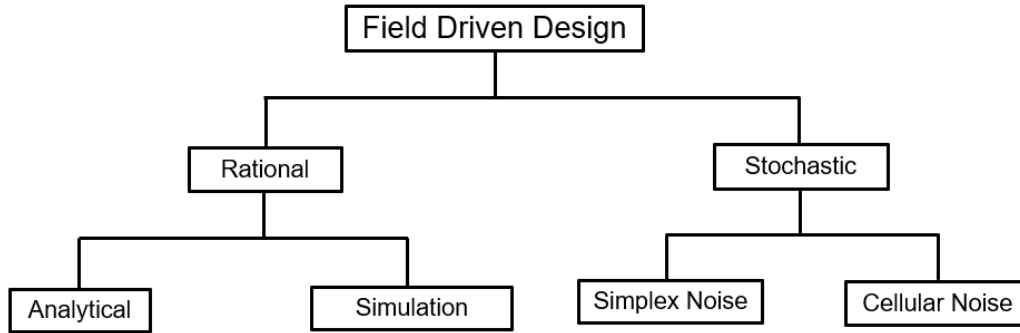


Figure 61 Types of fields used in the study

## 5.2. Results

The Force-Displacement response of a Schwarz primitive structure with a continuum shell model is shown in . The curve shows a good correlation with the test data, improving on the result with the conventional shell elements, shown previously in Figure 51. The peaks and valleys in the curve occur at the same displacement of the top platen as observed in the Schwarz-Primitive structure test. summarizes the energy absorption parameters of a 0.4 mm shell-based Schwarz-P structure. The parameters are extracted from force-displacement data obtained by test and finite element simulation using conventional and continuum shell models. The onset strain of densification predicted by simulation 0.6496 is closer to the OSD observed in the test (0.6532). There is a 9.2% error in the prediction of OSD with conventional shell elements.

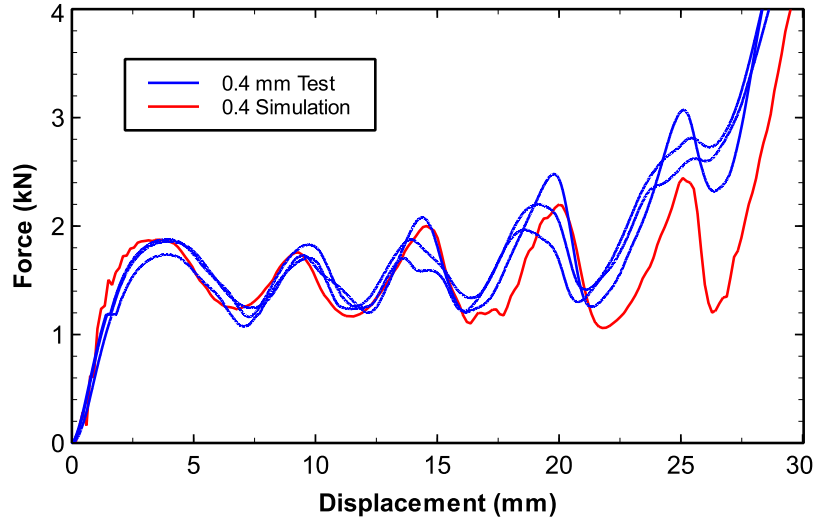


Figure 62 Force Displacement response of 0.4 mm Schwarz-Primitive cellular structure under uniaxial compression loading with continuum shell model, comparison with the test data.

Table 7 Comparison of energy absorption characteristics for 0.4 mm Schwarz-Primitive structure

Sr No	Method	OSD	Energy Absorbed [J]	SEA[J/g]	ULC
1	Experimental	0.65	44.34	4.92	0.23
2	FEA (Conventional Shell)	0.71	43.69	4.84	0.18
3	FEA (Continuum Shell)	0.65	39.81	4.41	0.20

The energy absorption measured in the simulation with the continuum shell model is less than that observed in the test because the peak stress level in the last undulation is low. Even though energy absorption predicted by conventional shell model is closer to the test data, that happens due to extended OSD with conventional shell model and not due to a better approximation of the force-displacement response as can be seen by comparing Figures 51 and 57. The peak stress level predicted by the conventional shell model is less than that predicted by the continuum shell model. Comparing the conventional and

continuum shells shows that undulations in the conventional shell model occur at higher strain, indicating delayed contact between collapsing cell walls. As the contacts are accurately captured in the continuum shell model, it is concluded to be a better choice for modeling TPMS structures to study complete deformation under uniaxial compressive load.

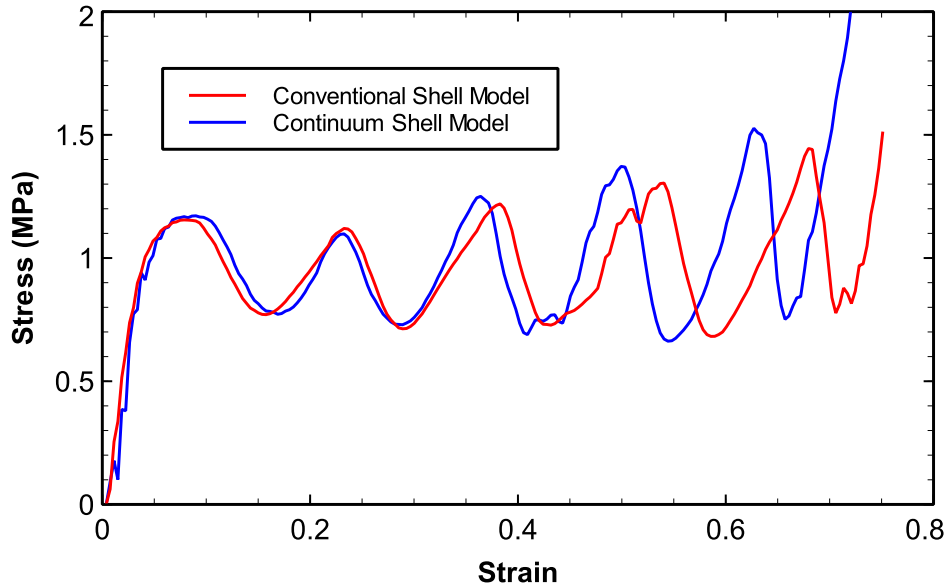


Figure 63 Comparison of Stress-Strain curves obtained from TPMS Schwarz-Primitive model with conventional and continuum shell model.

### 5.3. Simulation Driven Design

It is important to answer a few questions to apply simulation-driven design for the energy absorbers, such as: (i) which field parameter should be chosen? (ii) what stage of the deformation should the field be extracted from simulation? (iv) how should the field parameter influence the design parameters such as thickness and cell size? To address some of these questions, a field driven design for simulation fields was developed as shown in

Figure 63 and limited in scope to studying a baseline Schwarz-P structure with a 0.5 mm wall thickness, with this thickness being the only design parameter changed in response to the field.

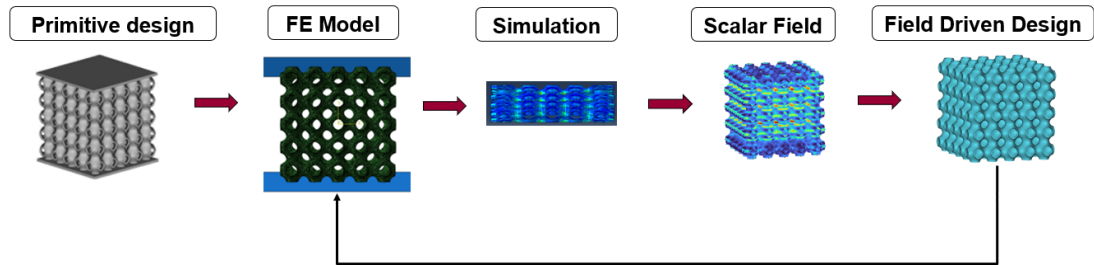


Figure 64. Field Driven Design methodology for cellular structures

### 5.3.1 Field Selection

To identify the appropriate field to use as an input to drive thickness variation, one can examine where the external work is dissipated. Figure 65 shows the conversion of external work into plastic and elastic energy for a periodic, 0.5mm Schwarz-P cellular structure (with 125-unit cells). At the end of the 30 mm compression of the structure, 95% of the external work is converted into plastic energy, and only 5% of the work is recoverable elastic energy. As the objective of this study is to enhance energy absorption, it may be hypothesized that the plastic energy density field may be used to modify the thickness distribution of the Schwarz-Primitive structure.

The hypothesis thus developed is that increasing wall thickness in proportion to the amount of dissipated plastic energy locally will improve the effective specific energy absorbed (SEA) globally. The plastic energy density field for the baseline 0.5 mm thick

structure is shown in Figure 66. To test the hypothesis a method is needed to modify nodal thickness in response to this field. This method is discussed in the next section.

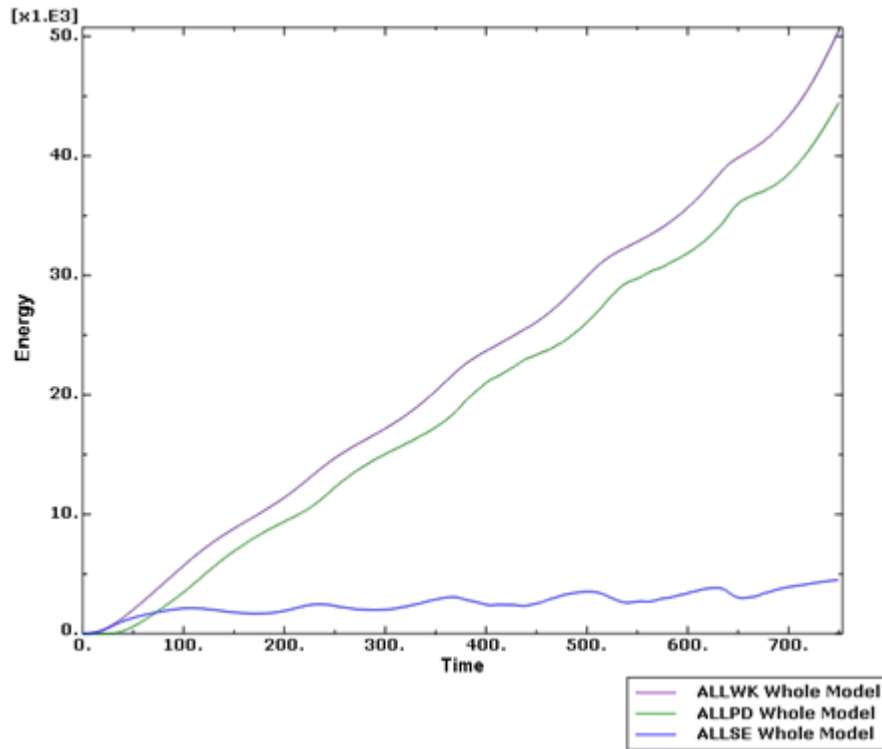


Figure 65. Energy dissipation in the Nylon-12 0.5 mm Schwarz-Primitive structure

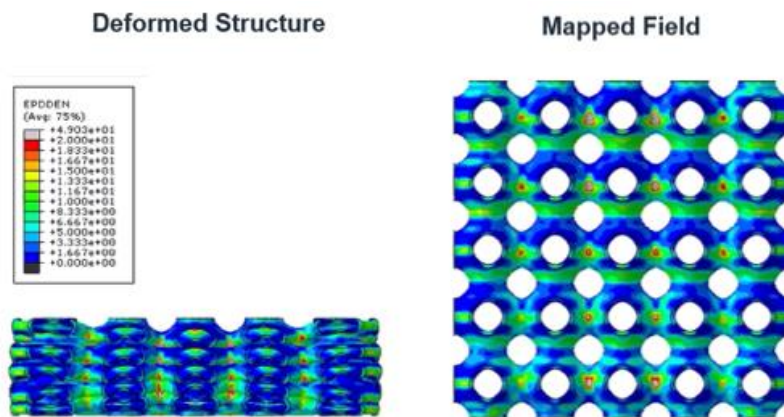


Figure 66. Deformed specimen and plastic energy density field mapping on the undeformed structure.



### 5.3.2 Thickness Distribution

To keep the relative density of the structure same as that of the baseline structure, even as its thickness changes spatially in response to the simulation-driven field, a histogram-based method was developed to distribute thickness in the structure.

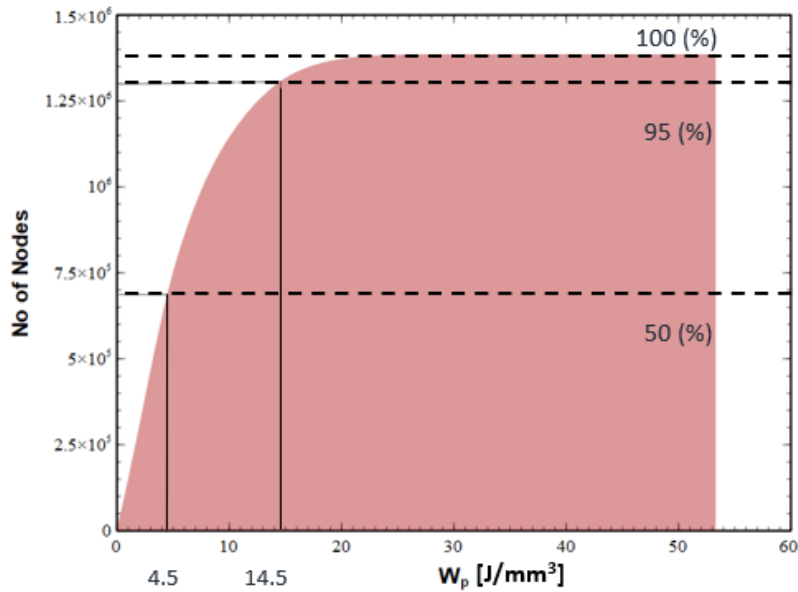


Figure 67 Histogram of No of nodes and corresponding plastic energy density.

Figure 67 shows the histogram of plastic energy density for the baseline simulation. The number of nodes is plotted on the Y axis, and the X axis indicates plastic energy density. The plot is cumulative: any point on the curve indicates the number of nodes with a plastic energy density lower than the value indicated on the X-axis. 95% of nodes experience plastic energy density lower than 14.5 J/mm<sup>3</sup>. The highest plastic energy dissipation at a node is 54 J/mm<sup>3</sup>. Only 5% of nodes have values in the range 14.5-54.2

J/mm<sup>3</sup> hence only a range from 0-14.5 J/mm<sup>3</sup> is considered to distribute thickness in the structure. The nodes at which plastic energy density is zero indicate elastic deformation.

Linear mapping was used to map plastic energy density at OSD, with the thickness distribution. 50% of the nodes experienced plastic energy dissipation lower than 4.5 J/mm<sup>3</sup>. Hence a proportion of 1:3.22 similar to proportion of plastic energy density is used to determine the range of thickness. This ensures that the total volume of the variable thickness structure remains the same as that of the uniform thickness structure. Five variants were designed: A, B, C, D, and E. Five variants are designed to assess effect of gradient on the SEA of the structure. The minimum thickness is reduced in the steps of 0.1 mm. The thickness range of all the specimens is given in Table 8.

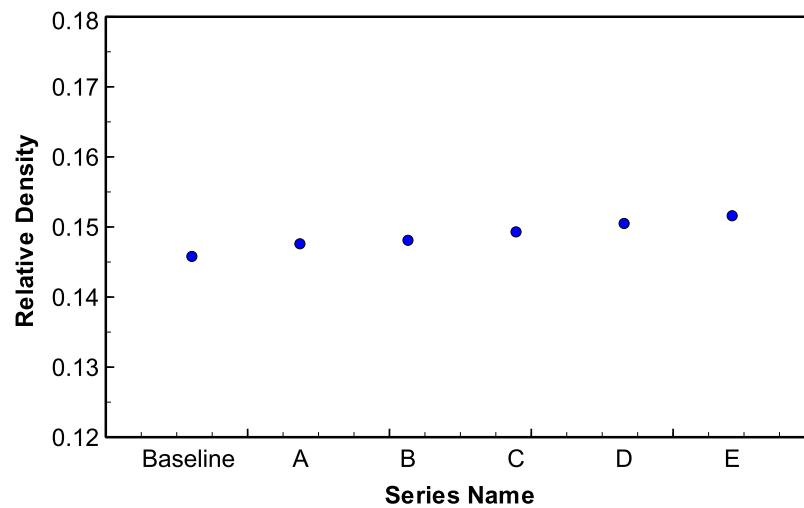


Figure 68. Comparison of relative density for the variable thickness structures with the baseline uniform thickness structure.

Table 8. Thickness range of the Schwarz-P specimens with simulation driven design

Sr. No	Name	Min. Thickness (mm)	Max. Thickness (mm)
1	Baseline	0.5	0.5
2	A	0.49	0.532
3	B	0.48	0.564
4	C	0.47	0.596
5	D	0.46	0.628
6	E	0.45	0.66

The relative density plotted in shows that the relative density increases as the thickness range increases. This is attributed to the 5% nodes that are not considered while deciding the thickness range. However, the maximum percentage difference in the relative density is 3%. Also, while calculating SEA, the energy absorbed by the structure is normalized by the nominal mass of the structure.

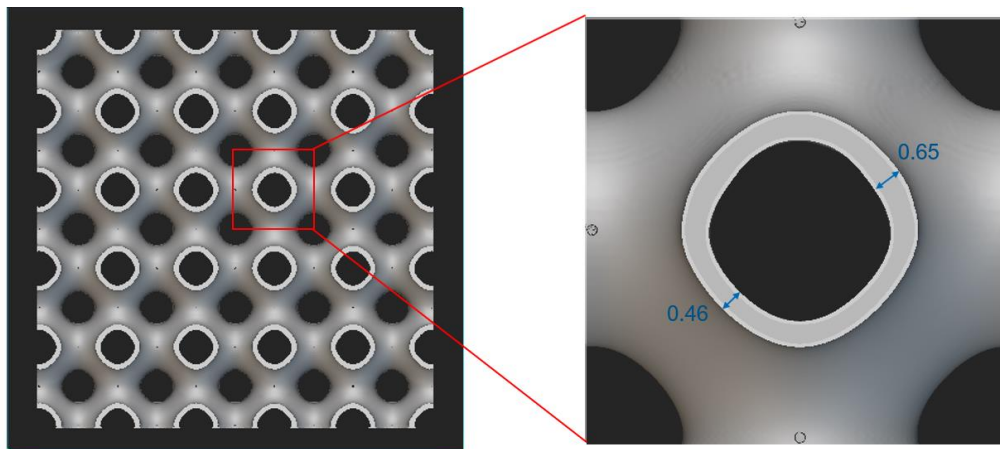


Figure 69. Cut section of variable thickness Schwarz-Primitive structure, the zoomed in picture shows measurement of the sides of a single cell.

The variable thickness structures were designed in nTopology software, leveraging ABAQUS output data as an input. The workflow for generating the structure is provided in Figure 64. The cross-section of the designed structure is shown in Figure 69, which

shows the design indeed has variable thickness according to the value of plastic energy density at that point.

### 5.3.3 Manufacturing and Characterization

The specimens were manufactured on an EOS FORMIGA P110 (EOS, Krailling, Germany) selective laser sintering machine as described previously. Figure 70 shows a single layer of specimens in the build. The specimens were manufactured in the orientation in which they were compressed. To have three replicates of each of the six variants, 18 specimens were manufactured in all.

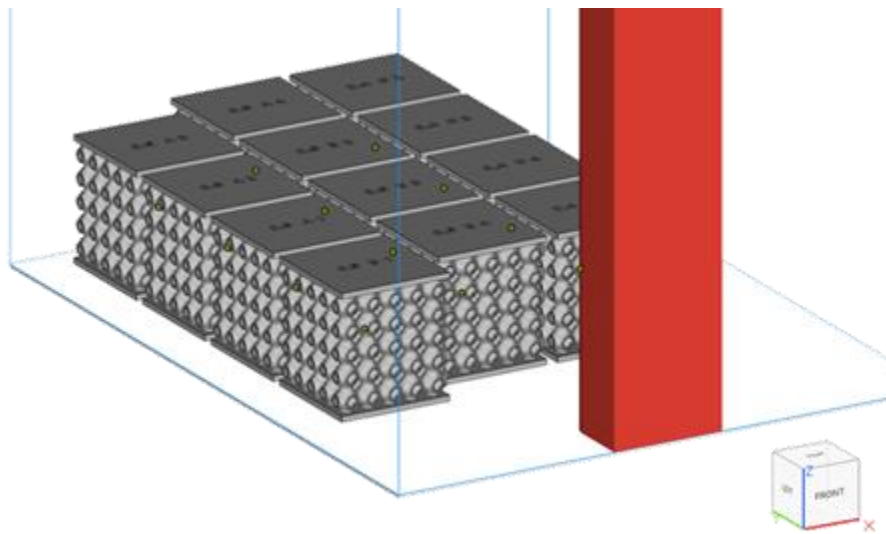


Figure 70. Build layout of the variable thickness specimens.

The specimens are subjected to sand blasting to remove excess powder particles stuck to the specimens. The post-processed specimens were weighed on an HR-250A analytical balance manufactured by A&D (Tokyo, Japan) with a 0.0001 g resolution to

obtain mass for SEA calculations. The dimensions were measured using a vernier caliper. Figure 71 shows the measurement of the bounding box dimensions for all the printed specimens. The printed specimens have 0.3%, 0.325% and 0.375% error in the height, width, and length respectively, confirming no significant distortions of the geometry occurred during manufacturing.

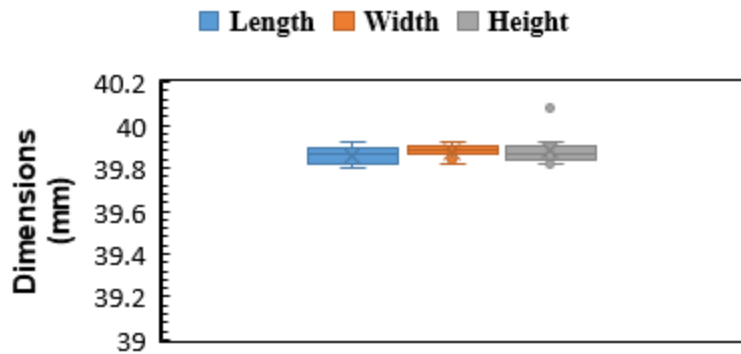


Figure 71. Dimension measurement of manufactured specimens

### 5.3.4 Compression Testing

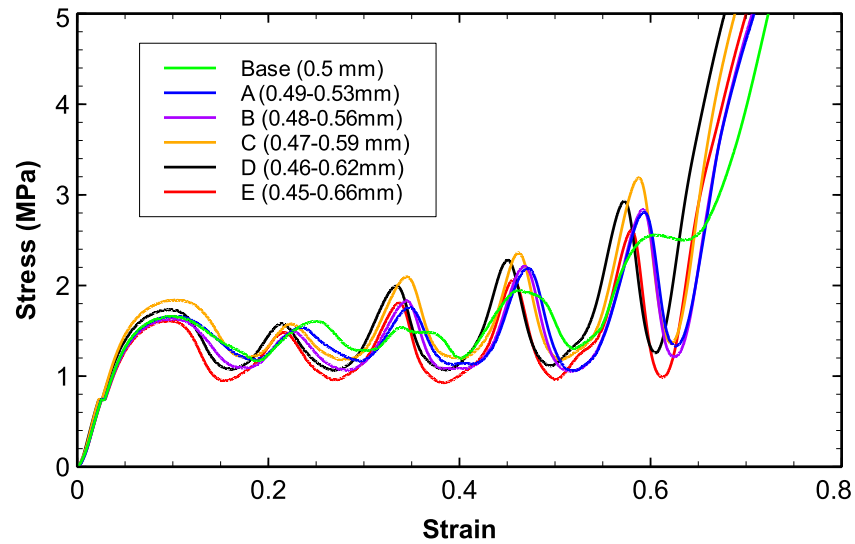


Figure 72. Stress-Strain response of the variable thickness Schwarz-Primitive structures and comparison with Baseline uniform thickness structure.

To generate results for comparison, experimental studies were conducted. The specimens were tested using an Instron 5985 universal testing machine with a 250kN load cell. A constant displacement rate was selected to effectively generate a strain rate of  $10^{-3} \text{ s}^{-1}$ . The loading direction was perpendicular to the endplates. The force and displacement data were estimated with a frequency of 50 readings per second for the entire test duration. The test was filmed using two cameras perpendicular to each other. The force-displacement curve is recorded with the machine and is processed using a MATLAB code to generate a stress-strain curve. The stress-strain curve for all the specimens is shown in Figure 72. The stress-strain curves of variable thickness specimens show undulations higher than the baseline structure. The first peak stress occurs at the same strain for all the structures, but the slope of the stress-strain curve after the first peak decreases as the

thickness variation increases. The deformation pattern for the variable thickness structures is changed as compared to the baseline structure, as shown in Figure 73. The uniform thickness structure shows the combination of ‘X’ and ‘=’ deformation pattern, whereas the variable thickness structures show layer wise collapse and only ‘=’ deformation pattern. The collapse is initiated at the minimum thickness section in each layer.

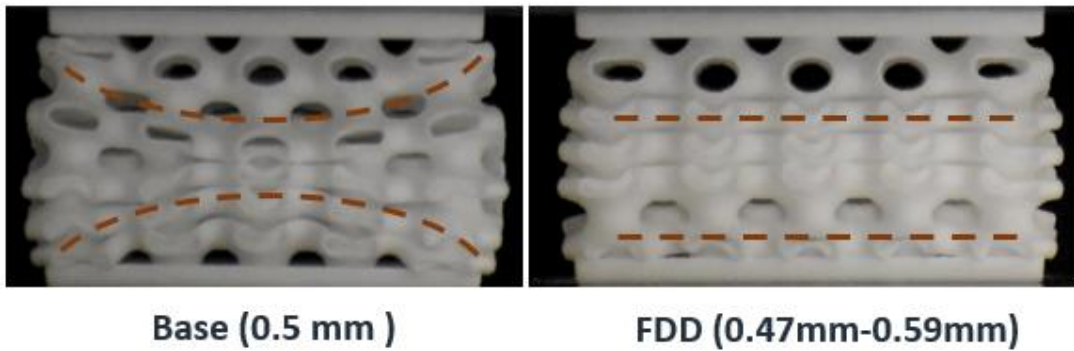


Figure 73. Comparison of Deformation pattern in the uniform thickness Schwarz-P structure and Variable thickness Schwarz-Primitive structure.

The onset strain of densification for the variable thickness structure decreases as the thickness range increases. This happens due to an increase in the slope of the stress-strain curve; hence densification occurs early with the thickness variation as indicated by Figure 74. Figure 75 compares the SEA for uniform thickness structure and simulation-driven variable thickness structures. The onset strain of densification governs the SEA as seen in Figure 74 similar trend is observed in SEA. Hence the hypothesis is invalidated, and with the simulation-driven design, SEA was reduced. The deformation pattern was changed due to the variation in thickness, and that resulted in increase in undulations and a reduction in OSD and SEA.

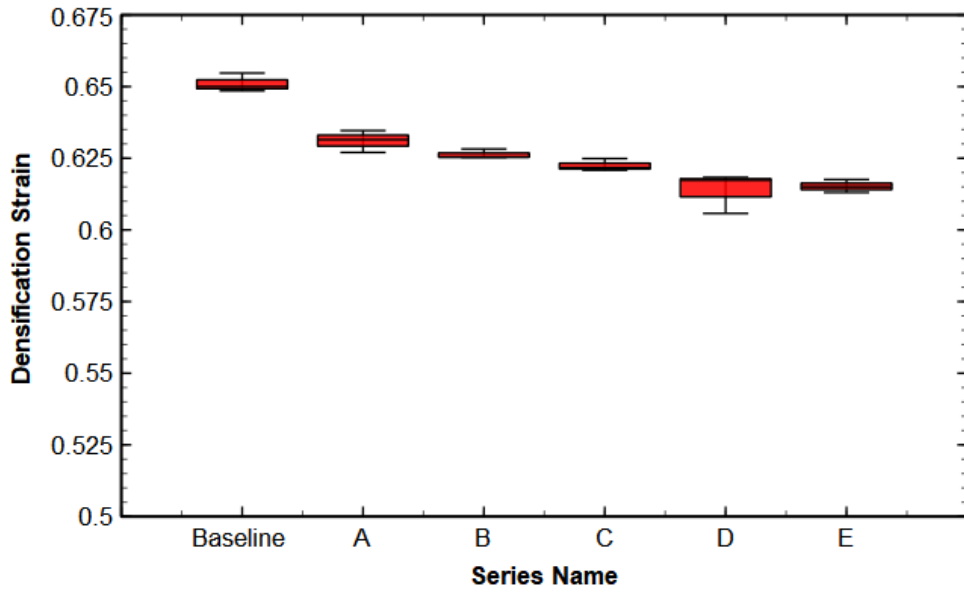


Figure 74. Densification strain comparison of the variable thickness Schwarz-primitive structure with the baseline design

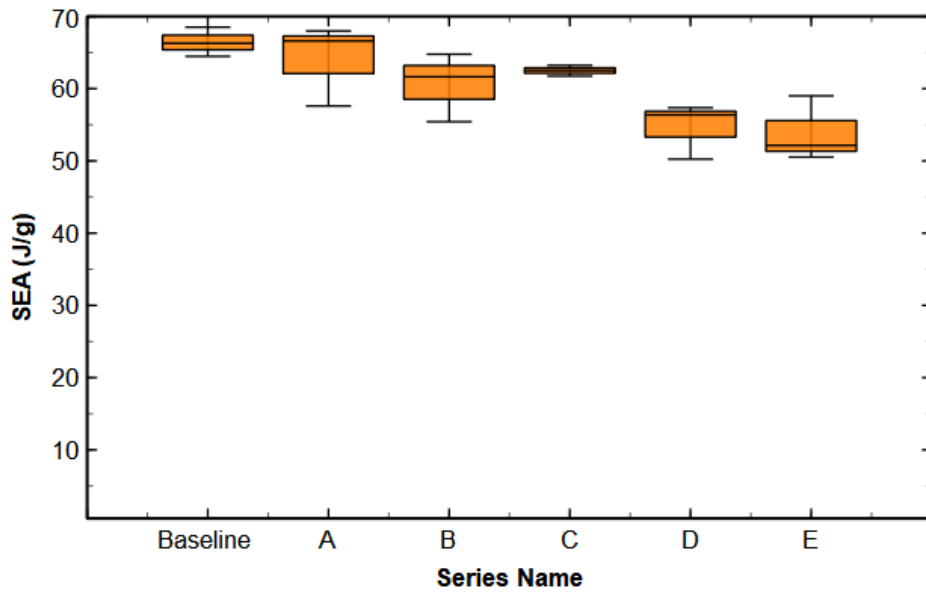


Figure 75. Comparison of SEA the variable thickness Schwarz-primitive structure with the baseline design



### 5.3.5 FEA Validation

Even though the hypothesis was invalidated, the test data was useful to validate the variable thickness continuum shell FEA model. The FEA methodology developed in chapter 4 was used to develop a variable thickness model of Schwarz-Primitive structure based on a plastic energy density field. A FEA model was developed for the ‘C’ variant with a thickness variation of 0.47 mm to 0.59 mm. The simulation was carried out in Abaqus, the explicit solver with similar boundary conditions, as explained in chapter 4. The reaction force at the rigid top plate and displacement of the rigid top plate was logged, and the stress-strain curve for the structure generated. Figure 76 shows the comparison of stress-strain curves obtained for the Schwarz-P structure with variable thicknesses ranging from 0.47 mm to 0.59 mm based on the plastic energy density field.

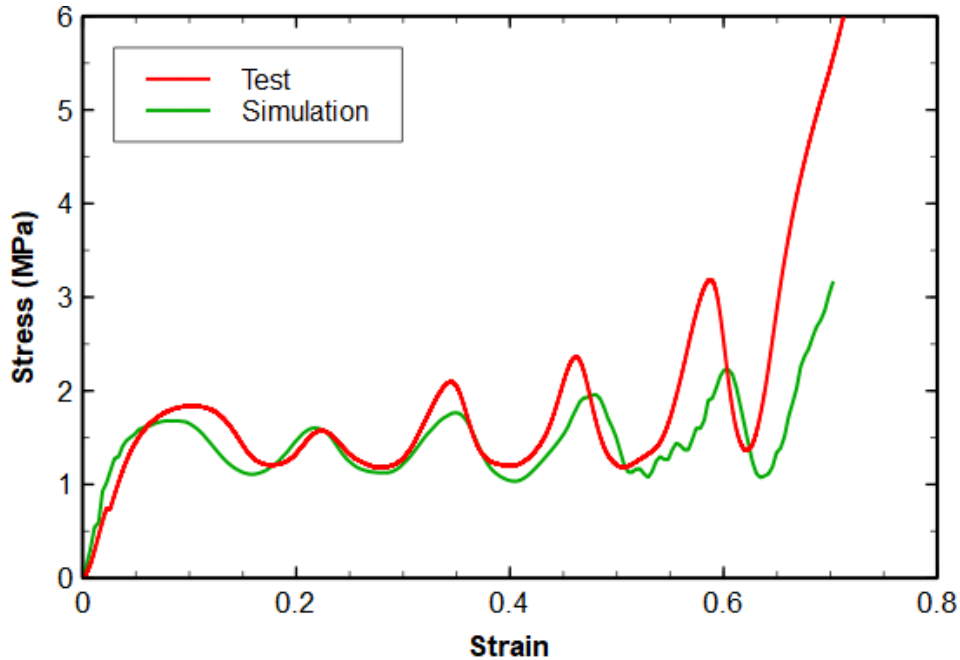


Figure 76. Comparison of Stress-Strain curves obtained by Schwarz-Primitive testing and FE simulation.

The comparison shows that the simulation is able to predict densification strain with a 2.36% error, and the error in the first peak stress is 8.79%. The simulation cannot capture the hardening effect observed in the subsequent collapse of the cellular structure. For this study, more emphasis is given to the deformation pattern itself and the form of its resulting stress plateau - a comparison of the deformation pattern in Figure 77 shows that the simulation is able to predict deformation patterns in the uniaxial compression of the variable thickness Schwarz-Primitive structure. For the variable thickness structure designed using a plastic energy density field, the thickness varies such that in most of the cells, the top half of Schwarz-P cells is lower than the thickness of the bottom half. Layer-wise collapse takes place in uniaxial compression as described. The structure's geometry governs the collapse and influences the stress-strain curve. As the deformation pattern is more important to this study and since plateau undulations are captured adequately, the current model is used for further simulation. With a strain rate dependent material model, the accuracy of the stress-strain curve can be potentially improved.

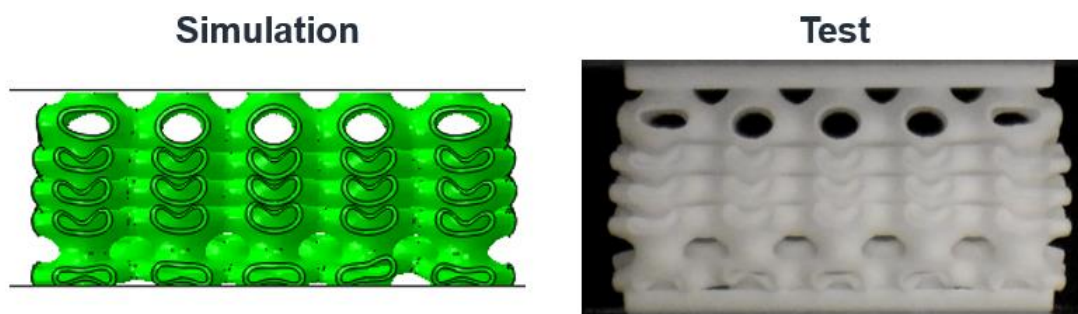


Figure 77. Deformation pattern of variable thickness Schwarz-Primitive structure at strain=0.5

Unlike the design method employed in chapter 2, the gradation is thus implemented using a simulation-driven approach instead of an a priori prescription of cell shape and wall thickness. While the field-driven design has been implemented in commercial software, it has not been applied for energy absorption applications to the best of our knowledge due to the unaddressed questions mentioned.

#### 5.4. Analytical Field Driven Design

Analytical fields are fields generated by analytical functions, with spatially varying parameters based on prescribed equations, as shown in Figure 78. One such example of an equation is  $f = 0.01 * z$ , which gives an analytical field with values of a parameter (such as wall thickness), varying in the Z direction according to this equation.

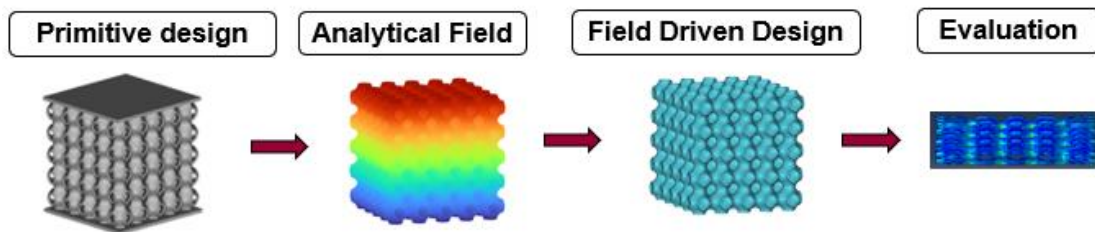


Figure 78. Workflow for the Analytical Field Driven Design

##### 5.4.1 Uniform Gradient Field

The most commonly studied field in the literature is the uniform gradient [91] [57], where the thickness of the structure is a function of Z-axis co-ordinate as given by the equation 16,

$$t = A + B * z \quad (16)$$

where  $t$  is the thickness in mm and  $z$  indicates Z co-ordinate of the point on the Schwarz-P mid surface, and  $A$  and  $B$  are constants that influence the minimum thickness ( $A$ ) at  $z = 0$ , and the scaling factor  $B$  that determines the strength of the gradient. An  $A$  value of 0.44, and a  $B$  value of 0.3 was chosen to keep the relative density of the structure the same as that of the baseline uniform thickness structure with 0.5 mm thickness.

Figure 79 shows the thickness distribution of the Schwarz-P structure with a uniform gradient scaling factor of 0.03 applied in the Z- direction. The variation is linear over the 40 mm height of the structure. The bottom row has minimum thickness indicated by the blue color, and the top row has maximum thickness shown by red.

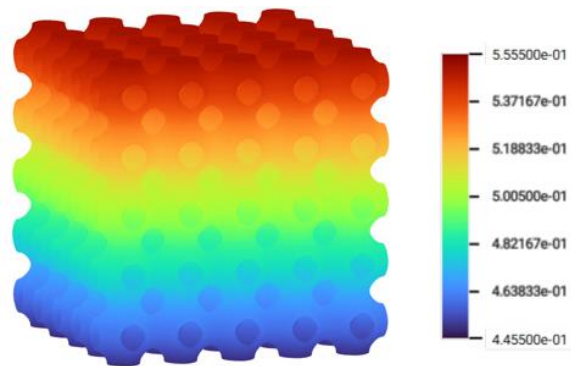


Figure 79. The overlay of uniform gradient field values varying from 0.44 mm to 0.56 mm and Schwarz-P structure.

A key reason for using the uniform gradient is the hypothesis that grading thicknesses in this manner will enable a more controlled and sequential collapse, which in turn may push out OSD and improve SEA. To examine this hypothesis, a FEA model was generated using the methodology developed in chapter 4, and simulation carried out for uniaxial compression of the uniform gradient structure as before. The stress-strain curve of uniform gradient thickness structure is compared with uniform thickness Schwarz-P

structure having the same relative density in Figure 80. The initial peak stress 1.6 MPa is the same for both structures, but the plateau shape of the uniform gradient structure has small undulations, and the ULC of the structure is less than that of the uniform thickness structure.

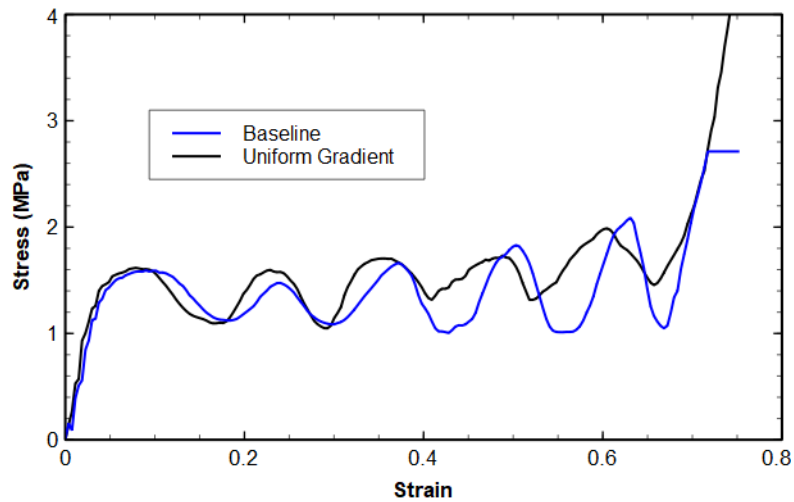


Figure 80. Stress-Strain curve for uniform gradient variable thickness Schwarz structure and comparison with the uniform thickness structure with same relative density.

Figure 81 shows the deformation pattern of the uniform gradient variable thickness Schwarz-P structure. The thickness of the structure governs the collapse pattern of the cell. As thickness is lowest in the bottom row, collapse initiates from the corner cells of the bottom row. An inverted ‘V-shaped’ collapse can be seen in the middle.

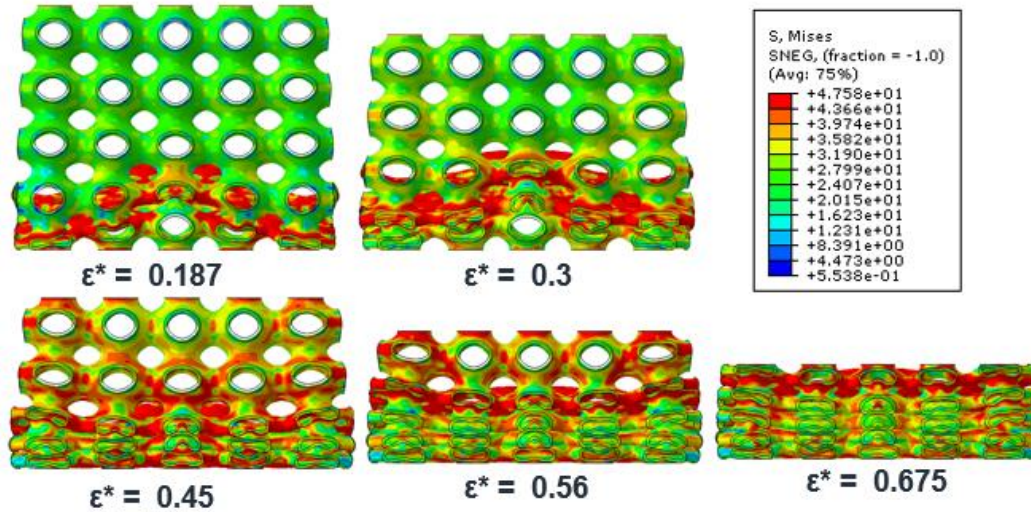


Figure 81. Deformation pattern of uniform gradient variable thickness structure under uniaxial compression load at the collapse of cell layers

The uniform gradient field improves the SEA of the Schwarz-P structure by 10 %, and thus validates the hypothesis, though the cause for this is attributed to the lower valleys attained for later row collapses. The first three rows collapse in a similar manner to that observed in the baseline structure, but the undulations observed in subsequent collapses are reduced relative to the baseline, thereby increasing the available area under the curve. This reduction in undulation at the later stages can be attributed to the fact that the top two rows that are the last to collapse have thicknesses higher than 0.5 mm, the fixed thickness in the baseline specimen.

Further improvements to the undulations of the plateau stress require an examination of its underlying causes. Each dip in the stress plateau corresponds to a sympathetic collapse of multiple cells – thus it is reasonable to hypothesize that a field that takes cell collapse into consideration is likely to improve performance by reducing

undulations. The uniform field, while an improvement over the baseline, does not incorporate any information from the physics of collapse. The simulation driven design, while being a far more physically relevant approach, is challenging to meaningfully implement when the field continuously evolves during the deformation process itself. As a result, the next field that was examined was one designed with the intent of nudging the localization of cell collapse in a favorable orientation.

#### 5.4.2 Shear Band Field

It is essential to weaken the cells methodically to change the collapse pattern.

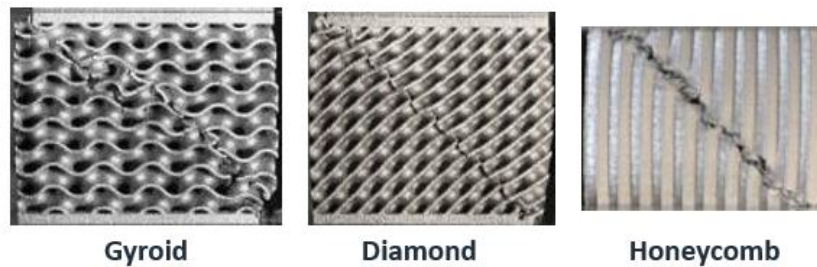


Figure 82. Shear band formation in the AlSi10Mg Gyroid, Diamond, and Honeycomb structures

A field inspired by the shear bands formed in the studied structures is used to improve energy absorption. The shear bands formed in the structures are shown in Figure 82. The hypothesis to test is if the collapse pattern is changed to occur along the diagonal and inclined hinges are introduced; the structure will have lower ULC and higher SEA.

The shear band field was created with a diagonal, auxiliary plane at an angle of  $45^{\circ}$  to the horizontal. A uniform gradient is applied with reference to the newly defined auxiliary plane, as explained previously in section 5.4.1 . Figure 83 shows the shear band

distribution of the thickness on the Schwarz-P structure. The blue colormap shows the thickness assigned to the point on the mid-surface. The thickness varies from 0.43 mm to 0.55 mm, so selected again to result in the same relative density as the baseline design with 0.5 mm thickness.

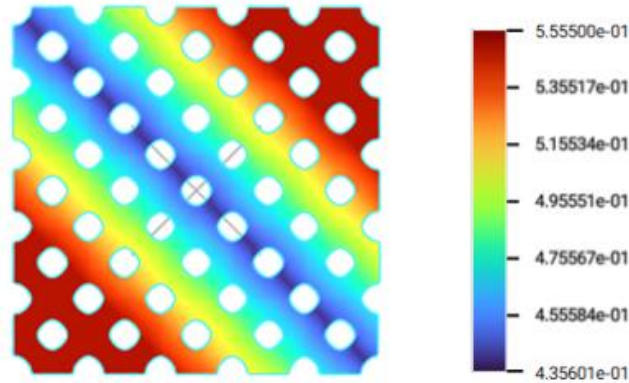


Figure 83. The overlay of Shear Band Field values varying from 0.43 mm to 0.56 mm in the Schwarz-P structure.

The FEA model was generated, and a uniaxial compression simulation is carried out to get a stress-strain curve for the variable thickness structure. Figure 84 shows the comparison of the stress-strain curves and cell collapse pattern in variable thickness structure and uniform thickness structure.



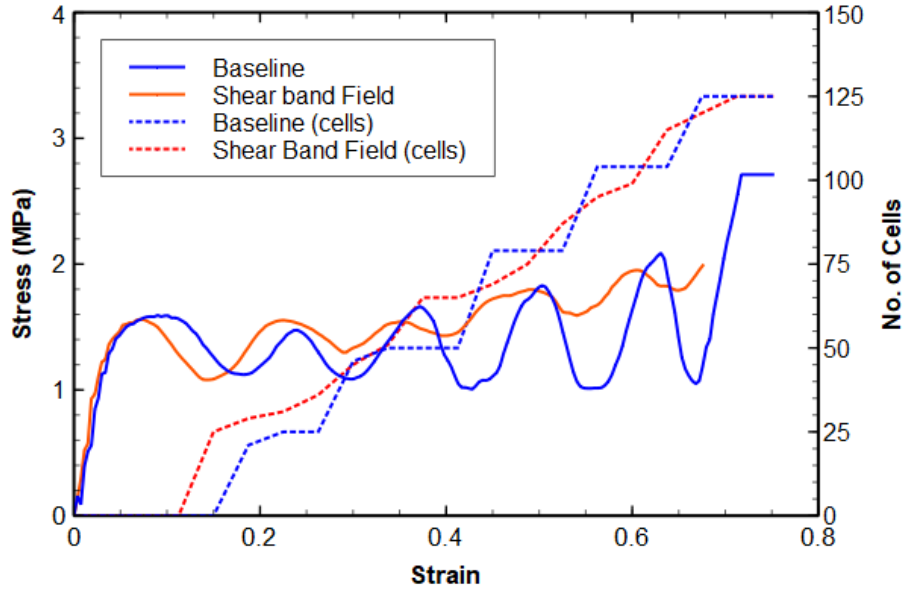


Figure 84. Stress-Strain curves and cell collapse count for shear band variable thickness Schwarz-P structure and comparison with the uniform thickness structure with same relative density.

The first drop after peak stress occurs early with the variable thickness design due to low thickness in the shear band. After the first drop, the undulations in the plateau region are lower, as indicated by ULC of 0.108 instead of ULC of 0.2 in uniform thickness structure, which represents a remarkable 50% reduction in ULC. The cell collapse is also tracked and plotted in Figure 84, showing a strong correlation between cell collapse and stress level drop in the stress-strain curve. In the uniform thickness structure, as a cell collapses, neighboring cells collapse sympathetically. In the variable thickness structure with a shear band after the first collapse, asymmetry is introduced in the structure. The deformed band has higher stiffness than the intact cells and can be considered rigid. This introduction of the rigid band at an angle of  $45^\circ$  changes the reaction forces on the remaining cells. This variable thickness also causes to form the of angular plastic hinges in the direction of the shear band, and cells collapse at an angle, as seen in Figure 85.

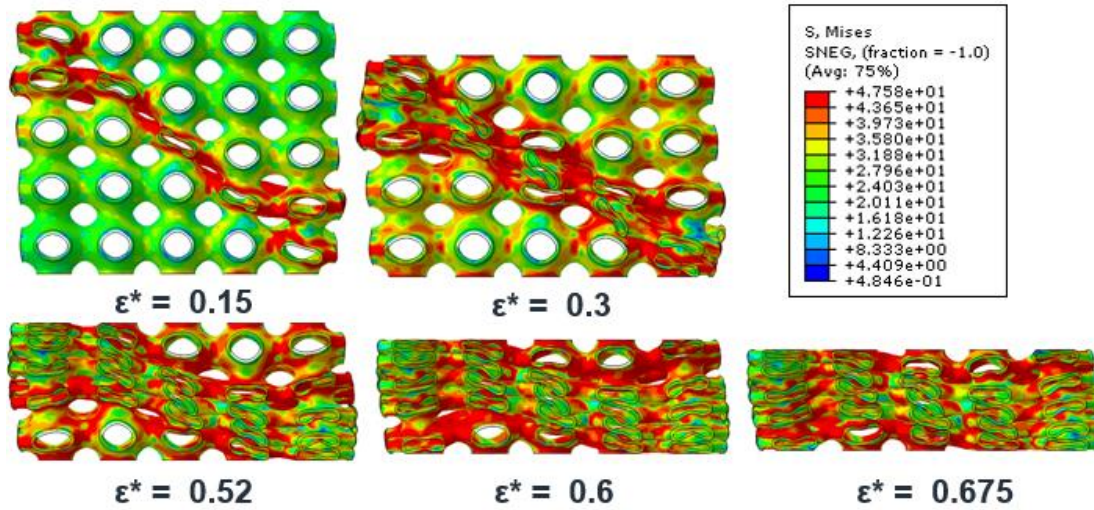


Figure 85. Deformation pattern of shear band variable thickness structure under uniaxial compression load at the collapse of cell layers

#### 5.4.3 Radial Field

While the diagonal field applied in the previous section showed significant reduction in undulations, it only modifies thickness along a single plane, with the third direction having identical thickness. It also reveals the importance of sympathetic collapse in influencing undulations in the stress plateau. A hypothesis may thus be proposed: reduction in the occurrence of sympathetic collapse – i.e., staggering collapse temporally, will result in lower undulations. And further, that a field that modifies thickness in all three directions is more likely to achieve this staggered collapse.

A straightforward to implement a geometric field that varies in all 3 directions is to use a spherical field. The equation gives the radial field for thickness  $t$  in mm,

$$t = 0.56 - r * 0.0025 \quad (17)$$

where,

$$r^2 = x^2 + y^2 + z^2 \quad (18)$$

The thickness distribution according to the radial field is depicted in Figure 86a. Figure 86b shows a cut section at the center of the structure. The thickness at the center is 0.56 mm, the maximum in the structure. Thickness decreases linearly with radius  $r$  and has a value of 0.46 mm at a distance of 40 mm. The hypothesis for using a radial field is by applying a gradient radially, and the deformation will happen in a diamond pattern around the central cell with maximum thickness, which will result in reduced undulations.

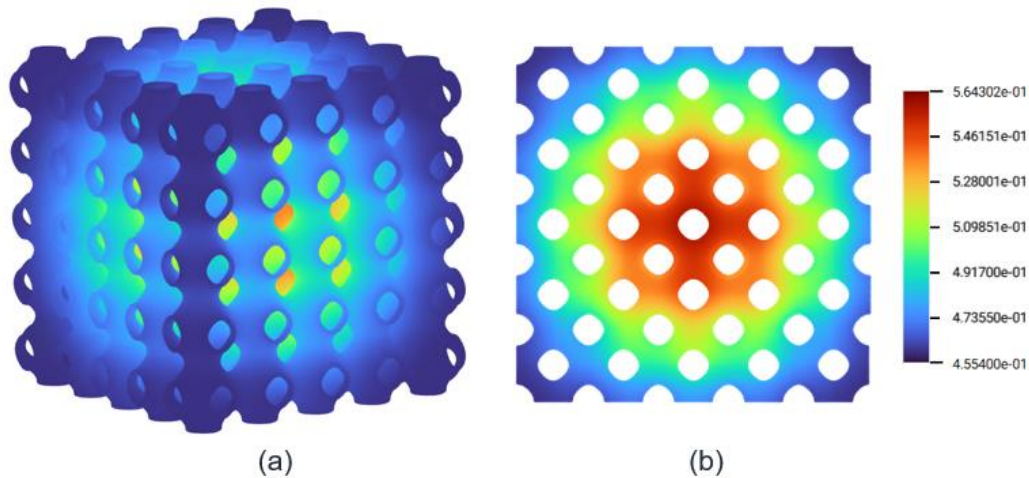


Figure 86. The overlay of Radial Field values varying from 0.44 mm to 0.56 mm and Schwarz-P structure.

Deformation patterns shown in Figure 87 illustrates behavior similar to the baseline geometry, in that sympathetic collapse still occurs following an “=” pattern. The first drop is delayed as compared to baseline due to the strong central cell. The thick cell acts as keystone and offers more resistance, Collapse starts from central row and layerwise sympathetic collapse is observed in each layer of the structure. The hypothesis is

invalidated as the deformation pattern remains same. The prime reason for the similar collapse pattern can be attributed to symmetry of the field.

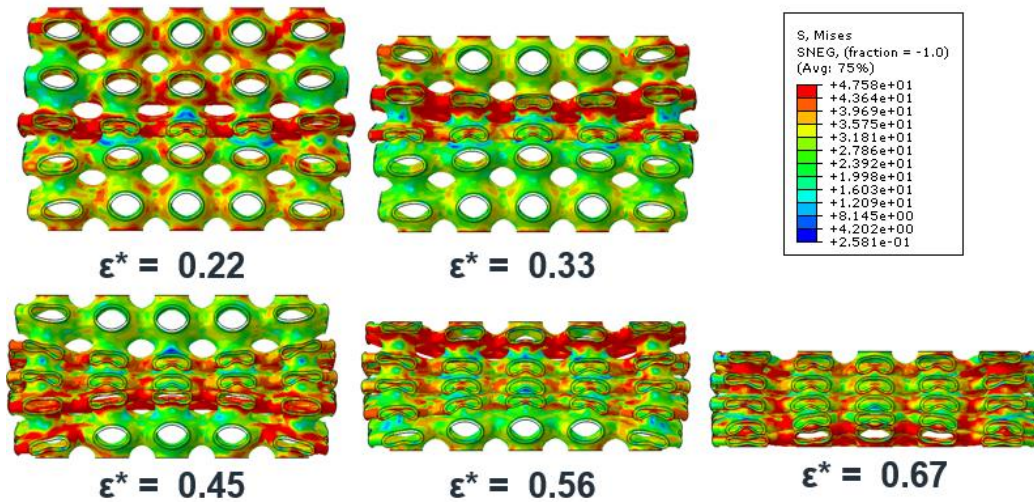


Figure 87. Deformation pattern of radial field variable thickness structure under uniaxial compression load at the collapse of cell layers

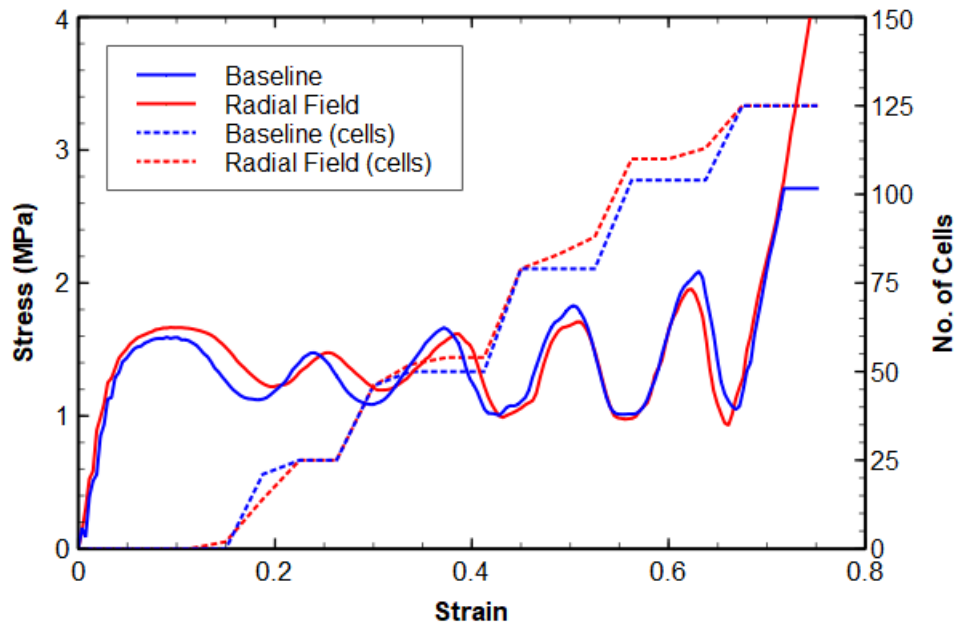


Figure 88. Stress-Strain curve comparison of spherical field and baseline uniform thickness structure

## 5.5. Stochastic Fields

As opposed to rational fields, stochastic fields are generated randomly, and any point in space can have a random value of thickness based on the coordinates. The hypothesis for using stochastic fields is that, due to random variation in the structure's thickness, each cell has unique stiffness introducing aperiodicity in the structure, causing it to deform asymmetrically under uniaxial compression giving smooth plateau and high SEA for the structure. Simplex noise and Cellular Noise fields are used in this study to generate stochastic fields.

### 5.5.1 Simplex Noise Field

A simplex algorithm uses a simplex shape to discretize the domain [88]. For example, to discretize the 2D domain, equilateral triangles are used. Each pixel is located in this grid, and gradients are associated with the grid points. A dot product of the gradient and distance vector gives the output value at each point. Simplex noise was created to overcome the shortcoming of well-known Perlin noise [92]. It uses a radial attenuation function to weigh each point; hence, no interpolation is required, generating high-quality noise [93]. Figure 89 shows the thickness distribution in the Schwarz-P structure generated using a simplex noise field. The thickness varies from 0.45mm to 0.55 mm, and the structure has the same relative density as the uniform thickness structure.

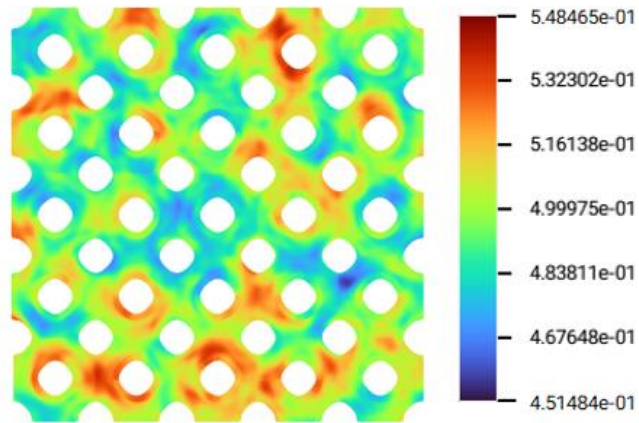


Figure 89. The overlay of Radial Field values varying from 0.44 mm to 0.56 mm and Schwarz-P structure.

The stress-strain curve compared with the baseline in Figure 91 shows that due to the introduction of noise in the structure, the first drop after the first peak is reduced by 18%, and energy absorption also increases by 6.33 %. The cells' failure pattern is gradual compared to stepwise collapse in the uniform thickness structure. The ULC is reduced by 38% as compared to the baseline structure. The hypothesis is validated, and it can be concluded that the aperiodic structure, due to the superimposition of simplex noise, field the collapse gradually and resulted in reduced undulations in the stress-strain curve, which results in an increase in the energy absorption.



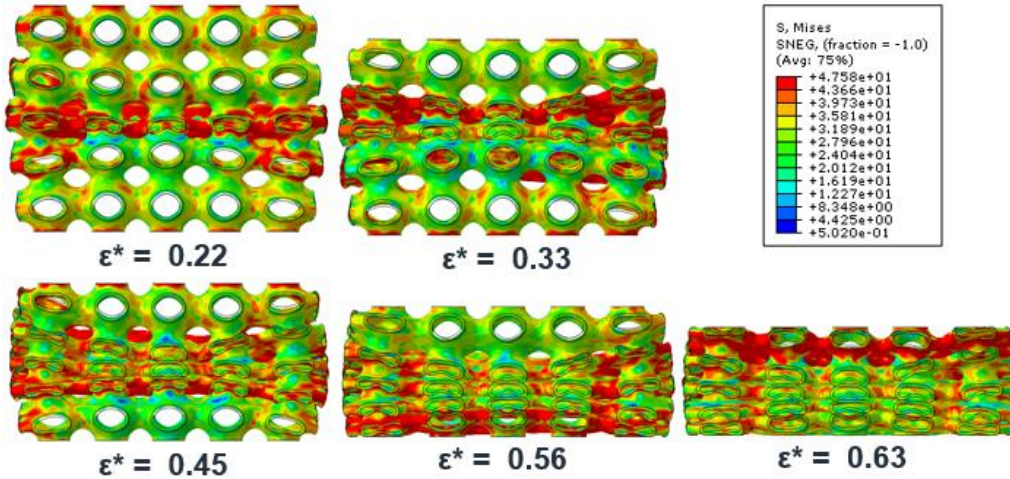


Figure 90. Deformation pattern of Simplex noise field variable thickness structure under uniaxial compression load at the collapse of cell layers

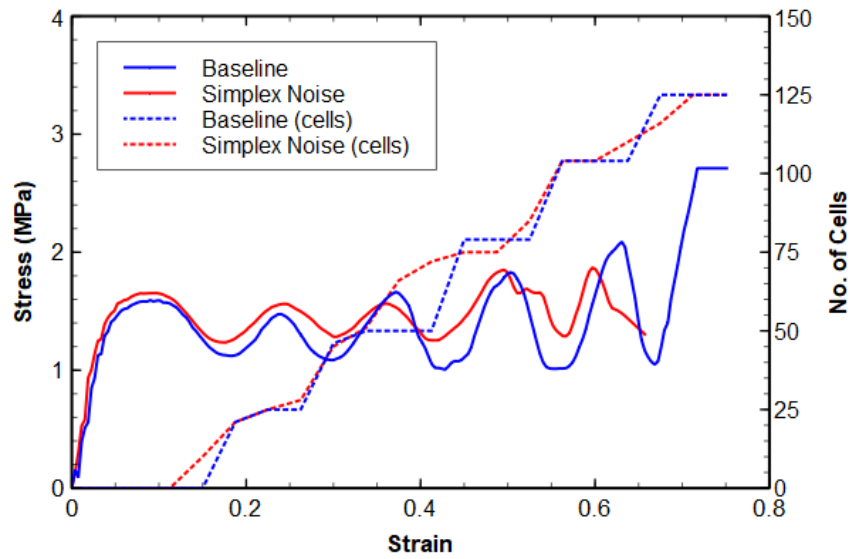


Figure 91. Stress-Strain curve comparison of Schwarz-P Simplex Noise Field and baseline uniform thickness structure

### 5.5.2 Cellular Noise Field

Random 3D Voronoi cells are generated based on cell noise or Whorley noise [85].

Few points are randomly scattered in space. The value of any given pixel is the distance of

the  $n$ th closest point [93]. Based on the choice of  $n$ , the cell noise is divided into Standard, Distance, Euclidean, and Manhattan subtypes [85]. For the current study the Distance field is used. The field generated by the cellular noise function is shown in Figure 92.

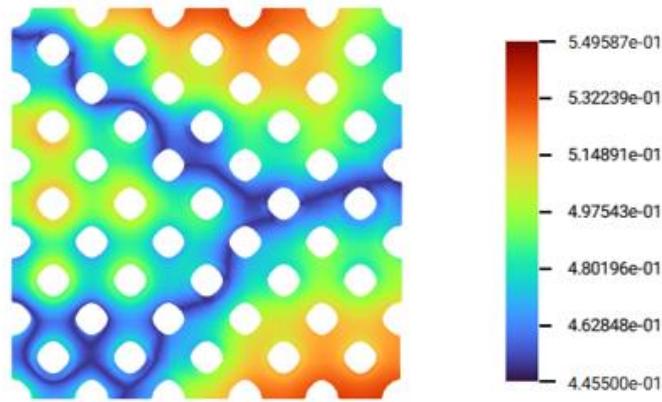


Figure 92. The overlay of Cellular Noise Field values varying from 0.43 mm to 0.56 mm and Schwarz-P structure.

The blue color indicates minimum thickness in the structure, and red color indicates maximum thickness distribution in the structure. The progressive deformation pattern is shown in Figure 93. The cells along the minimum thickness band collapse first; as the minimum thickness is lower than the baseline thickness, the collapse starts early as compared to the baseline structure. As the compressive strain increases, weaker cells amongst the remaining cell in the structure collapse. After second collapse due to aperiodicity introduced in the structure, simultaneous collapse of the cells occurs.



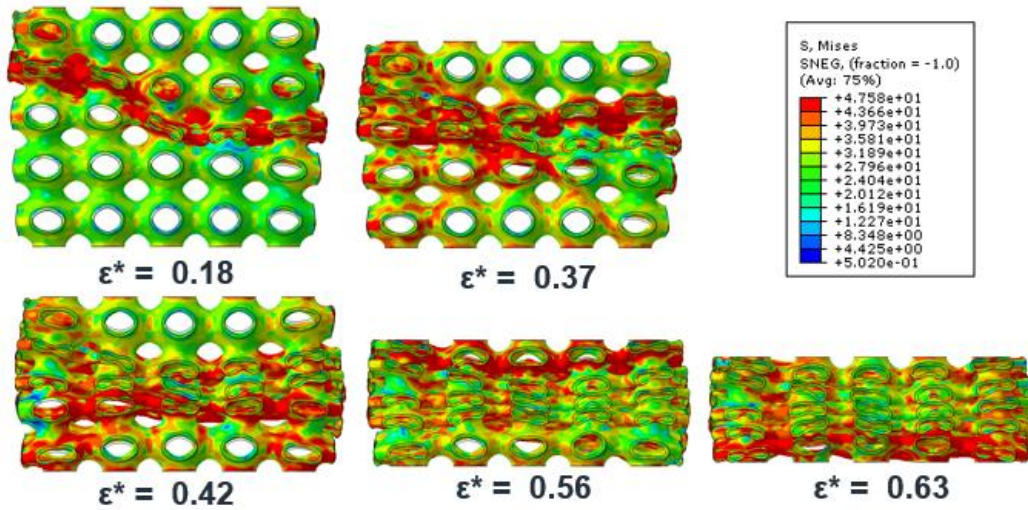


Figure 93. Deformation pattern of Cellular noise field variable thickness structure under uniaxial compression load at the collapse of cell layers

Figure 94 compares the stress-strain curve of variable thickness structure designed with cellular noise field and uniform thickness structure. The undulations in the cellular noise field structure are reduced as compared to the baseline structure.

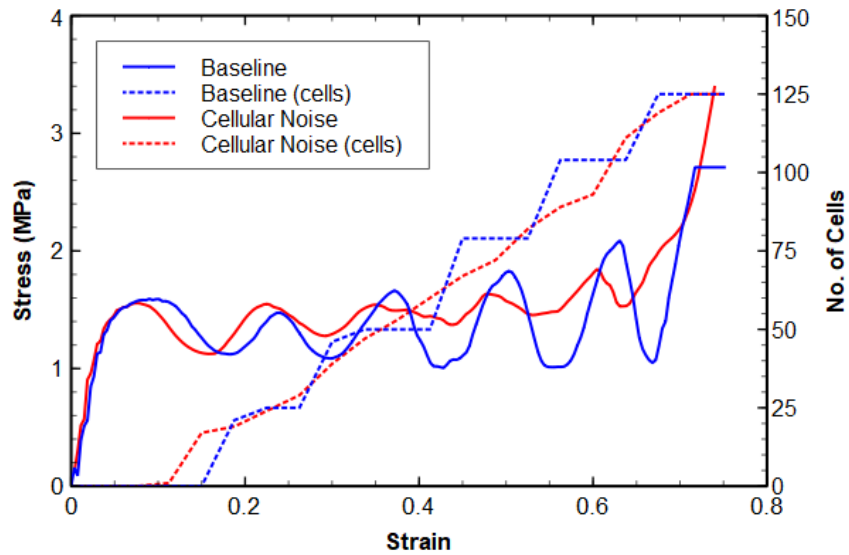


Figure 94. Stress-Strain curve comparison of Schwarz-P Cellular Noise Field and baseline uniform thickness structure

## 5.6. Conclusions

The numerical study of the field-driven design gives insight into how fields influence a cellular structure's energy absorption characteristics. Table 9 summarizes the energy absorption characteristics of all the structures studied in this chapter relative to the uniform thickness gradient; it shows that various fields can be used to improve the energy absorption ability of the structure, reduce the undulation coefficient, or reduce the first drop in the stress level of the structure.

Table 9. Comparison of energy absorption parameters for studied field-driven designs with uniform thickness structure.

Sr. No.	Field	OSD	First Drop [Mpa]	Energy Absorbed [J]	SEA[J /g]	ULC	Max. Transmitted Stress [MPa]	SEA/ MTS
1	Uniform Thickness	0.66	0.47	57.15	6.34	0.18	2.09	3.03
2	Uniform Gradient	0.65	0.52	61.40	6.81	0.14	1.99	3.42
3	Shear band	0.65	0.48	62.61	6.94	0.13	1.95	3.56
4	Radial	0.66	0.45	57.54	6.38	0.16	1.95	3.26
5	Simplex noise	0.65	0.42	60.77	6.74	0.11	1.87	3.60
6	Cell noise	0.63	0.43	57.69	6.40	0.10	1.84	3.47

The shear band field-driven structure shows the highest energy absorption capacity amongst the studied structures with 0.143 relative density, and a lower maximum transmitted stress. The cellular noise field-driven structure has the lowest ULC indicating the undulations are lowest due to the gradual collapse in the cells. The simplex noise field-driven structures show multiple advantages with increased SEA and very low ULC. The simulation-driven design using a plastic energy density field could not enhance the performance of the Schwarz-P structure. However, the methodology can be used with other fields to improvise of the uniform thickness structures.

## CHAPTER 6: SUMMARY AND FUTURE STUDY

This work concerned itself with exploring the four key contributing factors to energy absorption behavior. experimentally characterized the quasistatic compressive responses of six different cellular materials manufactured in AlSi10Mg, and Nylon-12 to enable comparisons among metrics of interest to the designer of energy absorption structures. The work also examined the effect of enclosing them in tubes. The primary conclusions and contributions of this experimental work are as follows:

- The 20  $\mu\text{m}$  layer thickness laser powder bed fusion process on a 100W laser machine generates lattice, honeycombs, and TPMS cellular structures with high fidelity, as evidenced by microscopy and the agreement between measured and nominally designed relative densities.
- A combination of four criteria may be used in determining the overall appropriateness of a cellular structure for implementation into an energy-absorbing system: (i) SEA vs. maximum transmitted stress; (ii) densification efficiency; (iii) plateau undulation; and (iv) tunability.
- Auxetic and Voronoi lattice structures perform poorly as energy absorbers primarily due to low SEA relative to maximum transmitted stresses and low densification efficiencies. Lattices are, however, highly tunable.
- TPMS structures, in particular the diamond and gyroid shapes, show great promise as energy absorption materials relative to honeycombs. This is primarily on account of their more gradual failure mechanism that includes folding and stacking of cell

walls above each other, resulting in higher densification densities and lower plateau undulations.

- Enclosing cellular structures in tubes has the effect of increasing peak stress while also increasing plateau stress undulations.
- A review of the literature of quasistatic energy absorption of additively manufactured cellular materials shows that a wide range of unit cells and materials are explored and characterized for energy absorption. It is observed that there is inconsistency in methods to determine the onset strain of densification.
- A new approach called the Hybrid Efficiency Method (HEM) was proposed, which is similar to MEM with the exception of (i) using peak stress instead of instantaneous stress to identify the efficiency maxima and (ii) identifying the local maxima on the instantaneous efficiency just prior to this point to establish OSD.
- The Max Transmitted stress/ Yield strength and SEA/ Yield strength are found to be material independent and can be used by the designers while designing energy-absorbing structures.

An effort is made to model and evaluate these structures numerically using FE method with shell elements. Chapters 4 and 5 discuss numerical work for evaluation of the effect of field-driven design in the energy absorbing structures following conclusions can be obtained by the study,

- The additively manufactured TPMS structures can be modeled by continuum shell elements with improved contact detection than conventional shell elements due to the ability to detect contact based on the element's geometry.

- The continuum shell elements can be stacked to improve the accuracy of the numerical solution.
- A methodology to model variable thickness TPMS structures with continuum shell elements is presented with a validation study.
- Chapter 5 shows improvement in the energy absorption parameters via a field-driven design approach using analytical and stochastic fields.

### 6.1.1 Future Work

This work can serve as the foundation for developing structures with improved energy absorption characteristics. In the current work, tools such as nTopology, Hypermesh, and Abaqus were used to design, model, and simulate the structure; an integrated tool can be imagined, implementing the current methodology to develop energy absorbers numerically according to design requirements. The fields studied in this work can be a good starting point for the optimization work. Apart from energy-absorbing structures, the developed method and script to generate variable thickness continuum shell elements can be used for general purposes to develop FEA models for thin structures.

This study was focused on developing energy-absorbing structures. The applications of energy absorbers include high-speed impact; hence this study needs to be validated at the high-speed impact. Future work includes exploring design parameters such as cell size, the structure's material, and fields.

The impact direction in practical applications, such as sports helmets or medical implants, is often unpredictable. The energy absorbers should be designed to give isotropic

energy absorption to account for the unpredictability of impact direction. In this study, the structures are characterized in only one direction. Future work includes characterizing structures in multiple directions and with variable loads to account for the unpredictability of the impact.

## REFERENCES

- [1] G. Y. Lu and Tongxi, *Energy Absorption of Materials and Structures*. 2003.
- [2] P. Astori, M. Zanella, and M. Bernardini, “Validation of numerical models of a rotorcraft crashworthy seat and subfloor,” *Aerospace*, vol. 7, no. 12, pp. 1–17, 2020.
- [3] M. F. Ashby, A. G. Evans, N. A. Fleck, L. J. Gibson, J. W. Hutchinson, and H. N. G. Wadley, *Metal Foams : A Design Guide*. Butterworth Heinemann, 2000.
- [4] G. Lu and T. X. Yu, *Energy Absorption of Structures and Materials*. 2003.
- [5] H. Yin, W. Zhang, L. Zhu, F. Meng, J. Liu, and G. Wen, “Review on lattice structures for energy absorption properties,” *Compos. Struct.*, vol. 304, no. P1, p. 116397, 2023.
- [6] I. E. Ramirez-Chavez, D. Anderson, R. Sharma, C. Lee, and D. Bhate, “A Classification of Aperiodic Architected Cellular Materials,” *Designs*, vol. 6, no. 4, p. 63, Jul. 2022.
- [7] L. Gibson and M. Ashby, “Cellular solids: structure and properties,” 1999.
- [8] L. Zhang *et al.*, “Energy absorption characteristics of metallic triply periodic minimal surface sheet structures under compressive loading,” *Addit. Manuf.*, vol. 23, no. July, pp. 505–515, 2018.
- [9] Y. Liang *et al.*, “Energy Absorption and Deformation Behavior of 3D Printed Triply Periodic Minimal Surface Stainless Steel Cellular Structures under Compression,” *Steel Res. Int.*, vol. 92, no. 3, pp. 1–9, 2021.
- [10] X. Liu, A. Suzuki, N. Takata, M. Kobashi, and M. Kato, “Dual plateau stress of C15-type topologically close-packed lattice structures additive-manufactured by laser powder bed fusion,” *Scr. Mater.*, vol. 202, p. 114003, 2021.

- [11] Y. Xiang, M. Wang, T. Yu, and L. Yang, “Key Performance Indicators of Tubes and Foam-Filled Tubes Used as Energy Absorbers,” vol. 7, no. 4, pp. 1–20, 2015.
- [12] I. Maskery, N. T. Aboulkhair, A. O. Aremu, C. J. Tuck, and I. A. Ashcroft, “Compressive failure modes and energy absorption in [1] I. Maskery, N. T. Aboulkhair, A. O. Aremu, C. J. Tuck, and I. A. Ashcroft, ‘Compressive failure modes and energy absorption in additively manufactured double gyroid lattices,’ *Addit. Manuf.*, vol. 16, ,” *Addit. Manuf.*, vol. 16, pp. 24–29, Aug. 2017.
- [13] Q. M. Li, I. Magkiriadis, and J. J. Harrigan, “Compressive strain at the onset of densification of cellular solids,” *J. Cell. Plast.*, vol. 42, no. 5, pp. 371–392, 2006.
- [14] J. A. Harris and G. J. McShane, “Metallic stacked origami cellular materials: Additive manufacturing, properties, and modelling,” *Int. J. Solids Struct.*, vol. 185–186, pp. 448–466, 2020.
- [15] Z. Ma, D. Z. Zhang, F. Liu, J. Jiang, M. Zhao, and T. Zhang, “Lattice structures of Cu-Cr-Zr copper alloy by selective laser melting: Microstructures, mechanical properties and energy absorption,” *Mater. Des.*, vol. 187, p. 108406, 2020.
- [16] L. Zhang *et al.*, “Energy absorption characteristics of metallic triply periodic minimal surface sheet structures under compressive loading,” *Addit. Manuf.*, vol. 23, pp. 505–515, Oct. 2018.
- [17] J. A. Harris, R. E. Winter, and G. J. McShane, “Impact response of additively manufactured metallic hybrid lattice materials,” *Int. J. Impact Eng.*, vol. 104, pp. 177–191, 2017.
- [18] Y. Liu, T. A. Schaedler, A. J. Jacobsen, and X. Chen, “Quasi-static energy absorption of hollow microlattice structures,” *Compos. Part B Eng.*, vol. 67, pp. 39–49, 2014.
- [19] T. A. Schaedler *et al.*, “Designing Metallic Microlattices for Energy Absorber Applications,” no. 3, pp. 276–283, 2014.
- [20] M. F. Ashby, A. G. Evans, N. A. Fleck, L. J. Gibson, J. W. Hutchinson, and H. N. G. Wadley, *Metal Foams: A Design Guide*. Butterworth Heinemann, 2010.



- [21] F. S. L. Bobbert *et al.*, “Additively manufactured metallic porous biomaterials based on minimal surfaces: A unique combination of topological, mechanical, and mass transport properties,” *Acta Biomater.*, vol. 53, pp. 572–584, Apr. 2017.
- [22] V. S. Deshpande, M. F. Ashby, and N. A. Fleck, “Foam topology: Bending versus stretching dominated architectures,” *Acta Mater.*, vol. 49, no. 6, pp. 1035–1040, 2001.
- [23] L. R. Meza, A. J. Zelhofer, N. Clarke, A. J. Mateos, D. M. Kochmann, and J. R. Greer, “Resilient 3D hierarchical architected metamaterials,” *Proc. Natl. Acad. Sci.*, vol. 112, no. 37, pp. 11502–11507, 2015.
- [24] N. Kladovasilakis, K. Tsongas, and D. Tzetzis, “Mechanical and fea-assisted characterization of fused filament fabricated triply periodic minimal surface structures,” *J. Compos. Sci.*, vol. 5, no. 2, 2021.
- [25] R. Gümrük and R. A. W. Mines, “Compressive behaviour of stainless steel micro-lattice structures,” *Int. J. Mech. Sci.*, vol. 68, pp. 125–139, 2013.
- [26] I. Maskery *et al.*, “A mechanical property evaluation of graded density Al-Si10-Mg lattice structures manufactured by selective laser melting,” *Mater. Sci. Eng. A*, vol. 670, pp. 264–274, 2016.
- [27] M. Smith *et al.*, “The quasi-static and blast response of steel lattice structures,” *J. Sandw. Struct. Mater.*, vol. 13, no. 4, pp. 479–501, 2011.
- [28] Z. Ozdemir, A. Tyas, R. Goodall, and H. Askes, “Energy absorption in lattice structures in dynamics: Nonlinear FE simulations,” *Int. J. Impact Eng.*, 2017.
- [29] T. A. Schaedler *et al.*, “Designing Metallic Microlattices for Energy Absorber Applications \*\*,” no. 3, pp. 276–283, 2014.
- [30] I. Maskery, N. T. Aboulkhair, A. O. Aremu, C. J. Tuck, and I. A. Ashcroft, “Compressive failure modes and energy absorption in additively manufactured double gyroid lattices,” *Addit. Manuf.*, vol. 16, pp. 24–29, 2017.
- [31] C. Yan, L. Hao, A. Hussein, S. L. Bubb, P. Young, and D. Rayment, “Evaluation of

light-weight AlSi10Mg periodic cellular lattice structures fabricated via direct metal laser sintering,” *J. Mater. Process. Technol.*, vol. 214, no. 4, pp. 856–864, 2014.

- [32] Y. Du *et al.*, “Laser additive manufacturing of bio-inspired lattice structure: Forming quality, microstructure and energy absorption behavior,” *Mater. Sci. Eng. A*, vol. 773, no. December 2019, p. 138857, 2020.
- [33] H. Jia *et al.*, “An experimental and numerical investigation of compressive response of designed Schwarz Primitive triply periodic minimal surface with non-uniform shell thickness,” *Extrem. Mech. Lett.*, vol. 37, p. 100671, 2020.
- [34] T. Tancogne-Dejean, A. B. Spierings, and D. Mohr, “Additively-manufactured metallic micro-lattice materials for high specific energy absorption under static and dynamic loading,” *Acta Mater.*, vol. 116, pp. 14–28, 2016.
- [35] O. Al-Ketan, R. Rezgui, R. Rowshan, H. Du, N. X. Fang, and R. K. Abu Al-Rub, “Microarchitected Stretching-Dominated Mechanical Metamaterials with Minimal Surface Topologies,” *Adv. Eng. Mater.*, vol. 20, no. 9, pp. 1–15, 2018.
- [36] L. Yang, C. Yan, C. Han, P. Chen, S. Yang, and Y. Shi, “Mechanical response of a triply periodic minimal surface cellular structures manufactured by selective laser melting,” *Int. J. Mech. Sci.*, vol. 148, pp. 149–157, Nov. 2018.
- [37] E. W. Andrews, G. Gioux, P. Onck, and L. J. Gibson, “Size effects in ductile cellular solids. Part II: Experimental results,” *Int. J. Mech. Sci.*, vol. 43, no. 3, pp. 701–713, 2001.
- [38] C. Tekoğlu, L. J. Gibson, T. Pardoen, and P. R. Onck, “Size effects in foams: Experiments and modeling,” *Prog. Mater. Sci.*, vol. 56, no. 2, pp. 109–138, 2011.
- [39] J. Zhang, G. Lu, and Z. You, “Large deformation and energy absorption of additively manufactured auxetic materials and structures : A review,” *Compos. Part B*, vol. 201, no. July, p. 108340, 2020.
- [40] NTopology, “Platform.” New York, 2020.
- [41] ASTM F3302, “Standard for Additive Manufacturing – Finished Part Properties –

Standard Specification for Titanium Alloys via Powder Bed Fusion,” *ASTM Stand.*, vol. i, no. February, pp. 1–8, 2018.

- [42] “AMS2774E - IN718 Heat Treatment (SAE Standard).”
- [43] T. A. Schaedler *et al.*, “Designing metallic microlattices for energy absorber applications,” *Adv. Eng. Mater.*, 2014.
- [44] L. Casanova *et al.*, “On the Mechanical Behavior of Additively Manufactured Asymmetric Honeycombs,” in *Solid Freeform Fabrication*, 2018.
- [45] Y. Liu, T. A. Schaedler, and X. Chen, “Dynamic energy absorption characteristics of hollow microlattice structures,” *Mech. Mater.*, 2014.
- [46] F. N. Habib, P. Iovenitti, S. H. Masood, and M. Nikzad, “Fabrication of polymeric lattice structures for optimum energy absorption using Multi Jet Fusion technology,” *Mater. Des.*, vol. 155, pp. 86–98, 2018.
- [47] Y. Tao *et al.*, “Mechanical properties and energy absorption of 3D printed square hierarchical honeycombs under in-plane axial compression,” *Compos. Part B Eng.*, vol. 176, no. June, p. 107219, 2019.
- [48] J. Plocher and A. Panesar, “Mechanical Performance of Additively Manufactured Fiber-Reinforced Functionally Graded Lattices,” *Jom*, vol. 72, no. 3, pp. 1292–1298, 2020.
- [49] X. Li, L. Xiao, and W. Song, “Compressive behavior of selective laser melting printed Gyroid structures under dynamic loading,” *Addit. Manuf.*, vol. 46, no. April, p. 102054, 2021.
- [50] M. Zhao, B. Ji, D. Z. Zhang, H. Li, and H. Zhou, “Design and mechanical performances of a novel functionally graded sheet-based lattice structure,” *Addit. Manuf.*, vol. 52, no. January, p. 102676, 2022.
- [51] Z. Ozdemir *et al.*, “Energy absorption in lattice structures in dynamics: Experiments,” *Int. J. Impact Eng.*, vol. 89, pp. 49–61, 2016.

- [52] N. Novak *et al.*, “Quasi-static and dynamic compressive behaviour of sheet TPMS cellular structures,” vol. 266, no. March, pp. 1–10, 2021.
- [53] Y. Liang *et al.*, “Energy Absorption and Deformation Behavior of 3D Printed Triply Periodic Minimal Surface Stainless Steel Cellular Structures under Compression,” vol. 2000411, pp. 1–9, 2021.
- [54] A. M. Abou-ali, O. Al-ketan, D. Lee, R. Rowshan, and R. K. A. Al-rub, “Mechanical behavior of polymeric selective laser sintered ligament and sheet based lattices of triply periodic minimal surface architectures,” *Mater. Des.*, vol. 196, p. 109100, 2020.
- [55] I. Maskery *et al.*, “An investigation into reinforced and functionally graded lattice structures,” *J. Cell. Plast.*, vol. 53, no. 2, pp. 151–165, 2017.
- [56] S. Kumar, J. Ubaid, R. Abishera, A. Schi, and V. S. Deshpande, “Tunable Energy Absorption Characteristics of Architected Honeycombs Enabled via Additive Manufacturing,” 2019.
- [57] O. Al-Ketan, D. W. Lee, and R. K. Abu Al-Rub, “Mechanical properties of additively-manufactured sheet-based gyroidal stochastic cellular materials,” *Addit. Manuf.*, vol. 48, Dec. 2021.
- [58] S. Morphology, C. Behavior, and B. Fusion, “Absorption of Graded Triply Periodic Minimal Surface 316L Steel Cellular Structures Fabricated by Laser Powder,” 2022.
- [59] Y. Wang *et al.*, “Cell-size graded sandwich enhances additive manufacturing fidelity and energy absorption,” *Int. J. Mech. Sci.*, vol. 211, no. August, p. 106798, 2021.
- [60] L. Bai *et al.*, “Mechanical properties and energy absorption capabilities of functionally graded lattice structures: Experiments and simulations,” *Int. J. Mech. Sci.*, vol. 182, no. February, p. 105735, 2020.
- [61] Y. Wang *et al.*, “Numerical and experimental studies on compressive behavior of Gyroid lattice cylindrical shells,” *Mater. Des.*, vol. 186, p. 108340, 2020.

- [62] D. W. Abueidda, M. Elhebeary, C. S. (Andrew) Shiang, S. Pang, R. K. Abu Al-Rub, and I. M. Jasiuk, "Mechanical properties of 3D printed polymeric Gyroid cellular structures: Experimental and finite element study," *Mater. Des.*, vol. 165, p. 107597, 2019.
- [63] X. Cao, D. Zhang, B. Liao, S. Fang, L. Liu, and R. Gao, "Thin-Walled Structures Numerical analysis of the mechanical behavior and energy absorption of a novel P-lattice," *Thin-Walled Struct.*, vol. 157, no. September, p. 107147, 2020.
- [64] M. Zhong, W. Zhou, H. Xi, Y. Liang, and Z. Wu, "Double-level energy absorption of 3d printed tpms cellular structures via wall thickness gradient design," *Materials (Basel)*, vol. 14, no. 21, Nov. 2021.
- [65] Y. Xu, T. Li, X. Cao, Y. Tan, and P. Luo, "Compressive Properties of 316L Stainless Steel Topology-Optimized Lattice Structures Fabricated by Selective Laser Melting," *Adv. Eng. Mater.*, vol. 23, no. 3, 2021.
- [66] C. Zhang *et al.*, "Mechanical responses of sheet-based gyroid-type triply periodic minimal surface lattice structures fabricated using selective laser melting," *Mater. Des.*, vol. 214, p. 110407, 2022.
- [67] X. Fan *et al.*, "International Journal of Mechanical Sciences Design , mechanical properties and energy absorption capability of graded-thickness triply periodic minimal surface structures fabricated by selective laser melting," *Int. J. Mech. Sci.*, vol. 204, no. May, p. 106586, 2021.
- [68] X. Liu, T. Wada, A. Suzuki, N. Takata, M. Kobashi, and M. Kato, "Understanding and suppressing shear band formation in strut-based lattice structures manufactured by laser powder bed fusion," *Mater. Des.*, vol. 199, p. 109416, 2021.
- [69] Q. Sun, J. Sun, K. Guo, and L. Wang, "Compressive mechanical properties and energy absorption characteristics of SLM fabricated Ti6Al4V triply periodic minimal surface cellular structures," *Mech. Mater.*, vol. 166, no. January, p. 104241, 2022.
- [70] D. Li, W. Liao, N. Dai, and Y. M. Xie, "Comparison of mechanical properties and energy absorption of sheet-based and strut-based gyroid cellular structures with graded densities," *Materials (Basel)*, vol. 12, no. 13, 2019.

- [71] S. Cui *et al.*, “Mechanical metamaterials foams with tunable negative poisson’s ratio for enhanced energy absorption and damage resistance,” *Materials (Basel)*., vol. 11, no. 10, 2018.
- [72] J. J. Andrew, J. Schneider, J. Ubaid, R. Velmurugan, N. K. Gupta, and S. Kumar, “Energy absorption characteristics of additively manufactured plate-lattices under low- velocity impact loading,” *Int. J. Impact Eng.*, vol. 149, no. August 2020, p. 103768, 2021.
- [73] J. Fu, P. Sun, Y. Du, H. Li, X. Zhou, and Q. Tian, “Isotropic design and mechanical characterization of TPMS-based hollow cellular structures,” *Compos. Struct.*, vol. 279, no. October 2021, p. 114818, 2022.
- [74] R. Sankineni and Y. Ravi Kumar, “Evaluation of energy absorption capabilities and mechanical properties in FDM printed PLA TPMS structures,” *Proc. Inst. Mech. Eng. Part C J. Mech. Eng. Sci.*, vol. 236, no. 7, pp. 3558–3577, 2022.
- [75] M. Tavares, J. M. Weigand, L. C. M. Vieira, S. J. C. Almeida, and S. Szyniszewski, “Mechanical behavior of steel and aluminum foams at elevated temperatures. Local buckling based approach toward understanding of the material system behavior,” *Int. J. Mech. Sci.*, vol. 181, no. May, 2020.
- [76] ISO, *ISO 13314: Mechanical testing of metals, ductility testing, compression test for porous and cellular metals*. 2011.
- [77] P. J. Tan, S. R. Reid, J. J. Harrigan, Z. Zou, and S. Li, “Dynamic compressive strength properties of aluminium foams. Part i - Experimental data and observations,” *J. Mech. Phys. Solids*, vol. 53, no. 10, pp. 2174–2205, 2005.
- [78] M. Shinde, I. Ramirez-Chavez, D. Anderson, J. Fait, M. Jarrett, and D. Bhate, “Towards an Ideal Energy Absorber: Relating Failure Mechanisms and Energy Absorption Metrics in Additively Manufactured AlSi10Mg Cellular Structures under Quasistatic Compression,” *J. Manuf. Mater. Process.*, vol. 6, no. 6, p. 140, 2022.
- [79] ASTM International, *Standard test method for tensile properties of plastics*. pp. 1–17.

- [80] D. Chapelle, K.-J. Bath, and C. Meyer, *The Finite Element Analysis of Shells: Fundamentals*, vol. 57, no. 3. 2004.
- [81] U. Simsek, A. Akbulut, C. E. Gayir, C. Basaran, and P. Sendur, “Modal characterization of additively manufactured TPMS structures: comparison between different modeling methods,” *Int. J. Adv. Manuf. Technol.*, vol. 115, no. 3, pp. 657–674, 2021.
- [82] M. Smith, “ABAQUS/Standard User’s Manual, Version 6.9 .” Dassault Systèmes Simulia Corp , Providence, RI , 2009.
- [83] C. Majewski and N. Hopkinson, “Effect of section thickness and build orientation on tensile properties and material characteristics of laser sintered nylon-12 parts,” *Rapid Prototyp. J.*, vol. 17, no. 3, pp. 176–180, 2011.
- [84] D. I. Stoia, E. Linul, and L. Marsavina, “Influence of manufacturing parameters on mechanical properties of porous materials by selective laser sintering,” *Materials (Basel)*, vol. 16, no. 6, 2019.
- [85] H. E. Demirci, S. Bhattacharya, N. A. Alexander, and R. M. Singh, “Finite Element Model of Buried Pipelines Crossing Strike-Slip Faults by ABAQUS / EXPLICIT This conference paper was accepted and will be published in the Proceedings of 16 th European Conference on Earthquake Engineering , 18-21 June 2018 , Thessaloniki .,” no. April, 2018.
- [86] C. Yang and Q. M. Li, “Advanced lattice material with high energy absorption based on topology optimisation,” *Mech. Mater.*, vol. 148, no. April, 2020.
- [87] J. Wu, N. Aage, and O. Sigmund, “Infill Optimization for Additive Manufacturing – Approaching Bone-like Porous Structures,” pp. 1–14.
- [88] L. Wang, S. Tao, P. Zhu, and W. Chen, “Data-driven topology optimization with multiclass microstructures using latent variable Gaussian process,” *J. Mech. Des. Trans. ASME*, vol. 143, no. 3, 2021.
- [89] G. X. Gu, C.-T. Chen, D. J. Richmond, and M. J. Buehler, “Bioinspired hierarchical composite design using machine learning: simulation, additive manufacturing, and experiment †,” 2018.

- [90] M. J. Mirzaali, H. Pahlavani, and A. A. Zadpoor, “Auxeticity and stiffness of random networks: Lessons for the rational design of 3D printed mechanical metamaterials,” *Appl. Phys. Lett.*, vol. 115, p. 21901, 2019.
- [91] L. Bai, C. Yi, X. Chen, Y. Sun, and J. Zhang, “Effective design of the graded strut of BCC lattice structure for improving mechanical properties,” *Materials (Basel)*, vol. 12, no. 13, 2019.
- [92] I. McEwan, D. Sheets, M. Richardson, and S. Gustavson, “Efficient Computational Noise in GLSL,” *J. Graph. Tools*, vol. 16, no. 2, pp. 85–94, Jun. 2012.
- [93] T. Archer, “Procedurally Generating Terrain,” *44th Annu. midwest Instr. Comput. Symp. Duluth*, pp. 378–393, 2011.



APPENDIX A  
MATLAB CODE INFORMATION

The MATLAB code requires two .csv files given in supplement S4 as input files. This code takes the Force-displacement data and specimen bounding box data and gives energy absorption parameters including OSD, ULC, Plateau stress, SEA as output. The Hybrid Efficiency Method explained in the paper is used to determine the OSD. The explanation of code is added as comments in the code itself this section is used to highlight important functions.

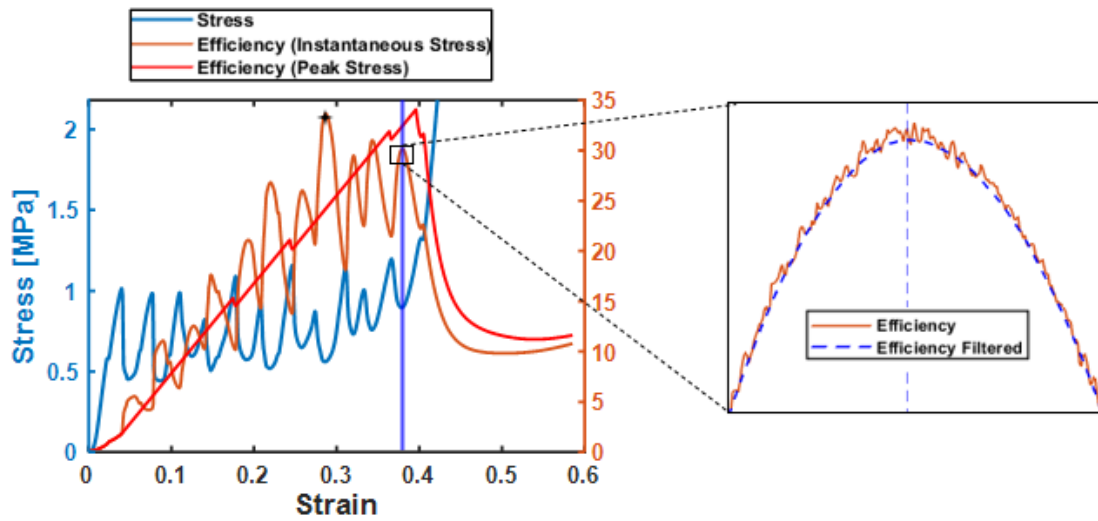


Figure S2.1 Stress Strain curve of Auxetic structure 0.5 mm beam thickness (b) Deformed structure at OSD. *findpeaks()* and *max()* functions are used to find the appropriate maxima depending on the method used, and then used to establish OSD.

### Code

```

clc;
clear all;
%TITLE
%NEEDED RESULT VALUES:
%=====
====
%specimen parameter input
%=====
=====

```

```

base="Auxetic_0.75";
filename=convertStringsToChars(append(base ,'.csv'));
specimen_no=19;
mult_factor=2;
threshold_0 = 0.002;
peakbracket = [0,.2];
bracket_linear = [0.001 0.0055]; %this is the x range of where the linear
%elastic region is located
%=====
====
Es=55180; % (MPa)
yield= 137.38; % (MPa)
filename_1='Specimen_names.csv';
%=====
====
%acquire data from the .csv file
%=====
====
spec_data=readmatrix(filename_1);
xwidth = spec_data(specimen_no,3); % Width of the cellular structure
ythickness = spec_data(specimen_no,4); % Length of the cellular structure
zheight = spec_data(specimen_no,5); % Height of the cellular structure
mass=spec_data(specimen_no,6); % Mass of the cellular structure
Area = xwidth*ythickness; % Area of the cellular structure
Volume = zheight*Area; % Volume of the cellular structure
basename = filename(1:end-4);
force_disp = readmatrix(filename);
force_column = 3;
disp_column = 2;
X = force_disp(:,disp_column); % (kN) extract displacement data
Y = force_disp(:,force_column); % (kN) extract force data
%=====
====
%crop out data below threshold_0
%=====
====
start_cutoff = 0;
j = 1;
while j<length(Y)
    if Y(j)>threshold_0
        start_cutoff = j;
        j = length(Y);
    end
    j = j + 1;
end
X = X(start_cutoff:length(X))-X(start_cutoff);
Y = Y(start_cutoff:length(Y));
%=====
====
%calculate Stress and Strain
%=====
====
stress = force2stress(Y,Area)*1000;% Units(MPa) Calculate stress
strain = disp2strain(X,zheight); % Calculate strain

```

```

%=====
====
%create array of Peak Stress till current point
%=====
====
n=numel(stress); % Number of array elements
maxstress=zeros(n,1); % Create a zero matrix of length n
for j=1:1:n-1
    maxstress(1)=stress(1);
    if stress(j+1)>=maxstress(j)
        maxstress(j+1)=stress(j+1);
    else
        maxstress(j+1)=maxstress(j);
    end
end
end
%=====
====
%calculate energy absorbed curve and efficiency curve
% units for Eabs_vol are N/mm^2
%=====
====
[Efficiency,Eabs] = energyEfficiency(X,Y);
[Efficiency_vol,Eabs_vol] = energyEfficiency(strain, stress);
[Efficiency_max,Eabs_max] = energyEfficiency(strain,maxstress);
[limit_eff, limit_index]=max(Efficiency_max)
Eabs_m = Eabs/mass ;% units (J/g)
%=====
====
%Find max of the energy efficiency curve and it's index
%=====
====
[Eff_Max,densif_index] = max(Efficiency);
smooth_eff=sgolayfilt(Efficiency, 1, 51);
[pks,locs] = findpeaks(smooth_eff);
[global_max,I]=max(pks);
densif_index=locs(I);
%temp_max_index=maxInRange(strain, stress, 1,I)
temp_max_stress=max(stress(1:densif_index));
len=length(locs);
global_max_index=locs(I);
mod_densif_index=global_max_index;
for j=I:1:len
    curr_index=locs(j);
    if curr_index <= limit_index+50
        densif_index=curr_index
    end
end
end
Strain_dense = strain(densif_index);
%densif_index = global_max_index
%find first peak stress
stress_eff=max(stress(1:global_max_index));
stress_mod=max(stress(1:densif_index));
maxindex = maxInRange(strain, stress, peakbracket(1), peakbracket(2));
peakstrain = strain(maxindex);

```

```

peakstress = stress(maxindex);
minindex
minInRange(strain, stress, peakstrain, peakbracket(2)*mult_factor);
valleystrain = strain(minindex);
valleystress = stress(minindex);
%=====
====
%find total energy absorbed until densification
%=====
====
Eabs_d = Eabs(densif_index);
Eabs_d_vol = Eabs_vol(densif_index);
%=====
====
%find slope of the linear region using the linear bracket values
%=====
====
V = fitWithinRange(strain, stress, bracket_linear(1), bracket_linear(2));
slope = V(1);
intercept = V(2);
x1 = bracket_linear(1);
y1 = bracket_linear(1)*slope + intercept;
x2 = bracket_linear(2);
y2 = bracket_linear(2)*slope + intercept;
linfit = [x1 y1 ; x2 y2]; %linear fit points for plotting later
%=====
====
%find plateau stress
%=====
====
plat_avg = mean(stress(maxindex:densif_index));
%=====
====
%find the smoothed stress data and then find the first peak of the averaged
%data
%=====
====
Navg = 200;
stress_avg = movmean(stress, Navg);
Y_avg = movmean(Y, Navg);
x1='Displacement (mm)';
y1='Force (kN)';
densification_displacement = X(densif_index);
Eabs_max=peakstress*Area*densification_displacement;
Eff= Eabs_d/Eabs_max*100;

Max_trans_stress=peakstress;

MCF=Eabs_d/densification_displacement; % calculate mean crushing force as
%energy absorbed till densification divided by densification stroke.

Y_diff=abs(Y-MCF); %

```

```

Y_diff=Y_diff(1:densif_index);
X_diff=X(1:densif_index);
ULC=trapz(X_diff,Y_diff)/Eabs_d;
SEA_vol= Eabs_d_vol ;
max_eff_strain=strain(global_max_index);
%*****
****
%=====plotting section to check
values=====
%*****
****
close all
p=figure;
hold on
%title('Stress vs Strain','FontSize', 13);
ylim([0 2*peakstress])
yyaxis left
plot(strain, stress, 'LineWidth',1.5);
xlabel('Strain', 'FontWeight', 'bold', 'FontSize', 12);
ylabel('Stress [MPa]', 'FontWeight', 'bold', 'FontSize', 12);
yyaxis right;
plot(strain, Efficiency_vol*100, '-b', 'LineWidth',1.3)
plot(strain, Efficiency_max*100, '-r', 'LineWidth',1.3)
xline(max_eff_strain, '--
b', 'LineWidth',1.5)%, {'Densification'}, 'FontSize', 12);
xline(Strain_dense, '--
r', 'LineWidth',1.5)%, {'Densification'}, 'FontSize', 12);
box on
x0=10;
y0=10;
width=350;
height=250;
set(gcf, 'position', [x0,y0,width,height]);
set(gca, 'FontName', 'Arial', 'fontweight', 'bold');
ax=gca;
ax.LineWidth = 1.25;
pname=[basename, '_Stress_strain.emf'];
exportgraphics(p,pname)

%=====end plotting section=====
%SSvalues = [stress strain];

function[stressout] = force2stress(Y,area)
%Y: values for force
%Area: cross-sectional area of the specimen as viewed from above
stressout = Y./area;
end
function[strainout] = disp2strain(X,height)
%converts displacement to strain
strainout = X./height;
end

function[N,Energy] = energyEfficiency(Xin,Stress_in)

```

```

%takes in stress-strain values and outputs the energy absorption
efficiency
%for each data point. Also outputs a matrix which contains the amount of
%energy absorbed up to that point

```

```

N = zeros(length(Stress_in),1);
Energy = zeros(length(Stress_in),1);
temparea = 0;
    for i=2:length(Stress_in)
        dx = Xin(i)-Xin(i-1);
        recarea = dx*Stress_in(i-1);
        temparea = recarea + temparea;
        N(i) = temparea/Stress_in(i);
        Energy(i) = temparea;
    end
end

```

```

function [Maxinds,Mininds,Rmax,Rmin] =
significantMaxMin(Xin,Yin,Navg,buffer);
%takes in Y values and number of averaging points, then averages the curve
%to find the significant max and mins of the curve (ignoring the tiny
%bumps). Since the averaged max and mins are going to be a little bit off
%from the real max and mins, a buffer zone is used to capture the true
%peaks. The buffer should be relatively small but not so small that it
%gives inaccurate results. Rmax and Rmin contain the X and Y values of
all
%the max and mins.

```

```

Yavg = movmean(Yin,Navg); %smooth the curve out
TFmax = islocalmax(Yavg); %find local max indices
TFmin = islocalmin(Yavg); %find local min indices
maxsum = sum(TFmax);
minsum = sum(TFmin);

```

```

maxinds = zeros(maxsum,1);
mininds = zeros(minsum,1);
count = 1;

```

```

    for i=1:maxsum
        if TFmax(i)
            x1 = Xin - buffer;
            x2 = Xin + buffer;
            maxinds(count) = maxInRange(Xin,Yin,x1,x2);
            count = count + 1;
        end
    end
end

```

```

function [maxindex] = maxInRange(X,Y,Xstart,Xstop)
%input arguments
%    example    input:    [Xmax,Ymax,maximum_index_out]    =
maxInRange(X,Y,Xstop,Xstart);
% Max will be found between Xstart and Xstop values, anything outside of

```

```

% that range will be ignored.
i = 1;
startind = 0;
stopind = 0;
while i<length(X)
    if X(i)>Xstart
        startind = i-1;
        i = length(X);
    end
    i = i+1;
end
i = 1;
while i<length(X)
    if X(i)>Xstop
        stopind = i;
        i = length(X);
    end
    i = i + 1;
end
[Ymax,Yindex_max] = max(Y(startind:stopind));
maxindex = startind + Yindex_max;

end
function [minindex] = minInRange (X,Y,Xstart,Xstop)
Y = Y*(-1);


```



```

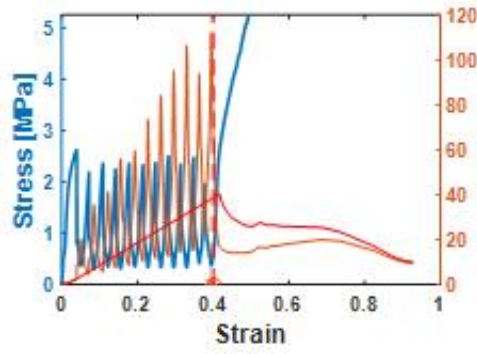
%takes in a matrix and a range where you'd like to perform a linear fit,
%cuts the data and returns the slope and y intercept of the linear fit
line
Xstart;
Xstop;
startindex = 0;
stopindex = 0;
j =1;
while j<length(Xin)
    if Xin(j)>Xstart
        startindex = j;
        j= length(Xin);
    end
    j = j + 1;
end
j = 1;
while j<length(Xin)
    if Xin(j)>Xstop
        disp('stop index found')
        stopindex = j;
        j = length(Xin);
    end
    j = j + 1;
end
startindex;
stopindex;
Xcut = Xin(startindex:stopindex);
Ycut = Yin(startindex:stopindex);
V = polyfit(Xcut,Ycut,1);

end

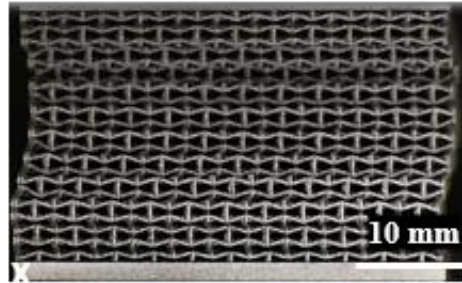
```

APPENDIX B

ONSET STRAIN OF DENSIFICATION

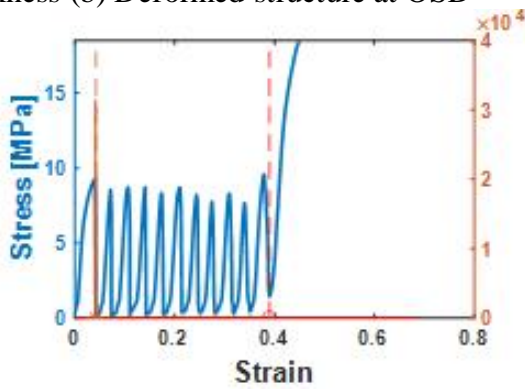


(a)

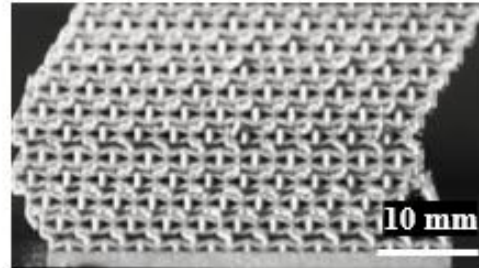


(b)

Figure S1.1 (a) Stress Strain curve of AlSi10Mg Auxetic structure with 0.5 mm beam thickness (b) Deformed structure at OSD

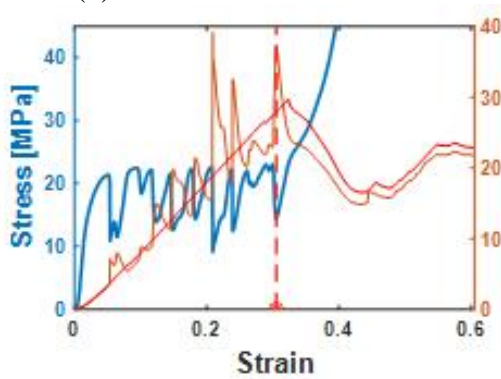


(a)

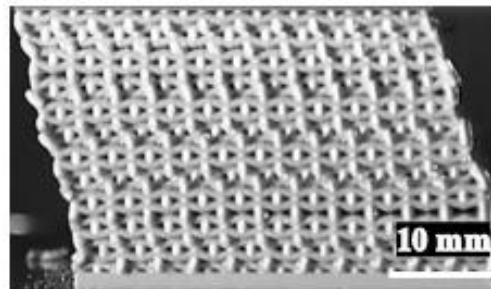


(b)

Figure S1.2 (a) Stress Strain curve of AlSi10Mg Auxetic structure 0.75 mm beam thickness (b) Deformed structure at OSD

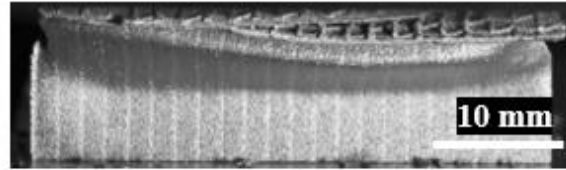
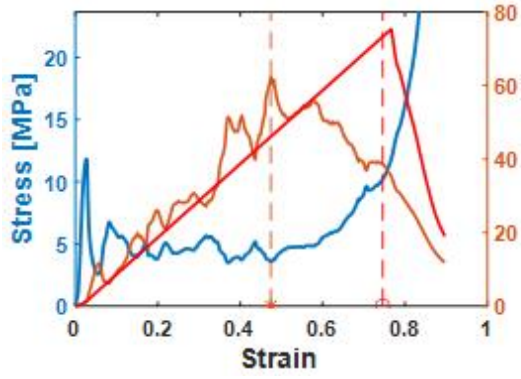


(a)



(b)

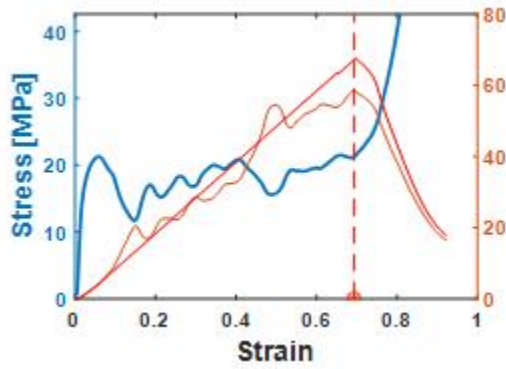
Figure S1.3 (a) Stress Strain curve of AlSi10Mg Auxetic structure 1 mm beam thickness (b) Deformed structure at OSD



(a)

(b)

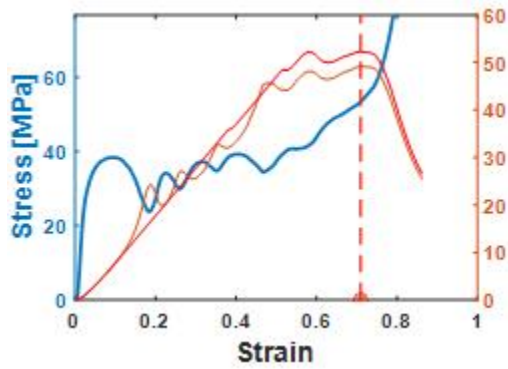
Figure S1.4 (a) Stress Strain curve of AlSi10Mg Auxetic structure with Tube (b) Deformed structure at OSD



(a)

(b)

Figure S1.5 (a) Stress Strain curve of AlSi10Mg Diamond structure 0.4 mm wall thickness (b) Deformed structure at OSD

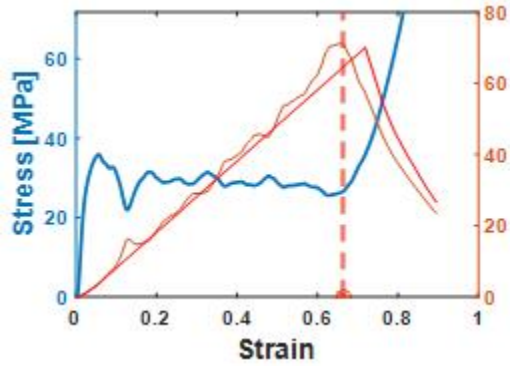


(a)

(b)

Figure S1.6 (a) Stress Strain curve of AlSi10Mg Diamond structure 0.6 mm wall thickness

(b) Deformed structure at OSD

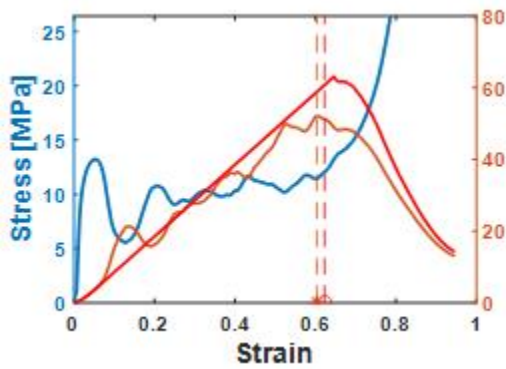


(a)

(b)

Figure S1.8 (a) Stress Strain curve of AlSi10Mg Diamond with tube structure 0.6 mm wall thickness

(b) Deformed structure at OSD

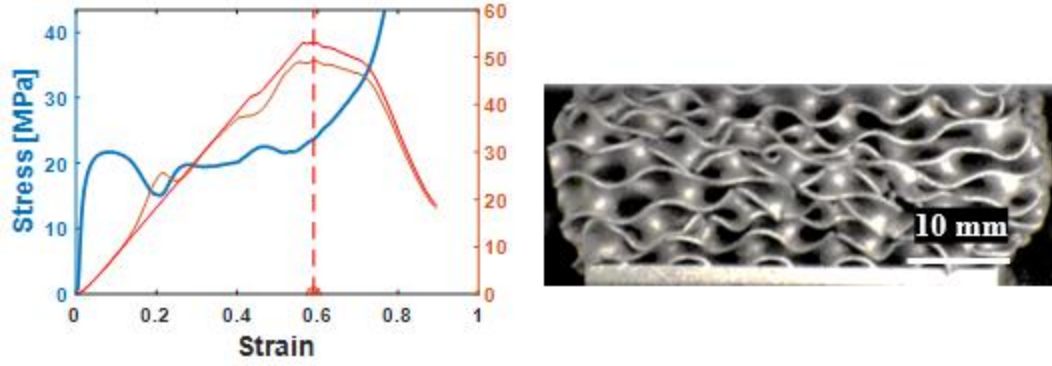


(a)

(b)

Figure S1.9 (a) Stress Strain curve of AlSi10Mg Gyroid structure 0.4 mm wall thickness

(b) Deformed structure at OSD

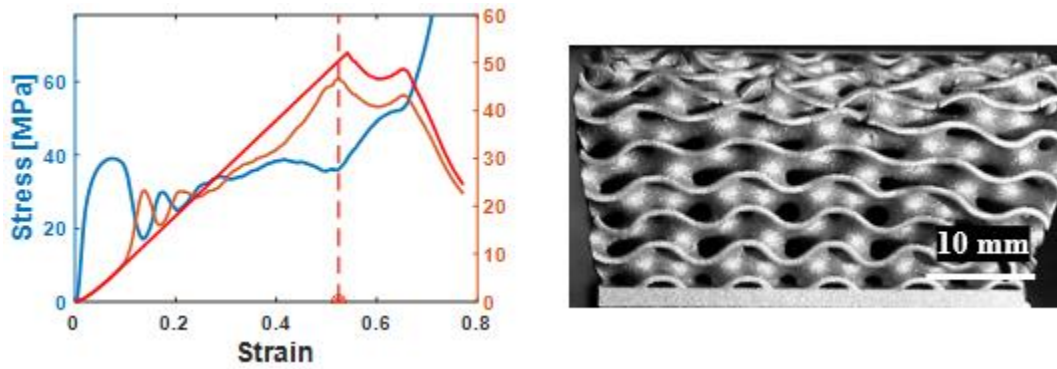


(a)

(b)

Figure S1.10 (a) Stress Strain curve of AlSi10Mg Gyroid structure 0.6 mm wall thickness

(b) Deformed structure at OSD

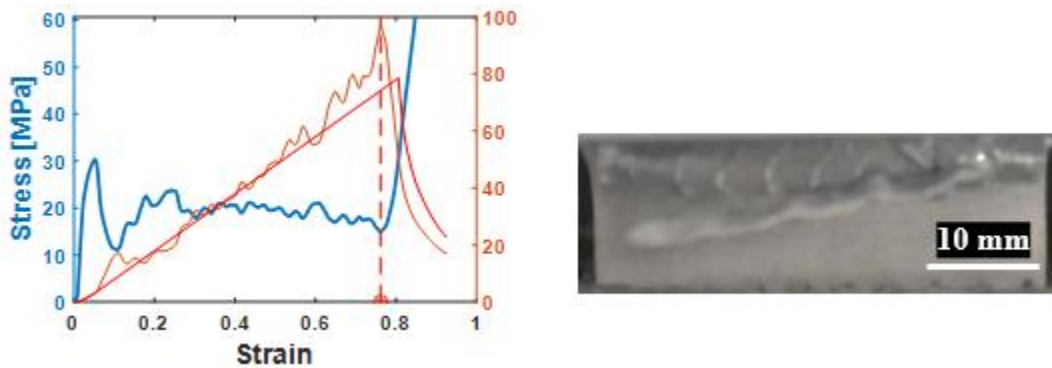


(a)

(b)

Figure S1.11 (a) Stress Strain curve of AlSi10Mg Gyroid structure 0.6 mm wall thickness

(b) Deformed structure at OSD



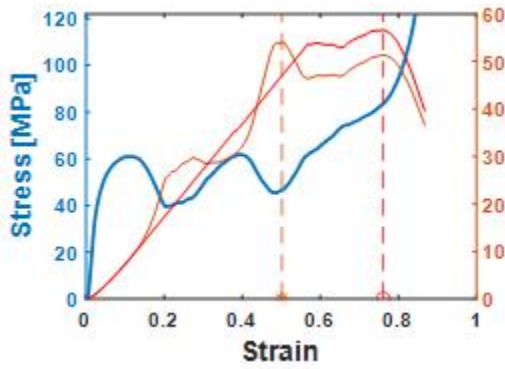
(a)

(b)



Figure S1.12 (a) Stress Strain curve of AlSi10Mg Gyroid structure 0.6 mm wall thickness

(b) Deformed structure at OSD

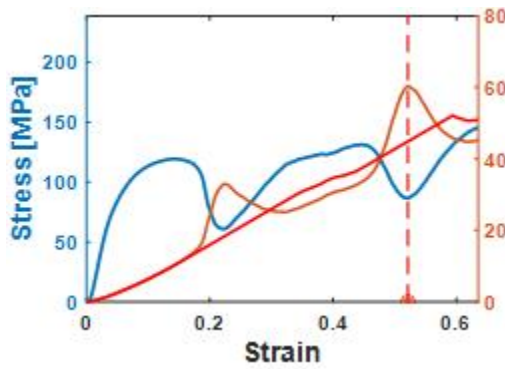


(a)

(b)

Figure S1.13 (a) Stress Strain curve of AlSi10Mg Honeycomb structure 0.4 mm wall

thickness (b) Deformed structure at OSD

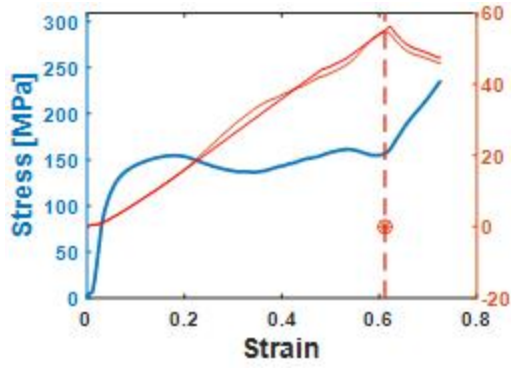


(a)

(b)

Figure S1.14 (a) Stress Strain curve of AlSi10Mg Honeycomb structure 0.6 mm wall

thickness (b) Deformed structure at OSD



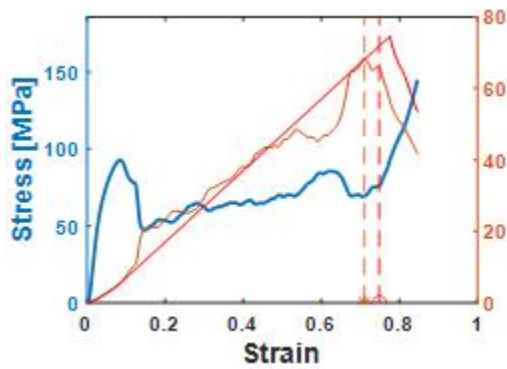
(a)



(b)

Figure S1.15 (a) Stress Strain curve of Honeycomb structure 0.8 mm wall thickness (b)

Deformed structure at OSD

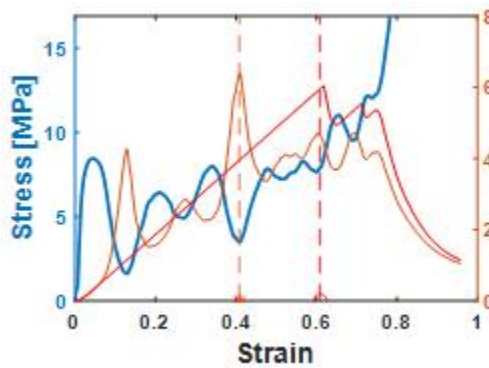


(a)



(b)

Figure S1.16 (a) Stress Strain curve of AlSi10Mg Honeycomb with tube structure 0.8 mm wall thickness (b) Deformed structure at OSD



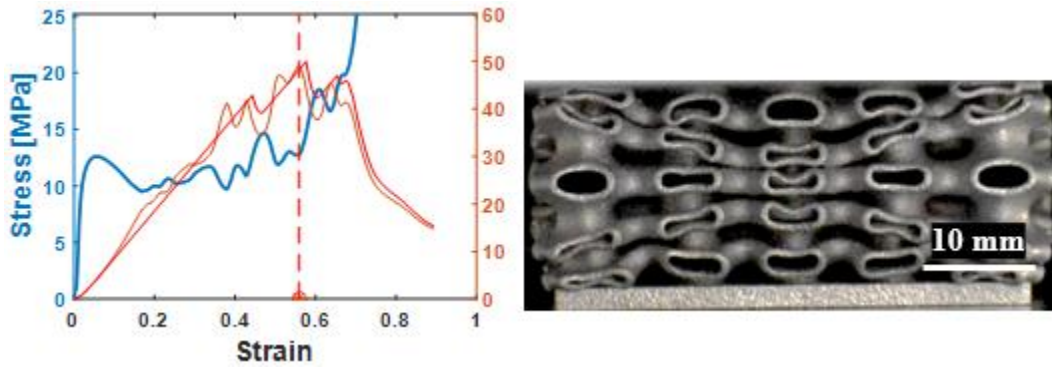
(a)



(b)



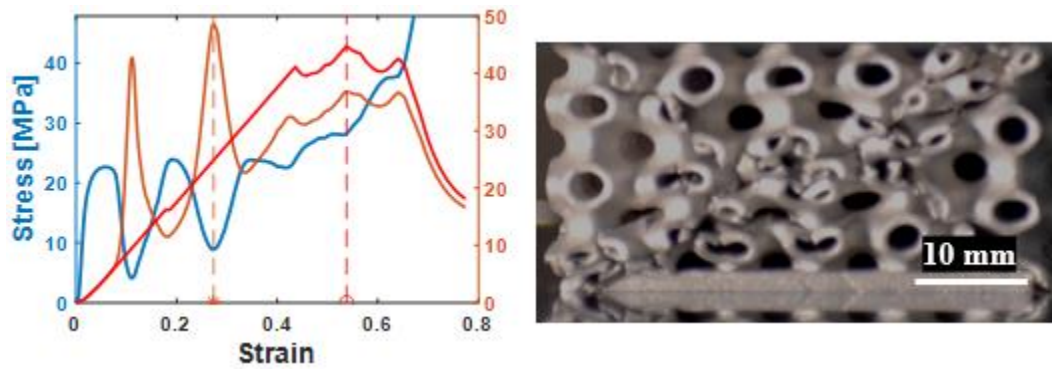
Figure S1.17 (a) Stress Strain curve of AlSi10Mg Schwarz-Primitive structure 0.4 mm wall thickness (b) Deformed structure at OSD



(a)

(b)

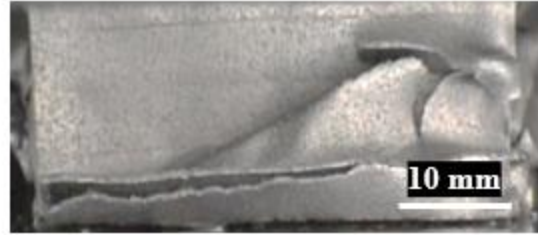
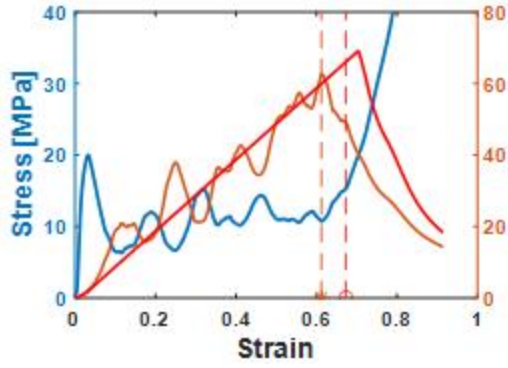
Figure S1.18 (a) Stress Strain curve of AlSi10Mg Schwarz-Primitive structure 0.6 mm wall thickness (b) Deformed structure at OSD



(a)

(b)

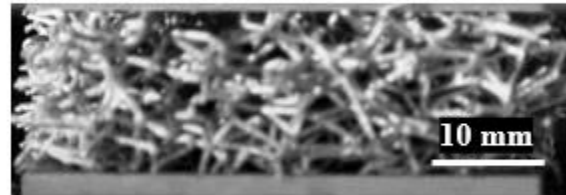
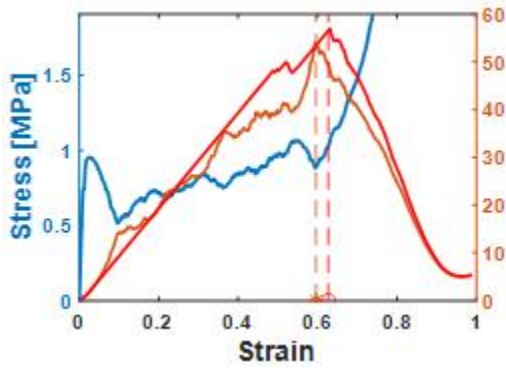
Figure S1.19 (a) Stress Strain curve of AlSi10Mg Schwarz-Primitive structure 0.8 mm wall thickness (b) Deformed structure at OSD



(a)

(b)

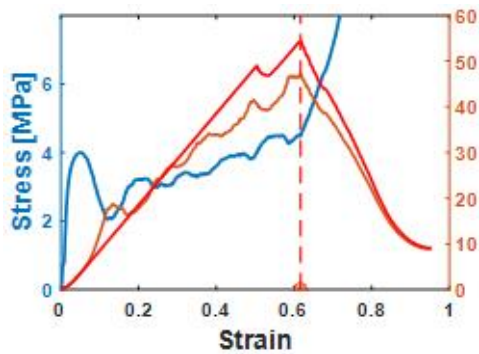
Figure S1.20 (a) Stress Strain curve of AlSi10Mg Schwarz-Primitive with tube structure 0.8 mm wall thickness (b) Deformed structure at OSD



(a)

(b)

Figure S1.21 (a) Stress Strain curve of AlSi10Mg Voronoi structure 0.8 mm wall thickness (b) Deformed structure at OSD.

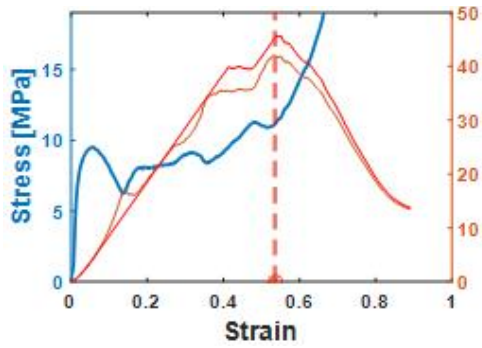


(a)

(b)

Figure S1.22 (a) Stress Strain curve of AlSi10Mg Voronoi structure 0.8 mm wall thickness

(b) Deformed structure at OSD.

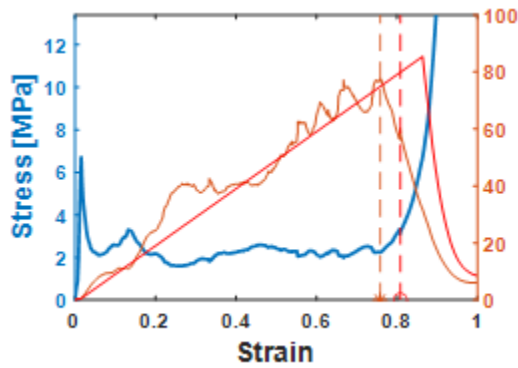


(a)

(b)

Figure S1.23 (a) Stress Strain curve of AlSi10Mg Voronoi structure 0.8 mm wall thickness

(b) Deformed structure at OSD



(a)

(b)

Figure S1.24 (a) Stress Strain curve of AlSi10Mg Voronoi structure with Tube (b)

Deformed structure at OSD.

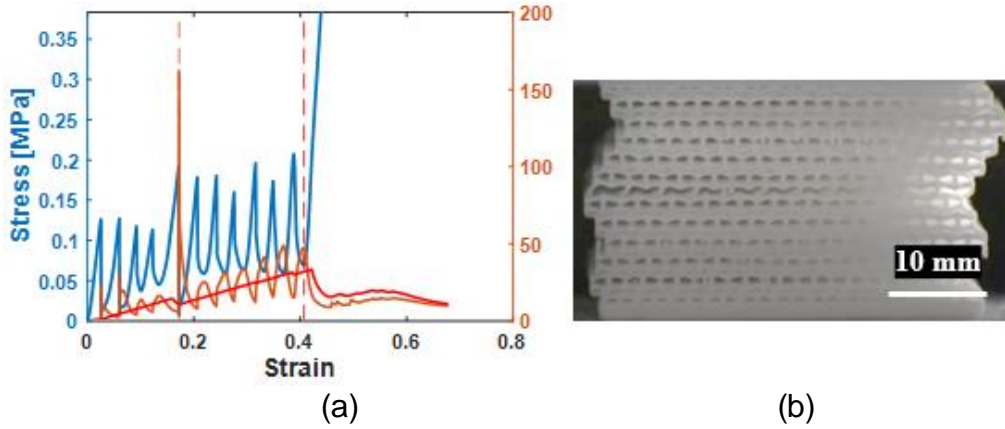


Figure S1.25 (a) Stress Strain curve of Nylon-12 Voronoi structure 0.5 mm wall thickness  
 (b) Deformed structure at OSD.

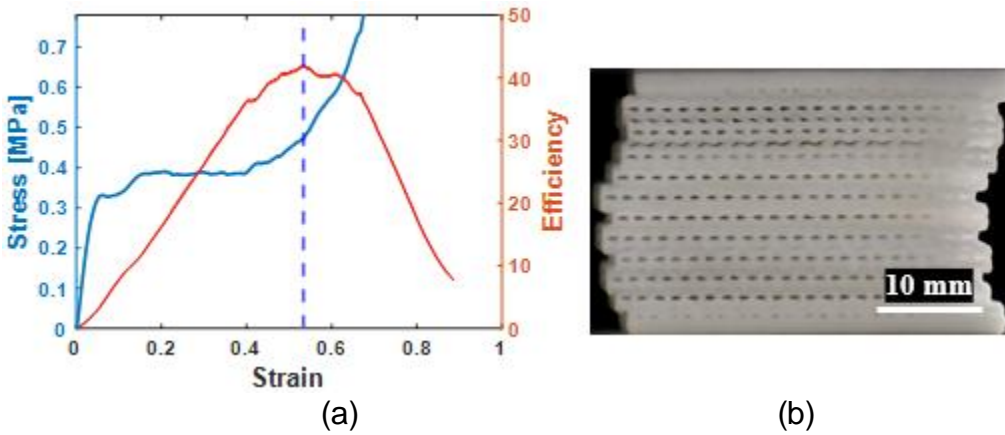


Figure S1.26 (a) Stress Strain curve of Nylon-12 Auxetic Structure 0.75 mm beam diameter  
 (b) Deformed structure at OSD.

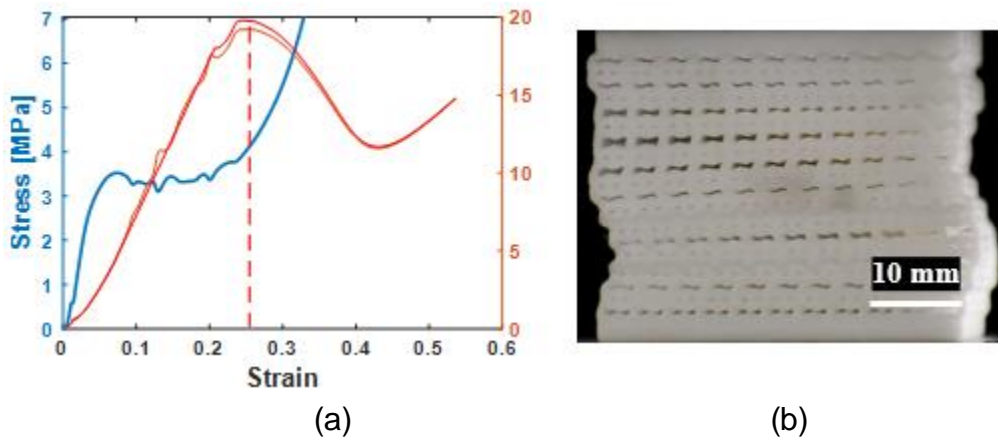
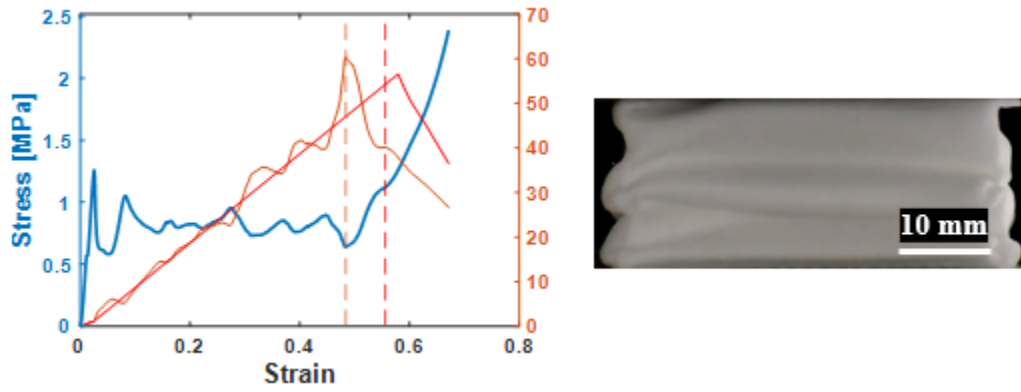


Figure S1.27 (a) Stress Strain curve of Nylon-12 Auxetic Structure 1 mm beam diameter

(b) Deformed structure at OSD.

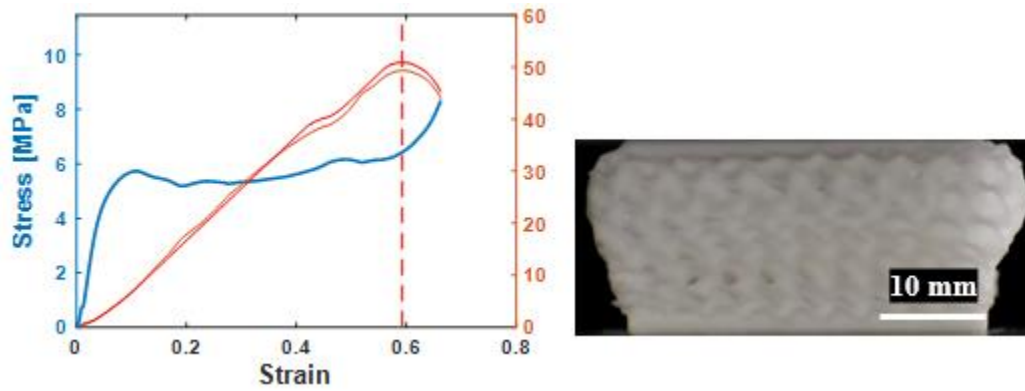


(a)

(b)

Figure S1.28 (a) Stress Strain curve of Nylon-12 Auxetic Structure with Tube0 (b)

Deformed structure at OSD.



(a)

(b)

Figure S1.29 (a) Stress Strain curve of Nylon-12 Diamond structure 0.4 mm wall thickness

(b) Deformed structure at OSD.

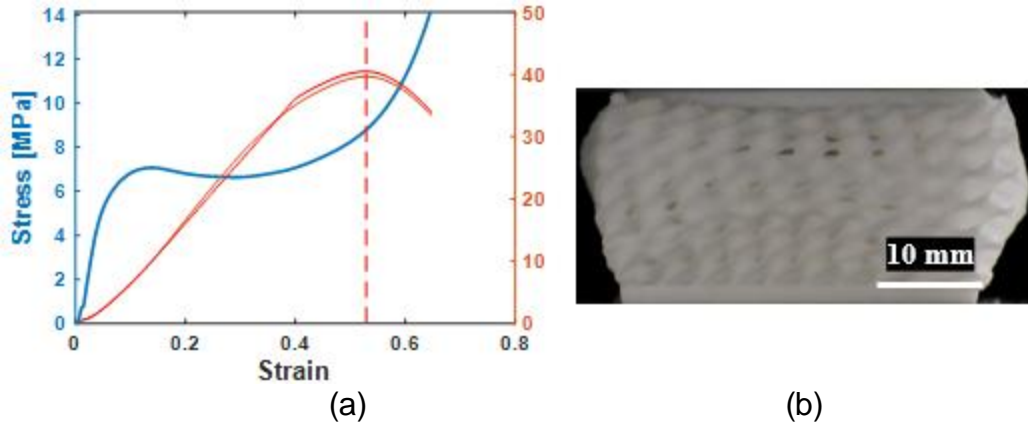


Figure S1.30 (a) Stress Strain curve of Nylon-12 Diamond structure 0.6 mm wall thickness  
 (b) Deformed structure at OSD.

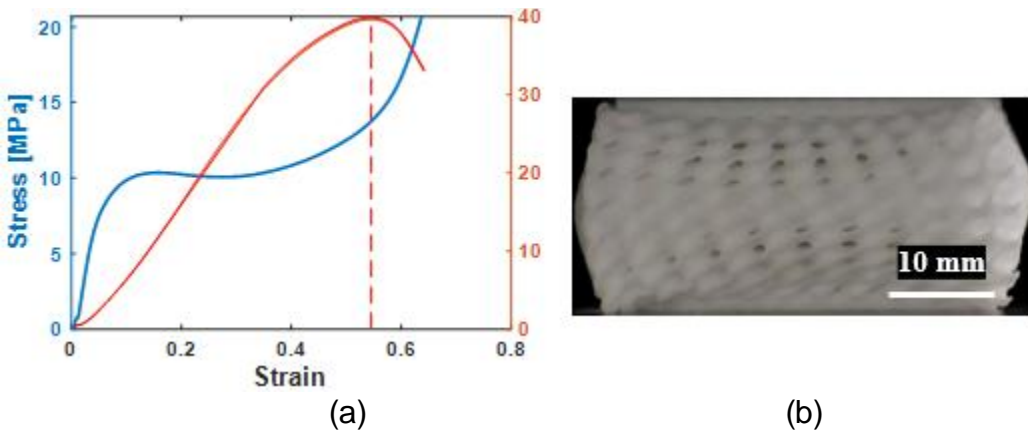


Figure S1.31 (a) Stress Strain curve of Nylon-12 Diamond structure 0.8 mm wall thickness  
 (b) Deformed structure at OSD.

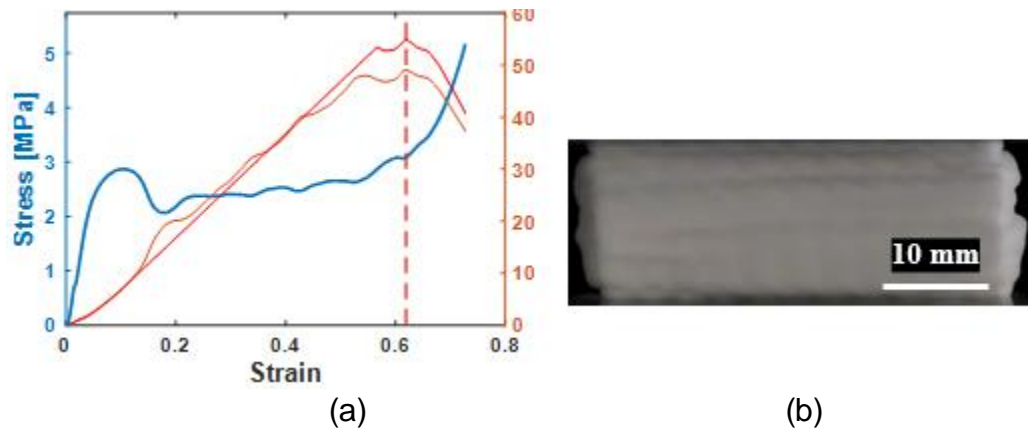




Figure S1.32 (a) Stress Strain curve of Nylon-12 Diamond with tube (b) Deformed structure at OSD.

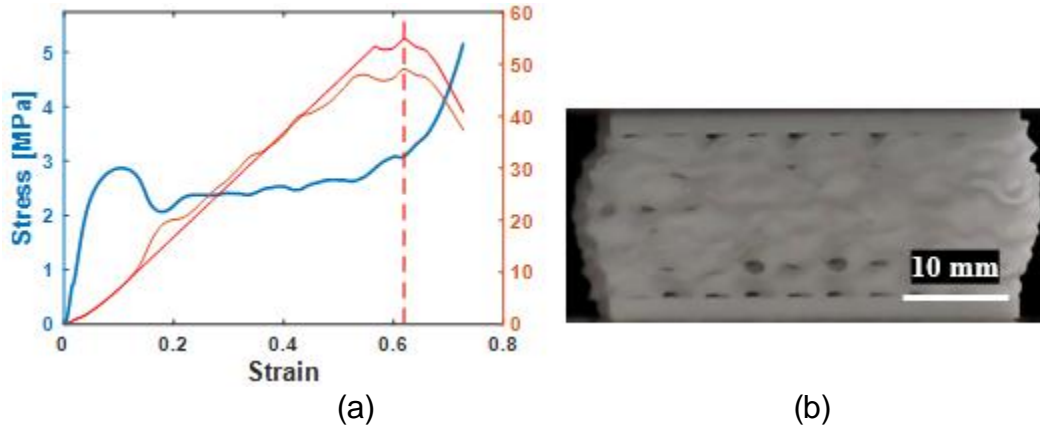


Figure S1.33 (a) Stress Strain curve of Nylon-12 Gyroid Structure 0.4 mm wall thickness (b) Deformed structure at OSD

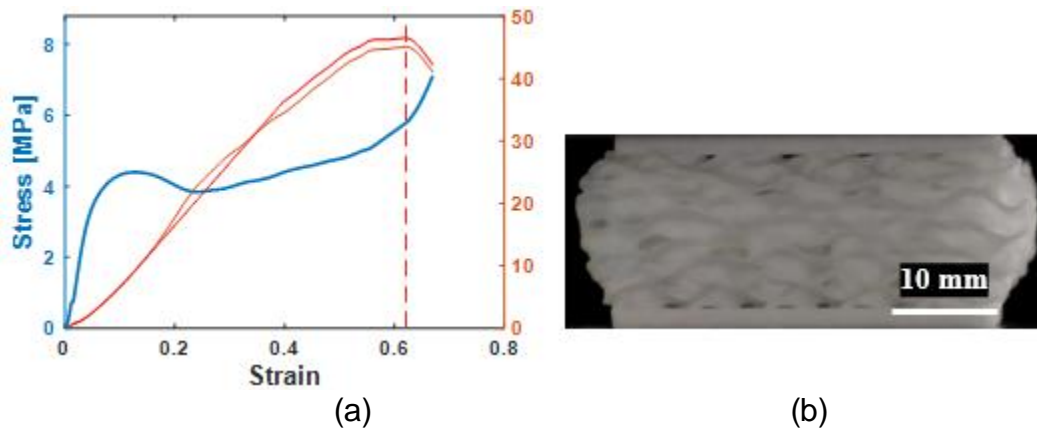


Figure S1.34 (a) Stress Strain curve of Gyroid Structure 0.6 mm wall thickness (b) Deformed structure at OSD.

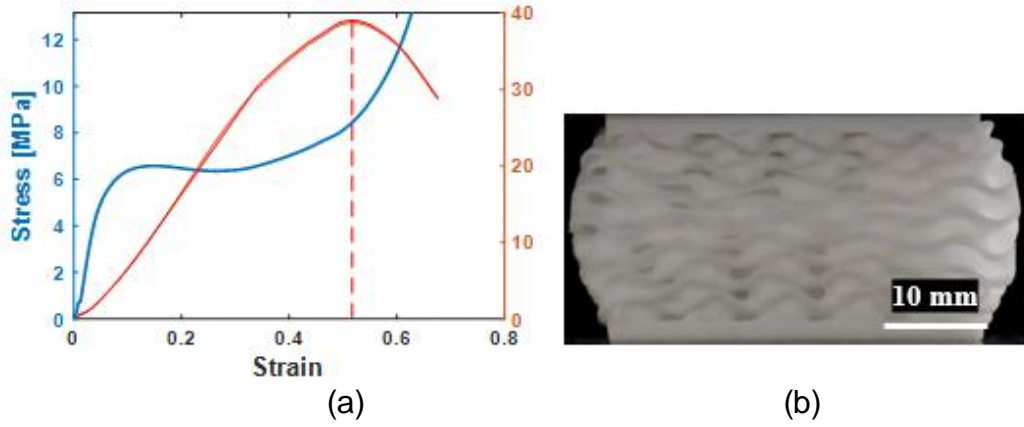


Figure S1.35 (a) Stress Strain curve of Gyroid Structure 0.8 mm wall thickness (b) Deformed structure at OSD.

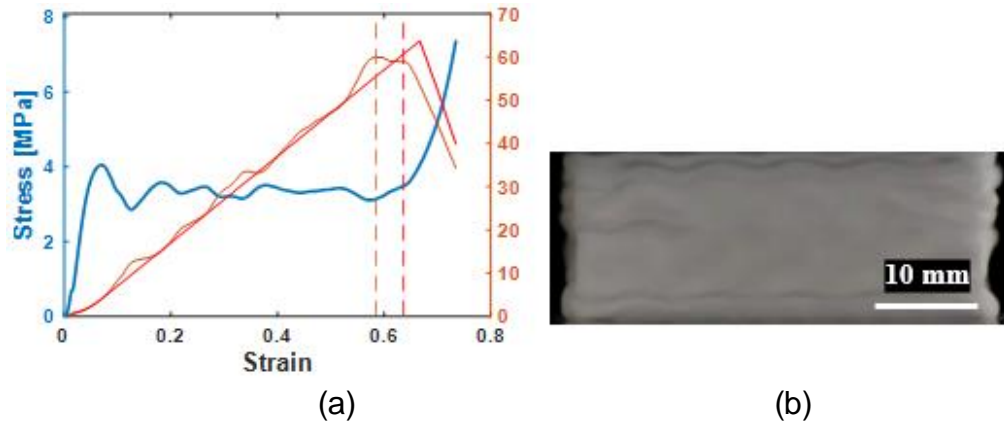


Figure S1.36 (a) Stress Strain curve of Nylon-12 Gyroid Structure with Tube (b) Deformed structure at OSD

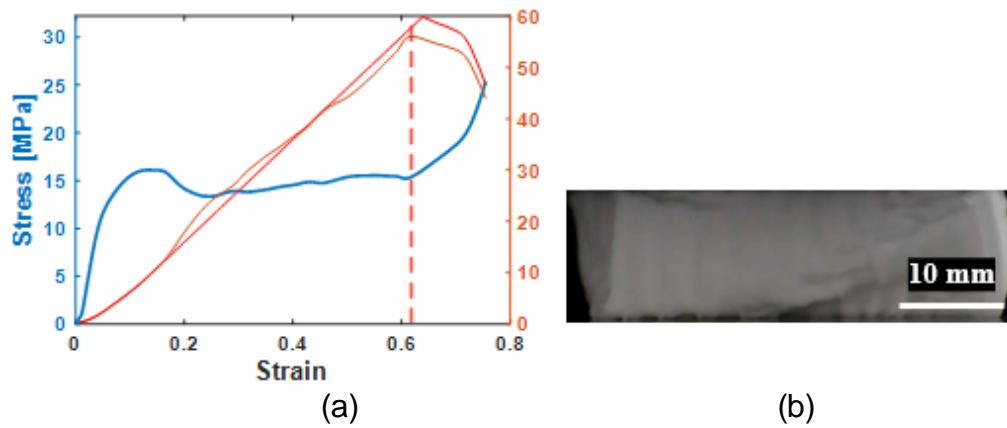




Figure S1.37 (a) Stress Strain curve of Nylon-12 Honeycomb structure 0.4 mm wall thickness (b) Deformed structure at OSD.

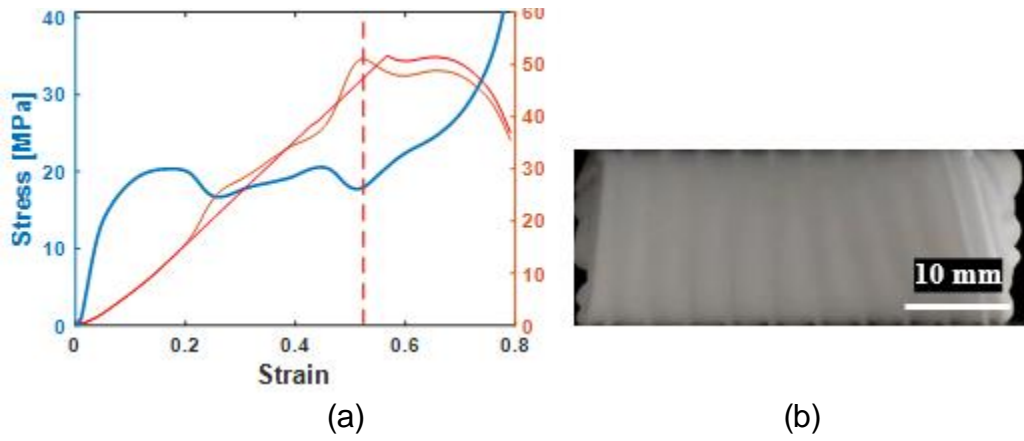


Figure S1.38 (a) Stress Strain curve of Nylon-12 Honeycomb structure 0.6 mm wall thickness (b) deformed structure at OSD

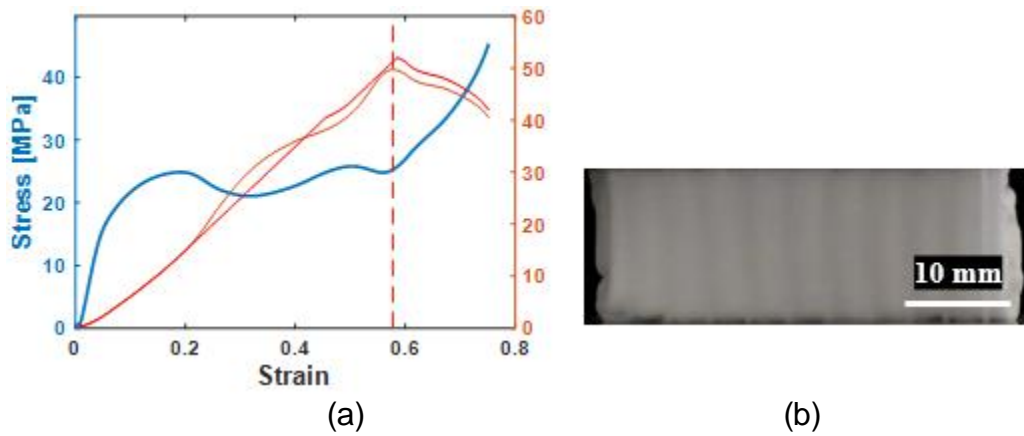
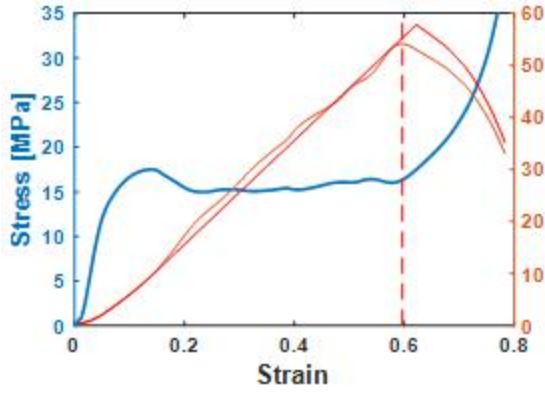


Figure S1.39 (a) Stress Strain curve of Nylon-12 Honeycomb structure 0.8 mm wall thickness (b) deformed structure at OSD.

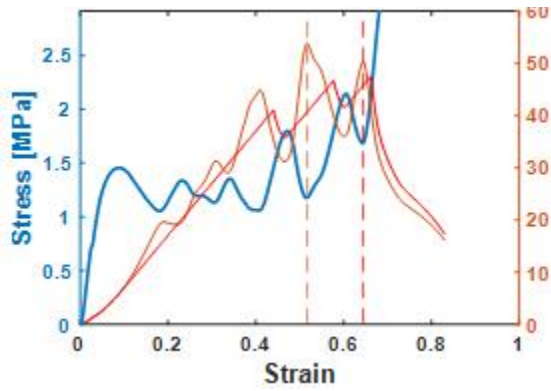


(a)



(b)

Figure S1.40 (a) Stress Strain curve of Honeycomb structure with Tube (b) deformed structure at OSD.

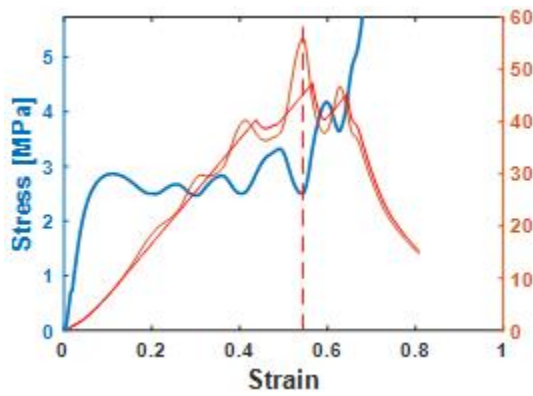


(a)



(b)

Figure S1.41 (a) Stress Strain curve of Nylon-12 Schwarz-Primitive 0.4 mm wall thickness (b) Deformed structure at OSD



(a)



(b)

Figure S1.42 (a) Stress Strain curve of Nylon-12 Schwarz-Primitive 0.6 mm wall thickness

(b) Deformed structure at OSD

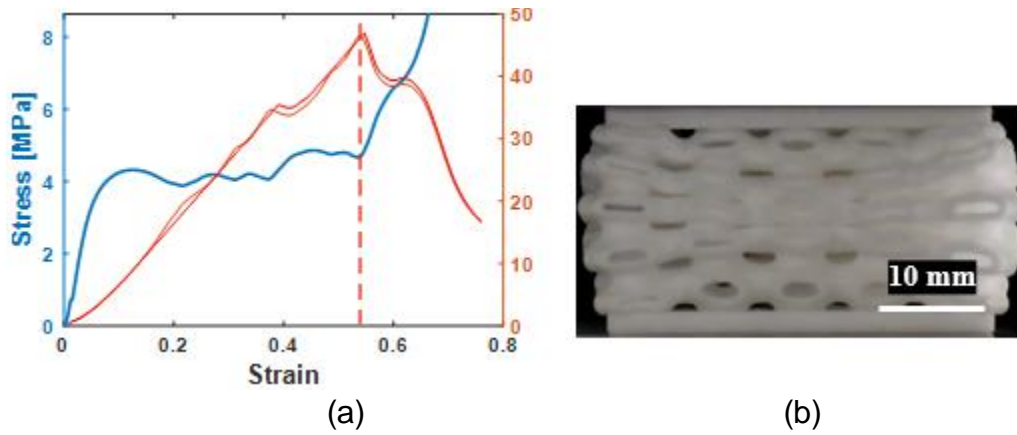


Figure S1.43 (a) Stress Strain curve of Nylon-12 Schwarz-Primitive 0.8 mm wall thickness

(b) Deformed structure at OSD.

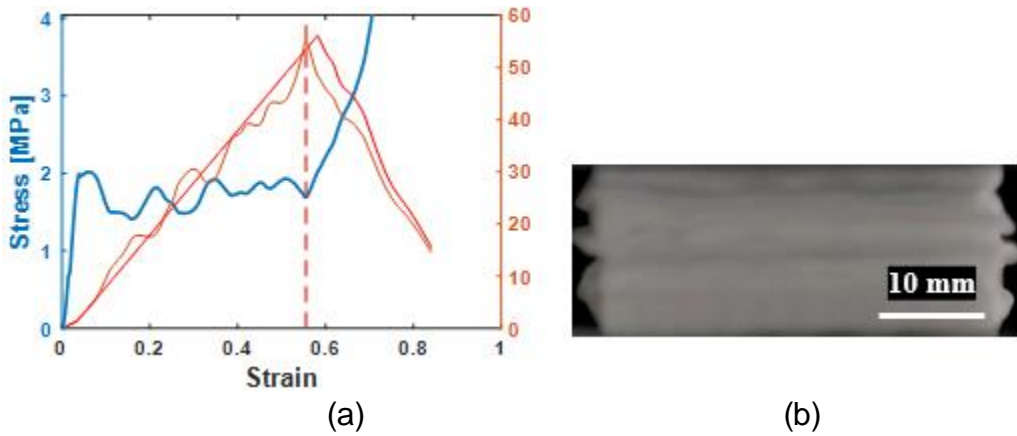


Figure S1.44 (a) Stress Strain curve of Nylon-12 Schwarz-Primitive with Tube (b)

Deformed structure at OSD

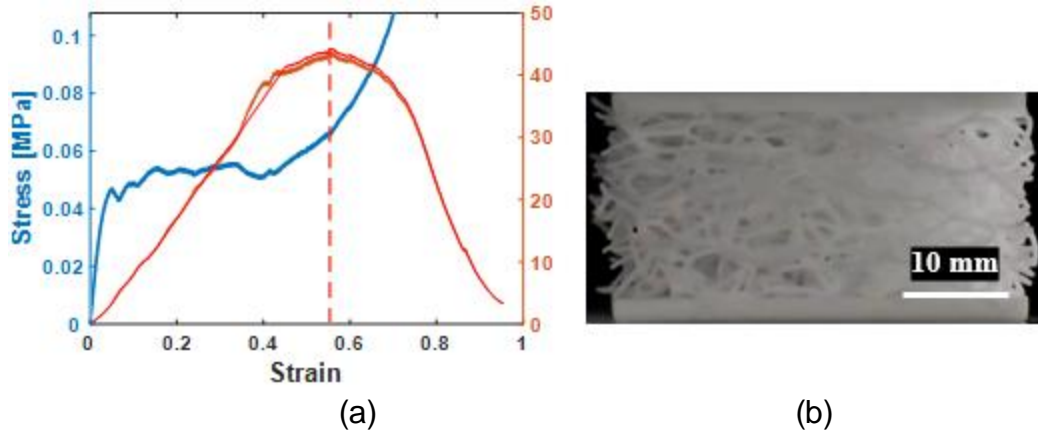


Figure S1.45 (a) Stress Strain curve of Nylon-12 Voronoi structure 0.5 mm beam diameter

(b) deformed structure at OSD

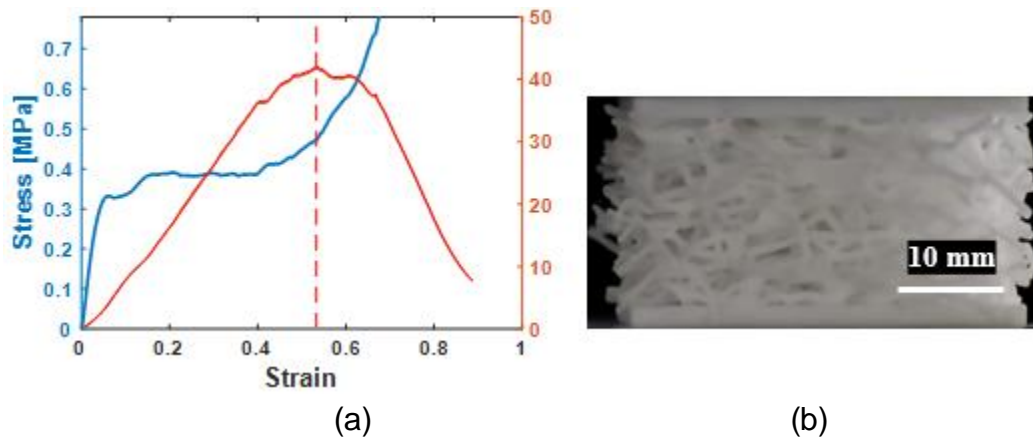


Figure S1.46 (a) Stress Strain curve of Nylon-12 Voronoi structure 0.75 mm beam diameter

(b) Deformed structure at OSD

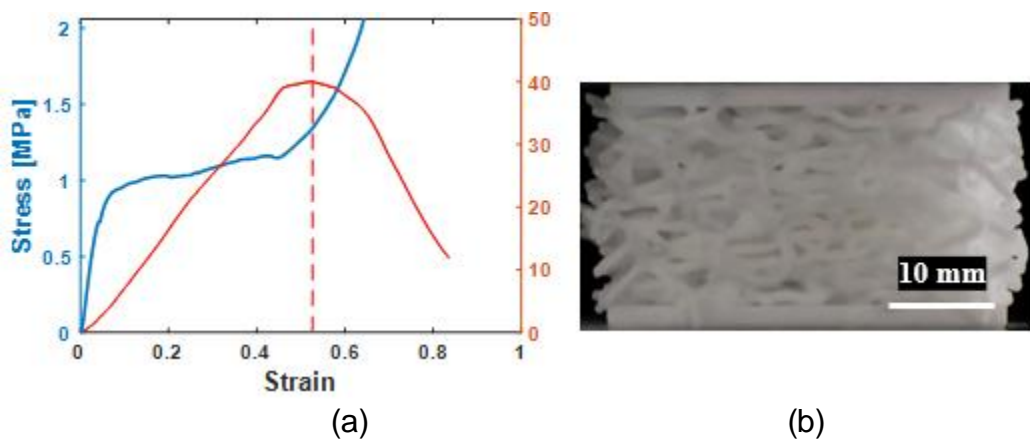


Figure S1.47 (a) Stress Strain curve of Nylon-12 Voronoi structure 1 mm beam diameter

(b) Deformed structure at OSD

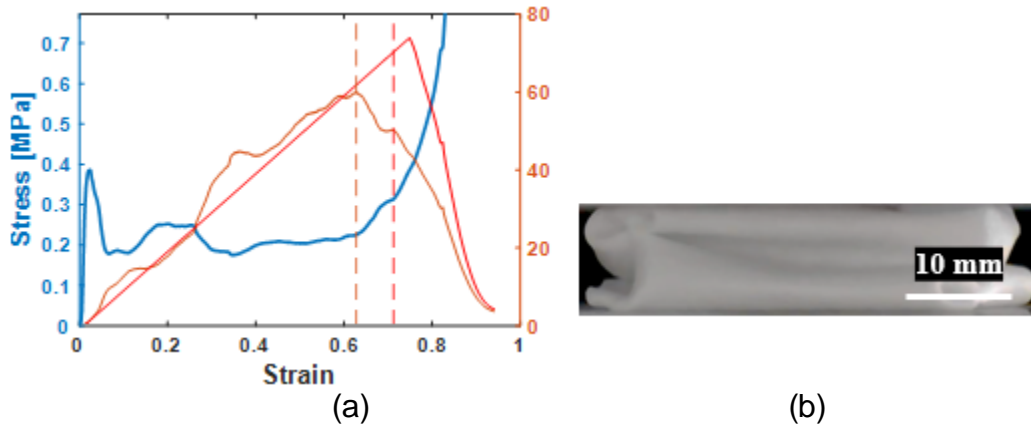


Figure S1.48 (a) Stress Strain curve of Nylon-12 Voronoi structure with Tube (b)

Deformed structure at OSD.

APPENDIX C  
ABAQUS SCRIPT

```

# This script is used to sort elements and assign thickness according
to the generated field in the geometry.

from abaqus import *
from abaqusConstants import *
import numpy as np
import regionToolset
import part
import assembly
import step
import load
import interaction
import csv

#Definitions
a = mdb.models['Full_Model_schwarz_renumbered'].rootAssembly
p = mdb.models['Full_Model_schwarz_renumbered'].parts['PART-1']
session.viewports['Viewport:
1'].partDisplay.geometryOptions.setValues(referenceRepresentation=OFF)
mdb.meshEditOptions.setValues(enableUndo=True,
maxUndoCacheElements=0.5)
instance = a.instances['PART-1-1']
allFaces = instance.faces
p = mdb.models['Full_Model_schwarz_renumbered'].parts['PART-1']
s = p.elements
l=len(s)
#currentset=p.SetFromElementLabels(name='Element_1',elementLabels=(1,2)
)
#print(currentset)
# sideElements =
s[251945:251946]+s[253793:253794]+s[414702:414703]+s[434023:434024]+s[4
34280:434281]+s[435777:435778]+s[436039:436040]
#
p.generateMeshByOffset(region=regionToolset.Region(sideElements=sideE
lements), meshType=SOLID, totalThickness=0.45, numLayers=1,
offsetDirection=BOTH)

# opening the CSV file
import csv

file = open("Element_Random_thickness_map_random_noise.csv", 'r')
ElementData = list(csv.reader(file, delimiter=","))
file.close()
sorted_elem=sorted(ElementData, key=lambda x: (float(x[1]),
float(x[0])))

# create set of different lists according to thickness values

d = {}
for value, key in sorted_elem:
    if key not in d.keys():
        d[key] = [key]
    d[key].append(value)
result = list(d.values())

```

```

# Function takes sorted list in format [t, *, *...] and returns
thickness (first value) and corresponding elements
def thickness_fn(input):
    thickness=float(input[0])
    q=[]
    q1=s[0:1]

    for i, x in enumerate(input[1:]):
        elem_no=int(float(input[i+1]))
        #print(elem_no)
        b=s[elem_no-1:elem_no]
        q1=q1+b
    #print(q1)
    return(q1[1:], thickness)

for i, x in enumerate(result):
    elem, thickness=thickness_fn(result[i])
    sideElements = elem
    print(thickness, len(elem))
    print([elem[-1]])

p.generateMeshByOffset(region=regionToolset.Region(sideElements=sideElements), meshType=SOLID, totalThickness=thickness, numLayers=2, offsetDirection=BOTH)

```



APPENDIX D

ENERGY ABSORPTION VARIABILITY GRAPHS

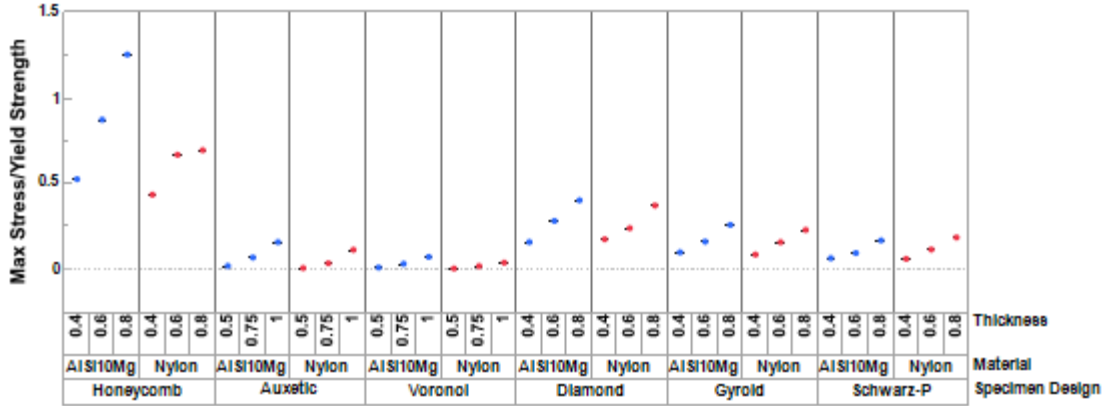


Figure S3.1 Variability chart of Maximum transmitted stress normalized by Yield strength plotted for Specimen design, material and thickness of the structure.

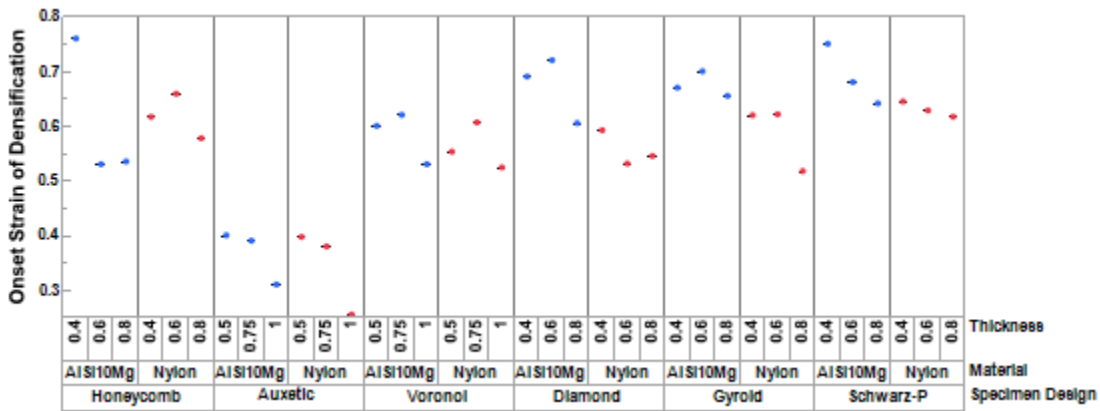


Figure S3.2 Variability chart of Maximum transmitted stress normalized by Yield strength plotted for Specimen design, material and thickness of the structure.

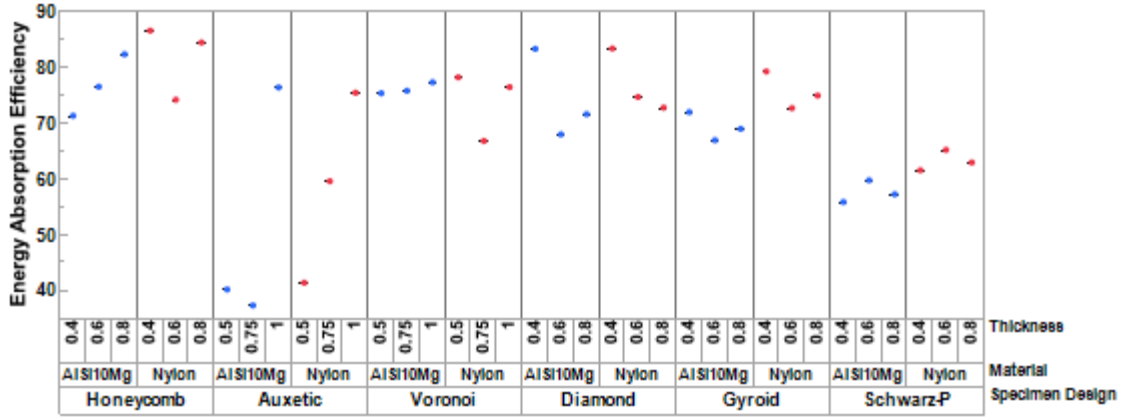


Figure S3.3 Variability chart of Maximum transmitted stress normalized by Yield strength plotted for Specimen design, material and thickness of the structure.

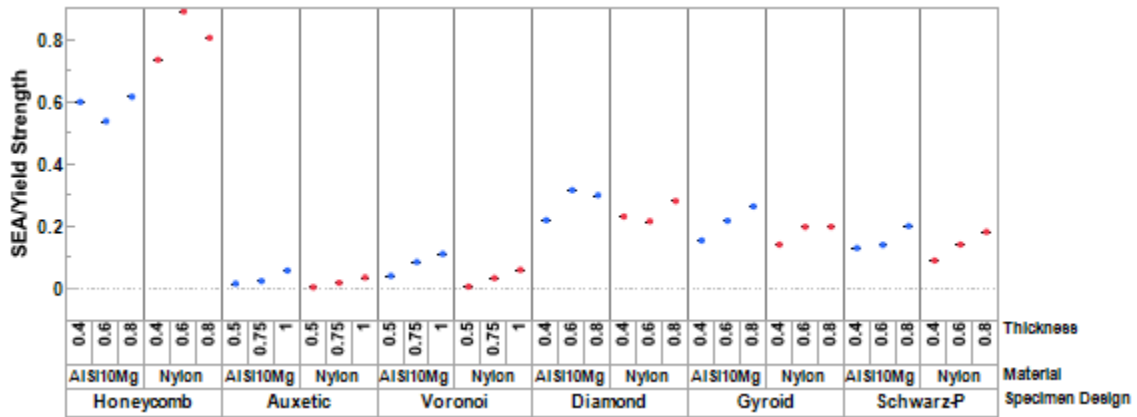


Figure S3.4 Variability chart of Maximum transmitted stress normalized by Yield strength plotted for specimen design, material and thickness of the structure

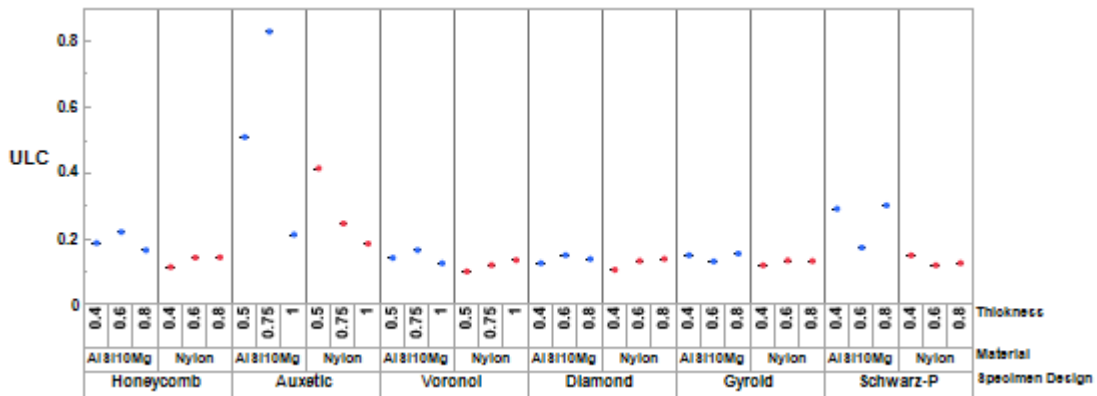


Figure S3.5 Variability chart of Maximum transmitted stress normalized by Yield strength plotted for Specimen design, material and thickness of the structure

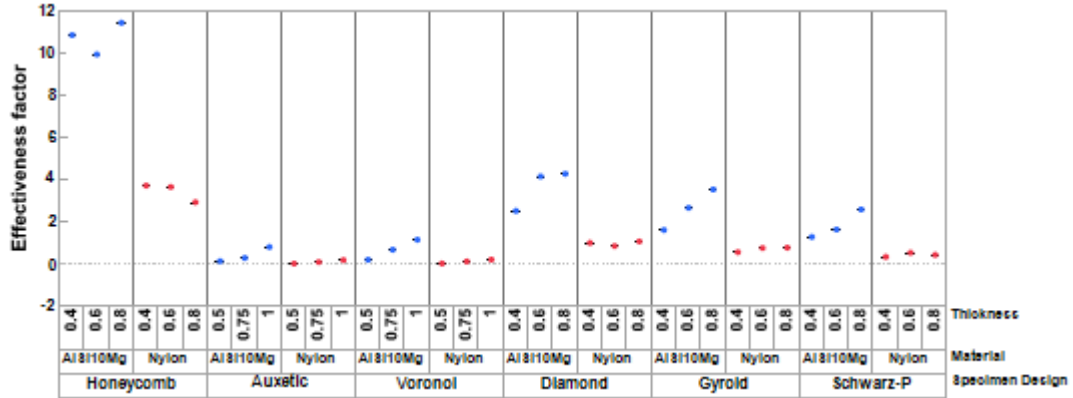


Figure S3.6 Variability chart of Maximum transmitted stress normalized by Yield strength plotted for Specimen design, material and thickness of the structure

APPENDIX E  
DECLARATION

I, declare that I have got permission from all the co-authors from the published paper 'Towards an Ideal Energy Absorber: Relating Failure Mechanisms and Energy Absorption Metrics in Additively Manufactured AlSi10Mg Cellular Structures under Quasistatic Compression' to use that work in my thesis.